3D Intelligent Antenna Design for 5G FWA Applications

Thi-Hong-Le Dam

THÈSE

Pour obtenir le grade de

DOCTEUR DE L'UNIVERSITÉ GRENOBLE ALPES

École doctorale : EEATS - Electronique, Electrotechnique, Automatique, Traitement du Signal (EEATS)
Spécialité : Optique et Radiofréquences
Unité de recherche : Institut de Microélectronique, Electromagnétisme et Photonique - Laboratoire d'hyperfréquences et de caractérisation

Conception dune antenne intelligente 3D pour les applications 5G FWA

3D Intelligent Antenna Design for 5G FWA Applications

Présentée par :

Thi-Hong-Le DAM

Direction de thèse :

Tan Phu VUONG PROFESSEUR DES UNIVERSITES, Université Grenoble Alpes	Directeur de thèse
Gregory HOUZET Maitre de Conférences, Université de Savoie Mont-Blanc	Co-encadrant de thèse
Thierry LACREVAZ Enseignant Chercheur, Université Savoie Mont Blanc	Co-encadrant de thèse

Rapporteurs :

Eric LHEURETTE
PROFESSEUR DES UNIVERSITES, UNIVERSITE DE LILLE
Laure HUITEMA
MAITRE DE CONDERENCES HDR, UNIVERSITE DE LIMOGES

Thèse soutenue publiquement le **24 février 2023**, devant le jury composé de :

Tan-Phu VUONG PROFESSEUR DES UNIVERSITES, GRENOBLE INP	Directeur de thèse
Eric LHEURETTE PROFESSEUR DES UNIVERSITES, UNIVERSITE DE LILLE	Rapporteur
Laure HUITEMA MAITRE DE CONDERENCES HDR, UNIVERSITE DE LIMOGES	Rapporteure
Ke WU PROFESSEUR, École Polytechnique de Montréal	Examinateur
Anne VILCOT PROFESSEUR DES UNIVERSITES, GRENOBLE INP	Présidente
Fabien FERRERO PROFESSEUR DES UNIVERSITES, UNIVERSITE COTE D'AZUR	Examinateur

Invités :

Gael DEPRES
DOCTEUR EN SCIENCES, Arjowiggins
Alejandro NIEMBRO-MARTIN
DOCTEUR EN SCIENCES, Schneider Electric

ACKNOWLEDGEMENT

First of all, I would like to express my deep gratitude to my supervisor and co-supervisors: PR. Tan-Phu VUONG from IMEP-LaHC, Grenoble site, Grenoble Alpes University, MCF. Grégory HOUZET and MCF. Thierry LACREVAZ from IMEP-LaHC, Chambéry site, Savoie Mont Blanc University for their guidance and support. Thank you for always being patient, guiding and helping me over the past three years.

I am also thankful to PR. Eric LHEURETTE from University of Lille I, MCF. Laure HUITEMA from University of Limoges, PR. Ke WU from Polytechnique Montréal, PR. Anne VILCOT from Grenoble Alpes University, PR. Fabien FERRERO from Côte d'Azur University and DR. Gael DEPRES from Arjowiggins for their acceptance of participation and review.

I would like to extend my sincere thanks to all members of IMEP-LaHC laboratory and RFM group. I would like to thank PR. Pascal Xavier, leader of RFM, for helping and patiently answering all my questions. I would like to give special thanks to the technician Nicolas CORRAO, who has been bothered a lot by me but is still very kind, who helped and supported me a lot with fabrications and measurements. I also give a lot of thanks to the members of the administrative secretariat, Dalhila ALOUANI, Fernanda MENDONÇA DOS REIS, Brigitte RASOLOFONIAINA, Anais DESCHAUX BEAUME, Valerie MISCIOSCIA, Gwladys ANAGNI for their support.

I would like to acknowledge MCF. Nadège REVERDY-BRUAS from Pagora, Grenoble Alpes University, PR. Damien PAULET from IUT1, Grenoble Alpes University, DR. Quoc-Bao DUONG from S.mart Grenoble Alpes, DR. Camille DELFAUT for helping to facilitate my 3D jetting print process.

I would like to acknowledge DR. Gael DEPRES and DR. Victor THENOT from Arjowiggins for their support with the printing on paper substrate.

I would like to send my thanks to my colleagues and friends, especially DR. Maxime, Jingwen, Bastien, Kim-Ngan, Hong-Son, Trọng-Thuy, Bich-Ngoc, Hong-Ngoc, Kim-Thoa, Julie, Magali for their support at work and in life.

Finally, I would like to express my deepest gratitude my family, especially my dear grandparents, my father Van-Toan, my mother Thi-Hieu, my brother Dinh-Nhu, my dear sister Nga Pham, my uncle Van-Thieu, my aunt Thi-Be, my cousins The-Tan and The-Dat for their

unconditional support. They are my biggest motivation in life, the thing that helps me to persevere no matter what happens. Words cannot express my gratitude to my family, and my companion, Dr. Edouard. Thank you for being by my side in good and bad times.

I could not have completed this thesis without the support of everyone. Thank you!

RÉSUMÉ

La 5G FWA (Fixed Wireless Access) est en cours de développement pour proposer des connexions à large bande et à haut débit. Dans cette technologie, les deux grandes familles de périphériques rencontrés sont : l'unité d'accès (Access Unit - AU) et l'équipement dans les locaux du client (Customer Premise Equipment - CPE). La 5G FWA apporte de nombreux avantages tels que le haut débit, la faible latence et la flexibilité. En France, les principales bandes utilisées pour la recherche ou le déploiement de la 5G sont les fréquences déjà précédemment utilisées pour la 2G, 3G, 4G, ainsi que la bande 3.4-3.8 GHz et la bande autour de 26 GHz. Les quatre grands opérateurs en France (Bouygues Telecom, Free Mobile, Orange et SFR) se sont inscrits pour utiliser les bandes de fréquences dans la bande 3.4-3.8 GHz en 2020 et les déployer civilement. La bande 26 GHz, bien qu'inexplorée dans les télécommunications civiles, est une bande très prometteuse pour résoudre le problème de l'explosion de la consommation de données.

Bien qu'il existe de nombreux avantages, la 5G FWA est confrontée au défi principal des pertes rencontrées à ces types de fréquences élevées. Celles-ci proviennent de diverses sources telles que les pertes durant le trajet de l'onde, la ligne de mire FWA non idéale, les pertes par pénétration de l'onde à travers les bâtiments et les pertes par interaction avec la végétation. De nombreuses études ont été menées pour mesurer, estimer et analyser ces différents facteurs de pertes. Elles ont été suivies par d'autres afin d'explorer les solutions qui minimiseraient ces pertes. En général, ces solutions d'amélioration peuvent être divisées en trois catégories : l'utilisation d'antennes à gain élevé, l'utilisation d'antennes orientables et l'amélioration des matériaux de construction. Cette thèse se concentre sur l'étude des deux premières solutions.

Les travaux de cette thèse se consacrent notamment sur les deux solutions suivantes : antennes à gain élevé et mise en forme de faisceaux. Ils sont construits sur la base d'applications pour des appareils compacts 5G tels que des appareils mobiles ou des CPE plutôt que sur des applications à large portée telles que des antennes de station. En particulier, pour les CPE, qui sont placés à l'extérieur et à proximité de bâtiments ou de bureaux afin d'assurer la communication entre l'intérieur et l'extérieur du bâtiment, il est nécessaire d'utiliser un radôme pour protéger l'antenne et ses circuits. Ainsi, dans notre solution de mise en forme de faisceaux, nous effectuons des recherches sur une application de la technologie piézoélectrique à jet 3D pour fonctionnaliser un radôme sur lequel sont imprimés des motifs permettant une sélection spatiale des ondes. La fin de la thèse présente une étude sur l'utilisation de substrats de papier

pour concevoir des composants RF (Radio Fréquences) dédiés aux applications 5G, dans une optique de développement durable et respectueux de l'environnement.

ABSTRACT

In recent years, 5G FWA (fifth generation mobile network Fixed Wireless Access) is being developed to provide broadband and high-speed connections in the context of an increasing number of devices connected wirelessly. In this technology, the two main families of peripherals encountered are: the AU (Access Unit) and the CPE (Customer Premise Equipment). 5G FWA brings many advantages such as high throughput, low latency and flexibility. In France, the main bands used for research or deployment of 5G are the frequencies already previously used for 2G, 3G, 4G, as well as the 3.4-3.8 GHz band and the band around 26 GHz. The four major operators in France (Bouygues Telecom, Free Mobile, Orange and SFR) have registered to use the frequency bands in the 3.4-3.8 GHz band in 2020 and deploy them civilly. The 26 GHz band, although unexplored in civil telecommunications, is a very promising band to solve the problem of the explosion of data consumption.

Although there are many advantages, the main challenge with 5G FWA is the losses encountered at these kinds of high frequencies. These come from a variety of sources such as wave path losses, non-ideal FWA line of sight, wave penetration losses through buildings, and vegetation interaction losses. Many studies have been conducted to measure, estimate and analyze these different loss factors, then studies related to the exploration of solutions to minimize these are developed. In general, these improvement solutions can be divided into three categories: the use of high gain antennas, the use of steerable antennas and the improvement of construction materials.

Our works in this thesis belong to the first and the second solution: high-gain antennas and beamforming technique. They are built on the basis of applications for 5G compact devices such as mobile devices or CPEs rather than wide range applications such as station antennas. Especially, with CPEs which are placed outdoors, near buildings or offices to support communication between inside and outside the building, it is necessary to use a radome to protect the circuits inside. Thus, in the beamforming solution, we do research on the application of 3D jetting piezoelectric technology to create a printed FSS (Frequency Selective Surface) radome allowing a spatial wave selection. And at the end of the thesis, we study the use of paper substrates to design some RF components in 5G applications, towards sustainable and environmentally friendly development.

CONTENTS

LIST OF TABLES

LIST OF FIGURES

LIST OF SYMBOLS AND ABBREVIATIONS

3GPP	3rd Generation Partnership Project
5G	Fifth generation
AGB	Alpha-Beta-Gamma
AI	Artificial intelligence
AFSR	Absorbent frequency selective radome
Ag NPs	Silver nanoparticles
AU	Access unit
BF	Beam forming
CDMA	Code division multiple access
CI	Close-In
CPE	Customer premises equipment
CPW	Coplanar waveguide
DSL	Digital Subscriber Line
FI	Floating Intercept
FSPL	Free-space path loss
FSS	Frequency selective surface
FWA	Fixed wireless access
GPRS	General packet radio service
IoT	Internet of things
LD	Log Distance
LoS	Line of Sight
Low-e	Low-emissivity
LTE	Long term evolution
ME	Magneto-Electric

MIMO	Multiple input multiple outpout
mMIMO	Massive multiple input multiple outpout
MMS	Multimedia messages
MTM	Metamaterial
NR	New radio
PCL	Phase compensation lens
PL	Path loss
RCA	Resonant cavity antenna
RCS	Radar cross section
PRS	Partially reflective surface
Rx	Receiver
RWG	Rectangular waveguide
SMS	Short Message Service
SUI	Stanford University Interim
Tx	Transmitter
TE	Transverse electric
TEM	Transverse electromagnetic
VSWR	Voltage standing wave ratio
ZIM	Zero-index metamaterial

Chapter 1. Fixed Wireless Access and 5G technology – State of the art

The chapter presents an overview of the development of 5G fixed wireless access worldwide and its challenges are also discussed. Next, the problem we choose to contribute to and the structure of the thesis will be introduced.

1.1. 5G Fixed Wireless Access Introduction

1.1.1. 5G Introduction

What is 5G?

5G is the 5th generation mobile network. 5G is being developed to expand wireless broadband services beyond mobile internet to Internet of Things (IoT) and critical communications segments. This is a new global wireless standard after earlier generations of mobile network:

- First generation (1G): In the 1980s, 1G delivered analog voice services

Originally launched in 1979 in Tokyo, until 1984, the first generation of the wireless standard was developed in Japan by the Nippon Telegraph and Telephone. In 1983, the United States launched its first 1G network using the Motorola DynaTAC mobile phone, followed by other countries like Canada and United Kingdom several years later.

- Second generation (2G): In the early 1990s, 2G introduced digital cellular voice services (e.g. Code Division Multiple Access - CDMA) and basic data services (SMS, GPRS).

2G was launched commercially on the Global System for Mobile Communications (GSM) standard in Finland in 1991. It presented data services for mobile, including SMS text messages and digitally encrypted conversations for the very first time. The second generation provided a higher quality of digital voice calls with a significant reduction in static noise and background crackling. This generation created a huge cultural shift by creating a whole new way for people to communicate through text messages, picture messages, and multimedia messages (MMS).

- Third generation (3G): In the early 2000s, 3G brought a better mobile internet experience (e.g. CDMA2000)

3G was first appeared in Japan, in October 2001. Like 2G did to 1G, 3G delivered a higher level of connection than its predecessor - 2G. 3G users were able to watch mobile television, use location-based services, participate in video conferencing and watch videos on demand.

- Fourth generation (4G): In the 2010s, 4G networks brought all-IP services (voice and data), a fast broadband internet experience, with unified networks architectures and protocols

4G was first presented in the United Kingdom in 2012, and EE (a British national mobile network operator and internet service provider) deployed its 4G services to 11 major cities. This standard offers gaming services, fast mobile web access, high-quality video conferencing, high-definition videos and TV support.

5G is built with the expectation of creating a generation faster than 4G and having the potential to enable big data industries like IoT and smart cities. Some important milestones in the development of 5G are presented in Figure 1-1.

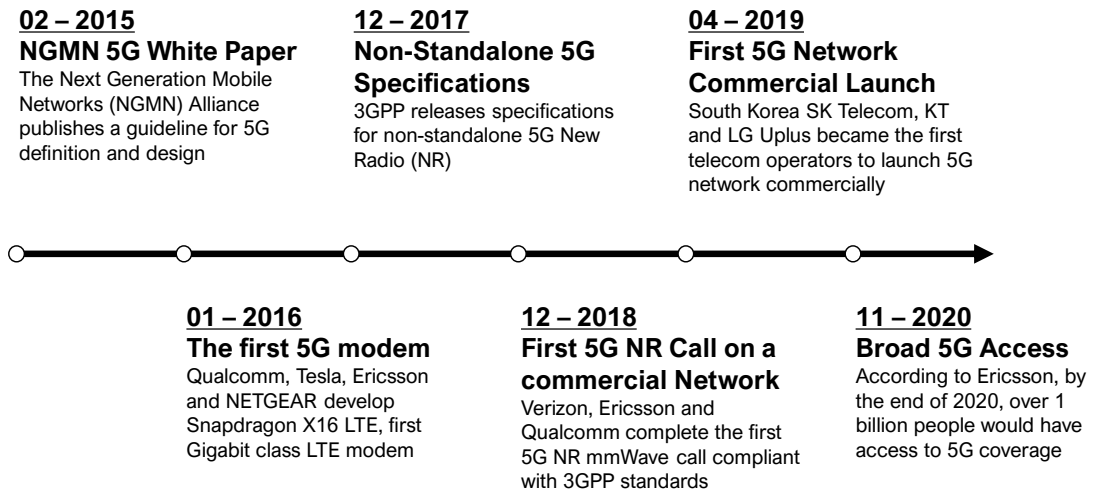

(Source : https://www.startus-insights.com)

Figure 1-1. Some important milestones in 5G development

5G is developed in a wide variety of frequency bands. Main 5G bands are summarized in Figure 1-2. Each carrier frequency band has different advantages in the development of 5G. For example, low-band spectrum offers blanket coverage, 5G mid-band spectrum provides coverage and capacity and 5G high-band spectrum delivers super-fast speeds over short distances. The 5G mobile wireless standard has been allocated different frequency bands in different countries and regions. The frequency bands under development and planned for some European countries are presented in Table 1.

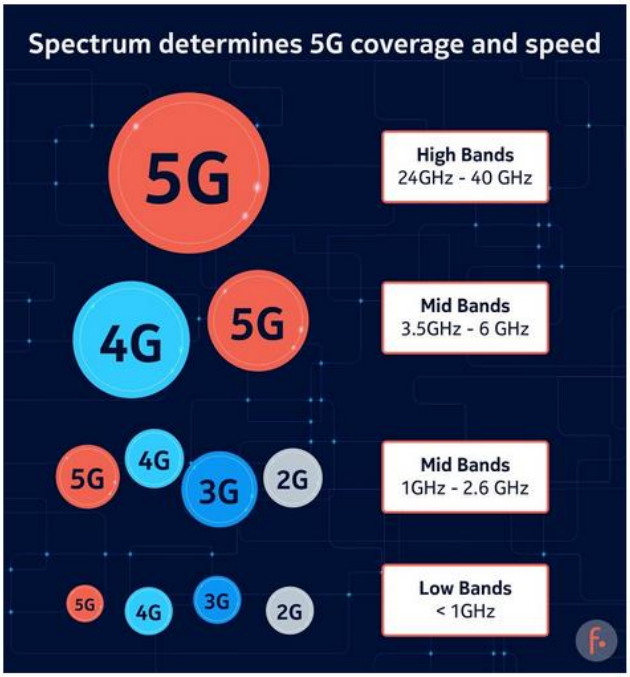

(Source : https://www.nokia.com)

Figure 1-2. 5G frequency bands

Table 1. 5G spectrum allocation in some European countries

Country	Frequency Band	Frequency
Finland, Ireland	n78	3.4-3.8 GHz
	n258	25.1-27.5 GHz
France	n78	3.4-3.8 GHz
	n257	26.5-27.5 GHz
Germany	n1	1920-1980 MHz (Uplink) 2110-2170 MHz (Downlink)
	n78	3.41-3.8 GHz
	n258	25.1-27.5 GHz
Italy	n78	3.6-3.8 GHz
	n258	26.5-27.5 GHz
	-	700 MHz
United Kingdom	n78	3.4-3.8 GHz
	n258	24.25-27.5 GHz

(Source : https://www.everythingrf.com/community/5g-frequency-bands-in-europe)

The frequency bands used for 5G in France include:

- The 3.4 - 3.8 GHz band, this is the band that has been allocated exclusively for 5G, after a long allocation and auction process.
- The frequencies of 2G, 3G, 4G (700 MHz, 800 MHz, 900 MHz, 1.8 GHz, 2.1 GHz, 2.6 GHz), which operators can switch to 5G.
- The 26 GHz band, this is the band that will allow 5G to express its full potential. It will be allocated to 5G in the coming years, no sooner than 2022 or 2023.

Most network operators in France have chosen to use the frequencies in the 3.4 - 3.8 GHz band that they purchased in the fall of 2020 as a priority for 5G. Of the 400 MHz of this entire band, 310 MHz was assigned exclusively to 5G. This should still be sufficient for operators to offer their subscribers good quality 5G services. The 26 GHz band, although unexplored in civil telecommunications, is a very potential band to address the explosion in data consumption. It not only allows a very wide spectrum, but also speeds comparable to those of optical fibers. But very high frequencies have limits as well. First, they have a low building penetration capability. They then have a limited range, around 150 meters in urban areas, which will require the deployment of a large number of antennas. The 26 GHz band will be allocated to 5G in the coming years, but for now, it's simply a test subject. In France, the call for applications for the spectrum assignments in the 3.4 - 3.8 GHz band was launched in December 2019. During this process of allocating 5G frequencies, the State, via Arcep, the telecoms regulator, granted operators a frequency spectrum of 310 MHz (3490 – 3800 MHz). It was attributed to the four major network operators Bouygues Telecom, Free Mobile, Orange and SFR with the distributions as indicated in Figure 1-3.

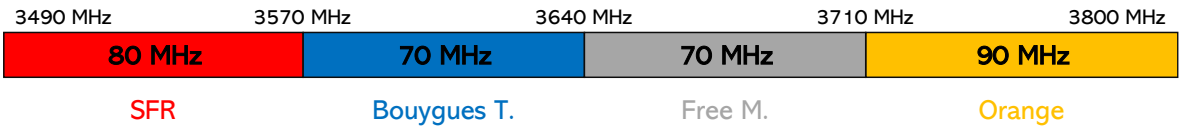

(Source : https://www.arcep.fr)

Figure 1-3. 5G frequency distribution for four major network operators in France

Advantages and disadvantages of 5G?

5G wireless technology aims to deliver higher multi-Gbps peak data speeds, ultra-low latency, more reliability, massive network capacity, increased availability, and a more uniform user

experience for more users. Enhanced performance and efficiency empower new user experiences and connect new industries. 5G is expected to achieve some objectives:

- High speed in transmissions: 5G speed in transmissions is expected to approach 15 or 20 Gbps. 5G has a higher speed than 4G and 4G LTE (Long Term Evolution). It allows users to download movies, videos, and music in seconds rather than minutes. This allows users to save a lot of data transmission time, thereby improving quality and efficiency of work.

- Low latency: Latency can be defined as the time that elapses since a user order is given on the device until the action happens. 5G is developed to have low latency, compared to 4G, to support new applications such as artificial intelligence (AI), the Internet of things (IoT), and virtual reality efficiently. High latency can have serious consequences in certain applications, such as autonomous car, so the ability to provide low latency will help develop and increase the reliability of these applications.

- Higher capacity: 5G can provide a capacity up to 100 times more than 4G capacity thanks to its broadband property. With 5G, the number of devices that can be connected to the network increases greatly and can reach millions of terminals per square kilometer.

Apart from the strengths that 5G brings, there are still some weaknesses and difficulties in the development of 5G:

- Limited broadcast distance: 5G operates at high frequencies, the loss in the air becomes significant, so 5G will not travel as far as 4G. In addition, other obstacles such as buildings, trees or walls may block the frequency of the 5G network, which will lead to various problems. Weather effects like rain can also cause problems to 5G coverage.

- Insufficient infrastructure: Old 4G infrastructure may not be re-used for 5G, so a whole ambitious investment is needed to build infrastructure for 5G to increase bandwidth and expand coverage, and this is quite expensive. This situation can cause delays in 5G network deployment.

- Security risk: 5G network is newly developed and may have cryptographic security deficiencies. In addition, more bandwidths can impede security monitoring.

Development of 5G?

Because 5G networks are cellular, network coverage may be used as an aspect to examine or evaluate the strength of the 5G network. The global 5G new radio (5G NR – a set of standards that replace the 4G LTE standard) deployments map in 2020 is presented in Figure 1-4. It can

be seen that in 2020, commercial 5G NR was widely covered worldwide. Most European, East Asian countries and major countries such as the United States, Canada, Australia had deployed commercial 5G with the rest of the world picking up the pace in deployments. At the same time, other countries such as Russia and Madagascar also implemented pre-commercial 5G networks.

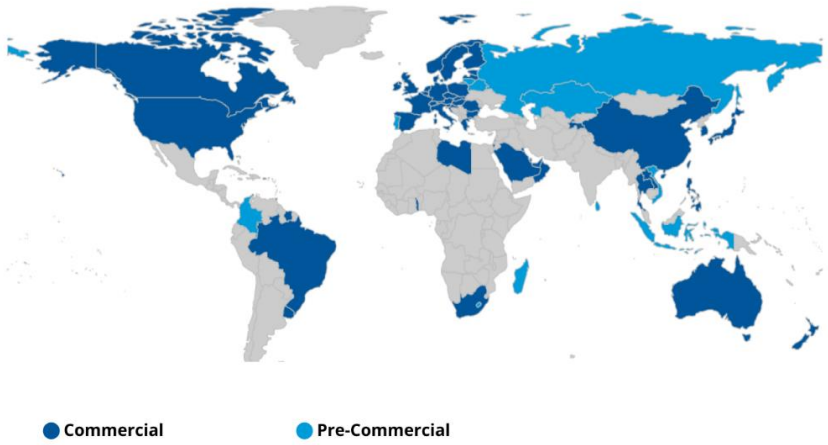

(Source : https://www.startus-insights.com)

Figure 1-4. Global 5G New Radio deployments map in 2020

According to Ericsson's survey report, in the second quarter of 2022, 5G reached 690 million subscriptions globally (a 5G subscription is counted as such when associated with a device that supports NR, as specified in 3GPP (3rd Generation Partnership Project - a coalition of telecommunications organizations that create technical standards for wireless technology) Release 15 and is connected to a 5G-enabled network). In the second quarter of 2022, the total number of mobile subscriptions was around 8.3 billion, with a net increase of 52 million subscriptions over the quarter. Figure 1-5 presents the mobile subscriptions by technology for recent years as well as projections for the coming years. A strong growth of 5G subscription is observed. By the end of 2027, 5G subscriptions are predicted to reach 4.4 billion globally, representing 48% of total mobile subscriptions. The 5G subscription uptake is faster than that of 4G as can be seen in Figure 1-6, reaching 1 billion subscriptions two years earlier than 4G. 5G is predicted to become the dominant mobile access technology by subscriptions in 2027.

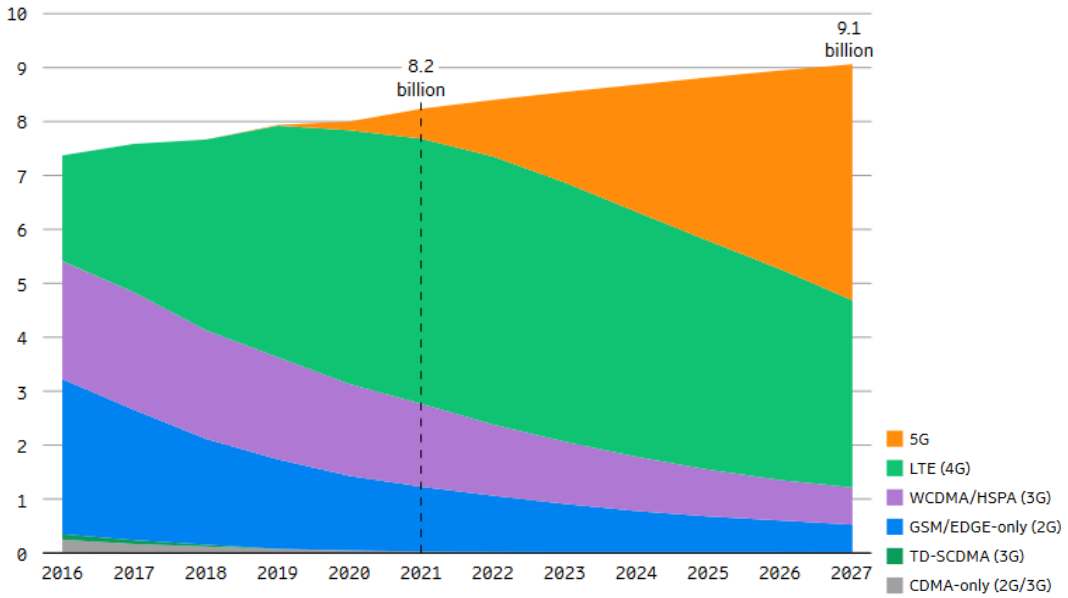

Figure 1-5. Mobile subscription by technology (billion) [1]

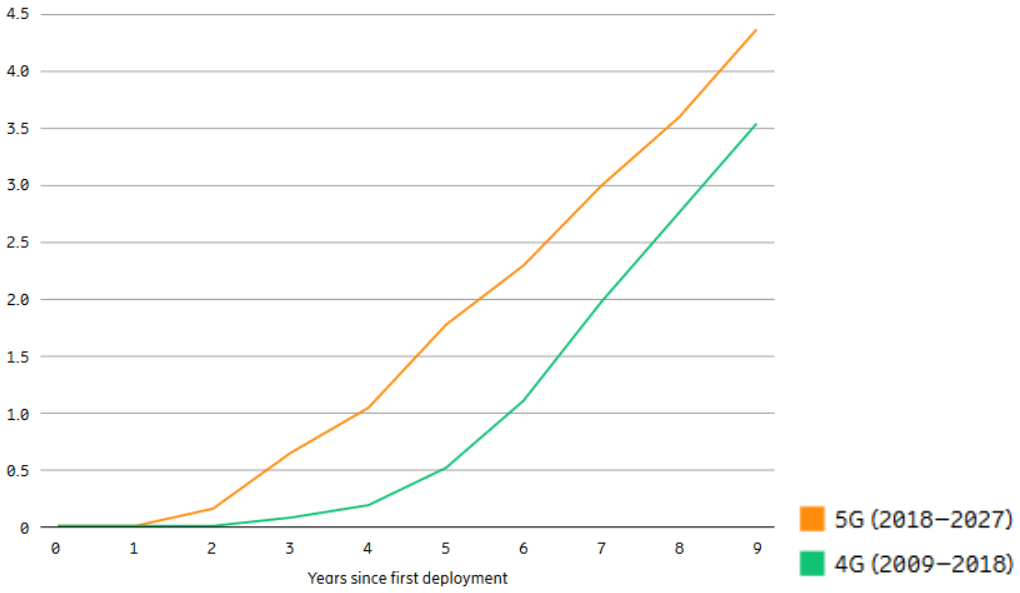

Figure 1-6. Comparison of 5G and 4G subscription uptake in the first years of deployment (billion) [1]

1.1.2. 5G Fixed Wireless Access (FWA)

What is FWA and advantages of FWA?

Fixed Wireless Access (FWA), in general, can be definied as a connection that provides primary broadband access through mobile network and enabled customer premises equipment (CPE).

FWA is a way to provide wireless connectivity through radio connection between fixed points. It does not include portable battery-based Wi-Fi routers or dongles. FWA provides wireless internet access to homes or businesses without fiber or cables at last mile connectivity as summarized in Figure 1-7.

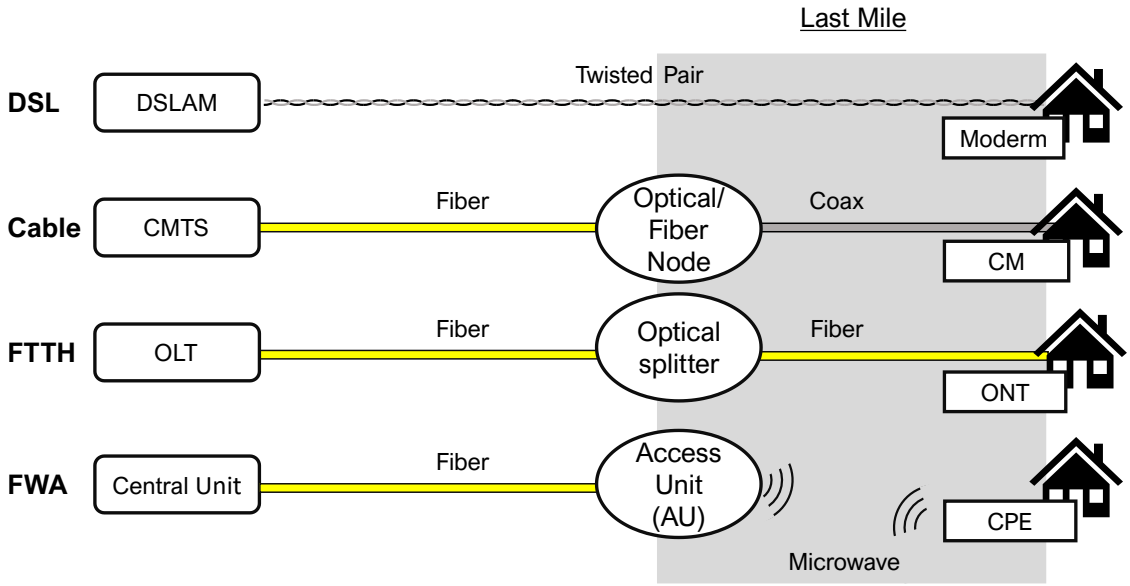

Figure 1-7. FWA compared to wireline technologies [2]

Compared to traditional fiber usage, FWA has the following advantages:

- Faster deployment: The deployment speed of an FWA network for outdoor connectivity is significantly higher than a comparable wired technology deployment. With wired technologies, the time required to bury or lay cables at each network endpoint is considerable, which may increase when it is required to cross a road or other assets not owned by the deployment organization.

- Lower cost: The typical cost of FWA deployment is about a decade cheaper than a wired network, especially in the case of outdoor area. This is due to the cost of cable installation in the street, needing big amout of public works, but also administrative procedures, and safety training and equipment for workers when laying the cable, in addition to maintenance costs once the installation is done.

- More flexible: FWA is more flexible as it can be deployed in different geographies. With FWA, the network operator can provide high speed broadband network to suburban and rural areas with a lower cost than fiber lines. FWA also has the flexibility to modify frequency bands and applications, and is more flexible with uncertain subscriptions.

Development of 5G FWA?

4G FWA has been researched and developed, however, this technology is considered inefficient, costly to deploy, and cannot provide the speed needed to compete with wired broadband connections. These things have changed with the introduction of 5G technology. Using standardized 3GPP architectures and common mobile components, 5G FWA can provide ultra-high-speed broadband services to subscribers such as residential subscribers or business customers. Not only that, 5G FWA can also provide services that can compete with DSL, cable or optical fiber thanks to the New Radio feature. Therefore, suburban and rural subcribers can also access and use high-speed connections easily.

As a result of its benefits, 5G FWA is becoming increasingly popular and widely deployed. According to a study of retail packages offered by service providers worldwide in Ericsson's report in June 2022 [1], in the first half of 2022, the number of 5G FWA service providers worldwide increased by about 30%, from 57 to 75 service providers. The development estimate of the 5G FWA based on the Ericsson study, presented in Figure 1-8, also shows that 5G FWA will continue to outperform. It is expected to reach approximately 110 million connections by 2027, which is almost half of the total number of FWA connections.

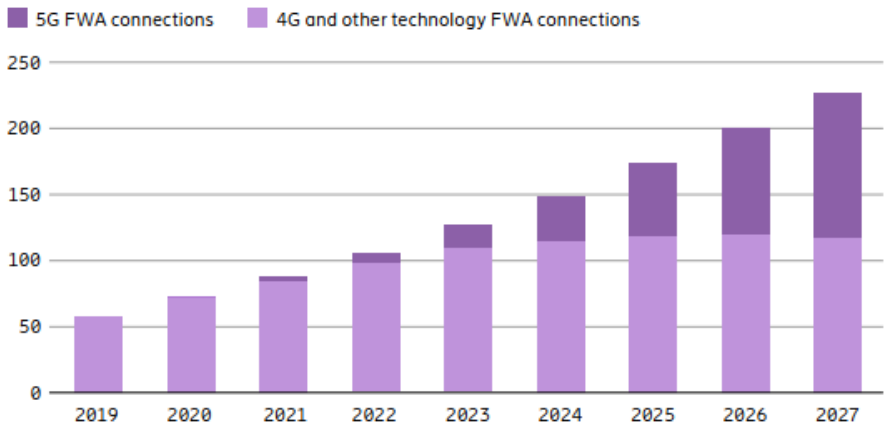

Figure 1-8. Forecast of FWA connections (millions) [1]

1.1.3. Challenges in 5G FWA

While receiving a lot of attention and expected to thrive, 5G FWA also faces many challenges. The principal challenges may be mentioned as follows:

- High loss: In addition to distance issues, 5G FWA in mmWave band faces propagation problems. Radio transmission in the mmWave bands is inherently lossy. It is sensitive to the

environment and can be easily disturbed with obstacles such as buildings or plants. This reduces the coverage of 5G FWA. Losses can be divided into the following four categories [3]:

- High path loss: The path loss defines how the strength of the received signal decreases with an increase in the distance between sending and receiving nodes [3]. In addition, it is strongly affected by the property of the environment in which the network is deployed [4]–[6]. Because the free-space path loss is inversely proportional to the square of the wavelength [7], the loss at such high frequencies in 5G FWA becomes more significant and more impactful than the loss at lower frequencies.
- Non-ideal FWA Line of Sight (LoS): LoS in general can be understood as a direct view to another object from a point of origin. In radio communication, if other techniques (such as reflection systems) are not used, signals operate in LoS. As well, FWA requires LoS between base station and end-user devices. However, when implementing FWA in practice, it is difficult to have an ideal LoS due to the influence of obstacles and terrain. These obstructions may prevent the installation of 5G FWA in some areas.
- Penetration loss through buildings: Numerous studies and measurements show that penetration loss becomes a concern in FWA applications that supply buildings [8]–[13]. The loss increases rapidly with frequency when passing through some special materials such as concrete or double-glazed sound or thermal insulation, which is usually made of low-emissivity (low-e) glass.
- Penetration loss by plants: The presence of plants in the signal path in an FWA network has been observed to have an effect on signal transmission. Parts of trees such as leaf branches, twigs and trunks which are randomly distributed in propagation environments can cause scattering, attenuation, absorption, and diffraction of radiated waves [7]. These factors can cause difficulties for wireless communication systems, and it becomes more evident during the deployment of 5G FWA in rural or suburban areas where there are dense vegetation systems.

- Expensive customer premises equipment (CPE): One of the promised benefits of FWA is that it allows customers to install the system quickly and easily themselves at home without requiring a special technician. By purchasing a CPE and installing it according to the supplied user manual, the FWA system will be configured. It also shows that the purchase of a CPE is a necessity to receive the 5G signal from the access unit (AU) and provide ethernet connectivity to the local access network (LAN). For 4G FWA, a CPE typically costs less than 300 euros.

Meanwhile, with 5G FWA, cheapest CPEs generally cost between 500 - 1000 euros. This is a high cost for many customers and could prevent customers from accessing the 5G FWA.

1.2. Review of Related Works on 5G Fixed Wireless Access

As presented, 5G FWA has a great potential, promising to bring many benefits to users. However, 5G FWA also faces many challenges as mentioned in the previous sections. To clarify these challenges and find solutions to improve and solve problems, a lot of research on 5G FWA has been carried out. This section will focus on presenting an overview of some of these studies to provide an overview of the evolution of 5G FWA research, proposed solutions to 5G FWA problems and solution development directions.

As mentioned, the two major challenges facing 5G FWA are high losses and high-cost CPE issues. In which, the second issue largely depends on manufacturers and suppliers. Therefore, this section will focus more on research related to the high losses issue. Although divided into four types of losses, it can also be said that non-ideal LoS, penetration loss through buildings and vegetations are three of the factors that increase the high path loss. Therefore, the term path loss will also be used to represent all four losses listed in the previous section.

Path loss (PL) measurement and prediction model

Path loss (PL) is an important loss in wireless communication, especially at high frequencies. Path loss refers to the attenuation that a propagating electromagnetic wave encounters along its path between the transmitter (Tx) and the receiver (Rx). To efficiently deploy the 5G FWA system in a certain area, it is very important to estimate how much path loss may be encountered in order to find solutions and decide whether to deploy 5G FWA in this area. In order to estimate this loss, path loss models were used. Path loss models describe the signal attenuation between a transmit and a receive antenna as a function of the propagation distance and other parameters. The free-space path loss can be calculated by formula (1.1).

$$FSPL = 20\log\left(\frac{4\pi d}{\lambda}\right) \quad (1.1)$$

Where:

- $FSPL$: Free-space path loss (dB)
- d: distance between the antennas (m)
- λ: signal wavelength (m)

However, when deployed in practice, there are many more factors affecting PL such as reflection, diffraction, absorption, dispersion, atmospheric particles, and the PL model becomes much more complicated than (1). The FWA deployment in different areas such as urban areas, rural areas, plains, forests, or mountains will give different path loss. Therefore, there are many PL models that have been studied and proposed to respond to these different specific environmental conditions. Some famous basic models can be mentioned as Okumura, Hata, LHata, COST 231 Extended Hata, Hata – Okumura Extended, Walfisch-Ikegami, Stanford University Interim (SUI), Ericson Model, Third Generation Partnership Project (3GPP)/ITU-R, Alpha-Beta-Gamma (AGB), Close-In (CI), Floating Intercept (FI), 2-ray, Winner II, Log Distance (LD). For each different situation and condition, there are different suitable models. One model may be suitable under these conditions but may also yield very misleading for other results. Therefore, it is necessary to rely on specific characteristics when implementing FWA to select appropriate models to estimating PL. However, many studies also show that, CI and FI are two of the models that give the most reasonable estimation results in many cases, in rural or urban areas. Many PL measurements have been implemented under different conditions to compare and evaluate the accuracy and efficiency of PL models [14]–[18]. In [19], the PL measurement in rural areas in Greece, at 3.7 GHz, for LoS conditions between Tx and Rx, was developed. In total, 1200 outdoor LoS link were measured in a commercial FWA network. The path losses in measurement and in predictions by some PL model in this work are presented in Figure 1-9(a). It can be seen that, in this particular case, CI and FI presented a better prediction than Winner II, 3GPP/ITU-R and Extended Hata. Another example of path loss measurement in urban conditions at 39 GHz was been taken and presented in [18]. Measured path loss and estimated path loss calculated by some models (FSPL, AB and CI) are compared and evaluated, via path gain, and are presented in Figure 1-9(b). It can be seen that, in these urban conditions, CI gives the closest results to the measurement.

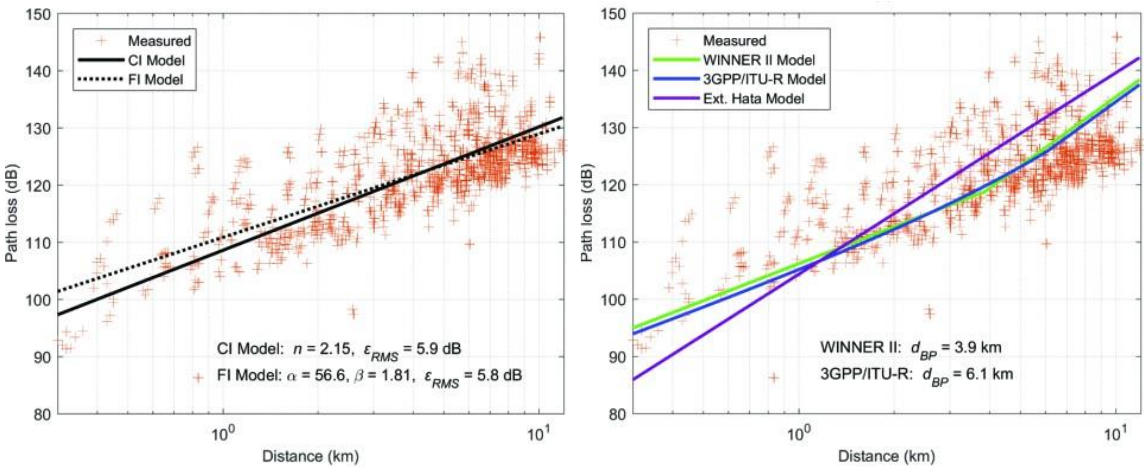

(a)

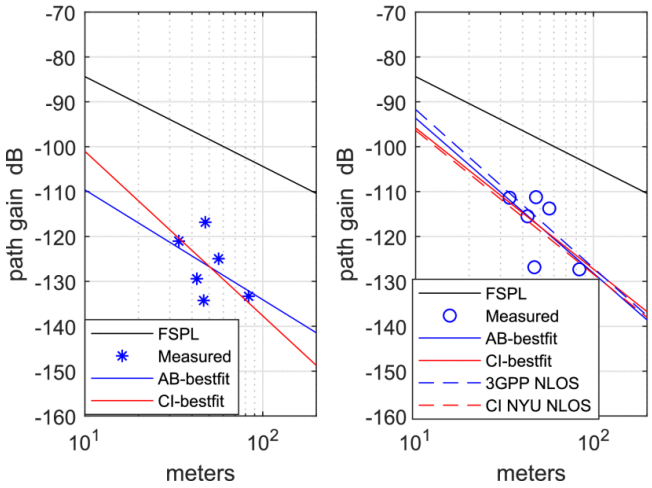

(b)

Figure 1-9. (a) Rural path loss measurement in [19] (b) Urban microcell 39 GHz measurement in [18]

Because the prediction of path loss greatly affects the decision, planning and deployment of the 5G FWA system, the accuracy of PL models is of great concern. In addition to the basic PL models mentioned, there are currently a number of studies that have been carried out with the aim of improving or creating new enhanced prediction models with higher accuracy in some specific cases [5], [16], [20], [21]. In [20] and [21], dual-slope CI model was used to achieve a more accurate path loss prediction than the standard CI path loss model. A probabilistic path loss model based on LoS and non-LoS omnidirectional propagation path loss data presented in [5] provides a fairly stable and accurate PL estimation. However, these methods increase the complexity of the PL model. Thus, some research has been done to make the PL model more accurate without complicating it, for instance in [16]. In [16], an independent parameter is added to model equation to increase the opportunity to fit the actual measured data collected

from path loss measurement. The authors succeeded to improve the accuracy of CI and FI models without increasing their complexity. Recently, with the strong development of AI, PL models based on machine learning and deep learning are widely developed [22]–[24] .These methods bring predictive results with much higher accuracy than traditional prediction models. However, the disadvantage of these methods is the requirement of a large amount of input data.

Factors affecting path loss analysis

Understanding the factors affecting the path loss is very important because this helps to analyze, control, and contribute to the estimation of the path loss value if the system is deployed. The influence of these factors is analyzed, understood, or predicted by actual measurement processes or by models and formulas. Numerous studies have been conducted to understand the influence of these factors on the path loss. Certain measurements for understanding the influence of building structure as well as buildings materials are presented in [9], [25]. For instance, in [9], a measurement building penetration loss in a New Jersey suburban residential neighborhood is presented. Measurements at three different representative houses with different material conditions were taken to be able to verify and compare the effects of these conditions on the path loss. The measurement results in the paper, presented in Figure 1-10, show that the median building penetration loss was found to be 9 dB for a home with low-loss materials and plain-glass windows, 15 dB for a renovated home with low-emissivity windows, and 17 dB for a new construction using foil backed insulation and low-emissivity windows. It can be concluded that the materials used to construct the building have a great influence on the path loss of the signal transmitted from outside to inside the buildings.

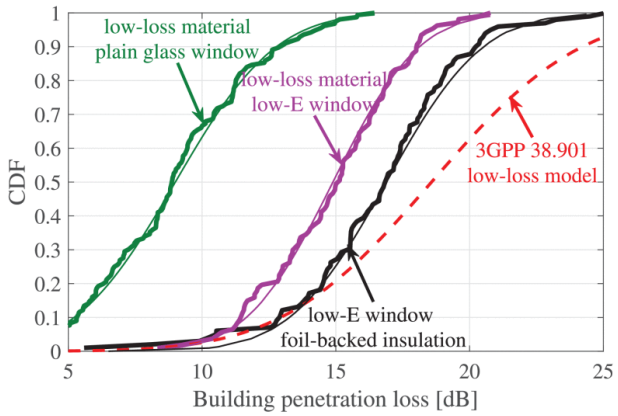

Figure 1-10. Cumulative distribution function (CDF) of measured building penetration loss for three representative single-family homes in [9]

For FWA's outdoor wave propagation, vegetations and weather are also two of the important factors affecting path loss [26]–[30]. From these studies, it can be seen that plant parts such as leaves, branches and stems that are randomly distributed in the propagation medium can cause scattering, attenuation, absorption, and diffraction of radiated waves. This greatly affects the implementation of the FWA system. For the most part, the presence of trees or forests will increase the path loss. This attenuation level depends on many factors such as foliage density and operating frequency [28], [30]. In addition to trees, weather conditions such as sun, wind, rain, snow, or seasons also affect path loss [26], [27], [29], [30]. For example, with the configuration in [27], the results show that in the case of low rainfall intensity, the main attenuation in path gain is the loss due to free space propagation, followed by rain attenuation and then the loss due to diffraction mechanism. The conclusion is not the same in the case of high rainfall rate. In this case, the main attenuation factor comes from rain attenuation, followed by free space path loss and then diffraction loss. In addition to the main influencing factors that have been presented, other factors such as the position or height of the antenna also influence the path loss [27], [31]. In [31], by adjusting the antenna height while measuring, the authors found that the height of antennas can affect the PL. In their case, higher antenna gives better coverage and more often LoS condition at 26 GHz in a rural area.

Solutions to improve path loss

After measuring, testing, calculating factors and losses, methods to improve the path loss are studied and proposed through numerous studies. In general, solutions can be divided into three main categories:

- Using high gain antennas
- Using steerable antennas
- Improving building materials

Category 1: Using high gain antennas

The Friis transmission formula in decibels can be written as (1.2):

$$P_r = P_t + G_t + G_r - PL \quad (1.2)$$

Where: P_r is wave power received (dB); P_t is wave power transmitted (dB), G_t is gain of the transmitting antenna (dB), G_r is gain of the receiving antenna (dB), PL is path loss (dB)

From the formula it can be seen that, if the path loss increases, to ensure that the power received is not reduced, we can increase the gain of the antennas, or in other words, we can use high gain

antennas to improve the problem of high path loss. Research on high gain antennas and antenna improvement methods to achieve high gain have been and are being developed [32]–[39]. In order to have an antenna with high gain, in addition to the use of traditional high gain antennas (such as horn antennas, Vivaldi antennas), methods to improve the gain of basic antennas are also developed. Two of the methods which are popularly used and have gained a lot of attention are the method using lenses [32]–[35] and the method using FSS (Frequency Selective Surface) or metamaterials to improve antenna gain [36]–[39].

The use of a lens to improve antenna gain normally relies on the principle of an optical lens: waves have a different phase velocity than they would normally have in the air, so that the lens, having a variable thickness in places, delays the waves which pass through it with different times, thereby modifying the shape of the wave front and the direction of the waves. Therefore, by constructing lenses with special shapes, it is possible to increase the antenna gain. In [32], a 3D printed dielectric lens with a height of approximately 70 mm, as shown in Figure 1-11(a), helps to increase antenna gain from 7.3 dBi to 25.2 dBi at 24.4 GHz, theoretically. Another example of a 3D printed dielectric lens is introduced in [33]. With a fairly compact size (about 23.26 mm x 21.48 mm), this lens can increase antenna gain by about 4 dB at 28 GHz, theoretically. It can be seen that dielectric lenses can help to improve antenna gain quite clearly. However, in some applications, 3D lens structures are not suitable because they are rather voluminous and do not have a flat construction. Therefore, a number of studies on flat lens structure that enhance antenna gain have been presented [34], [40]–[42]. For example, in [34], a quasi-Yagi dielectric lens antenna is introduced. In this example, holes are inserted into the extended planar dielectric lens to reduce its effective permittivity and therefore ensure that higher order modes will not be excited. This lens antenna structure reaches a realized gain of 10-13 dBi in the 27-41.25 GHz frequency band, theoretically.

Besides the lens method, other research based on FSS, and metamaterials is also increasingly being developed [36]–[39]. [36] presents a FSS array reflector which is used to increase the gain of an eight-element antenna as shown in Figure 1-11(b). The FSS reflector is designed and placed at the back side of the antenna to reflect the waves at the desired frequencies, thereby improving the antenna gain. Apart from FSS, metamaterial (MTM) structures are also used to enhance antenna gain. In [38], zero-index metamaterials (ZIMs) are added into a Landstorfer printed log-periodic dipole array (PLPDA) to resonate at 33 GHz to obtain a good gain flatness throughout the 31-36 GHz frequency range. The measurements in this experiment show that ZIMs help improve antenna gain and gain flatness. The gain is improved, from 9.1 ± 0.7 dBi

to 10.5 ± 0.5 dBi across the operating range of 26.5-40 GHz. Another example using a combination of different metamaterial patterns to improve antenna properties is shown in [39]. As illustrated in Figure 1-11(d), three pairs of MTM are used. The first pair with a high refractive index is used to provide a wide beam antenna. The second pair is added in front of the radiators to split the single wide beam into dual beam. The last pair of anisotropic MTM is incorporated to improve the gain performance. This structure helps the antenna to achieve a maximum gain of 7.4 dBi at 26 GHz and a gain improvement of 4.2 dB compared to the wide beam antenna.

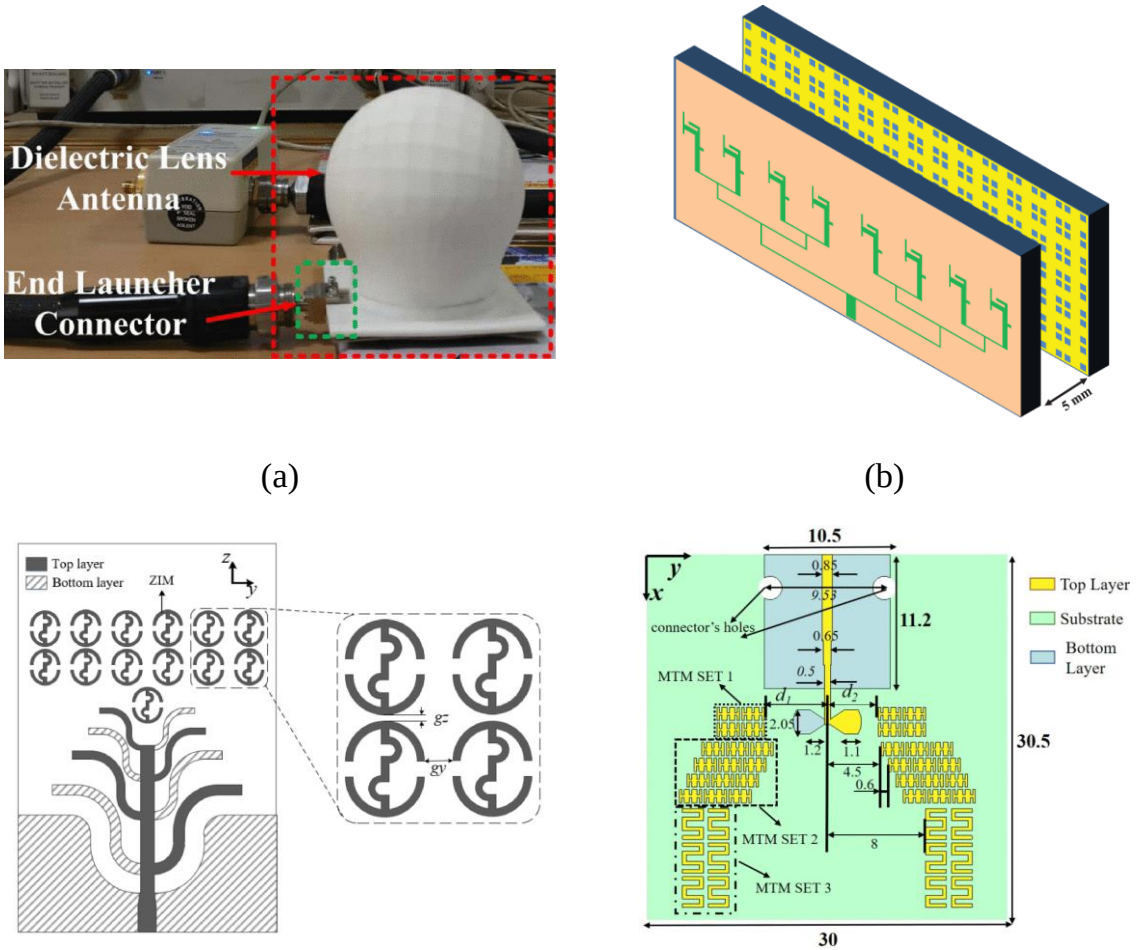

Figure 1-11. (a) 3D printed dielectric lens fed by microstrip patch antenna [32] (b) Array antenna with frequency selective surface [36] (c) Landstorfer printed log-periodic dipole array antenna with ZIMs [38] (d) Bowtie antenna with metamaterial [39]

In addition to focusing on increasing antenna gain, there are also numerous studies introducing high-gain antennas with some special properties to solve other 5G FWA issues in different special applications [43]–[52]. For instance, in 5G FWA, having a strong anti-interference is

also one of the highly appreciated properties. Therefore, in addition to exhibiting high gain, many antennas for 5G FWA are also designed to achieve high isolation, which indicates anti-interference capability [43], [47]. In [43], a slot-fed ME-dipole antenna subarray, which is excited by a high-order mode cavity, is presented. As shown in Figure 1-12(a), by using two vertically arranged slotted SIW feeding networks to feed the high-order mode cavity, the system achieve a high isolation (45 dB) besides a high gain (25.8 dBi) in a wide frequency band (36.8-42.6 GHz). In [47], by using an orthogonal differentially fed structure instead of feeding lines and shorting pins, the antenna system exhibits a high port isolation of 37 dB. In these two examples, in addition to high gain and high isolation, the antennas in these two examples are also designed to be dual polarized as well. This is also a property that is appreciated in some 5G FWA applications as it helps to avoid signal collisions and increase the traffic handling capacity of the system. Another property which is also appreciated in many other examples of 5G FWA is the antenna's ability to operate dual-band, multi-band, or broadband. This ability, in some applications, enables the antenna to operate in multi-frequency spectrum or in a wide frequency spectrum with a single antenna, thereby saving the system components. Thus, there are many antennas for 5G FWA applications that have both high gain and dual-band, multi-band or broadband capabilities [44], [48]–[51]. For example, the antenna in [44], depicted in Figure 1-12(b), is designed to operate at 28 GHz, 33 GHz and 38 GHz. By modifying the stub length and the patch antenna geometry based on a Franklin antenna array, the authors obtained an antenna configuration that can operate at all three frequencies. Another useful feature that needs to be mentioned in some applications is the narrow beamwidth and low sidelobe. The characteristics of beamwidth and sidelobe can be considered as two of the evaluation criteria for a directive antenna. An antenna with a narrow beamwidth and low sidelobes will have good directivity and low interference, especially in antenna arrays. Such antennas are suitable for antenna arrays or beamforming, beam scanning systems. Figure 1-12(c) presents an example of a narrow beamwidth and low sidelobe level antenna designed in [45]. Figure 1-12(d) shows a slightly different example compared to Figure 1-12(c). In this example, the authors attempted to improve the sidelobe level of an omnidirectional antenna array by controlling the power distribution on each element of the antenna array. In this way, the system achieves a low sidelobe level, which is less than -15 dB.

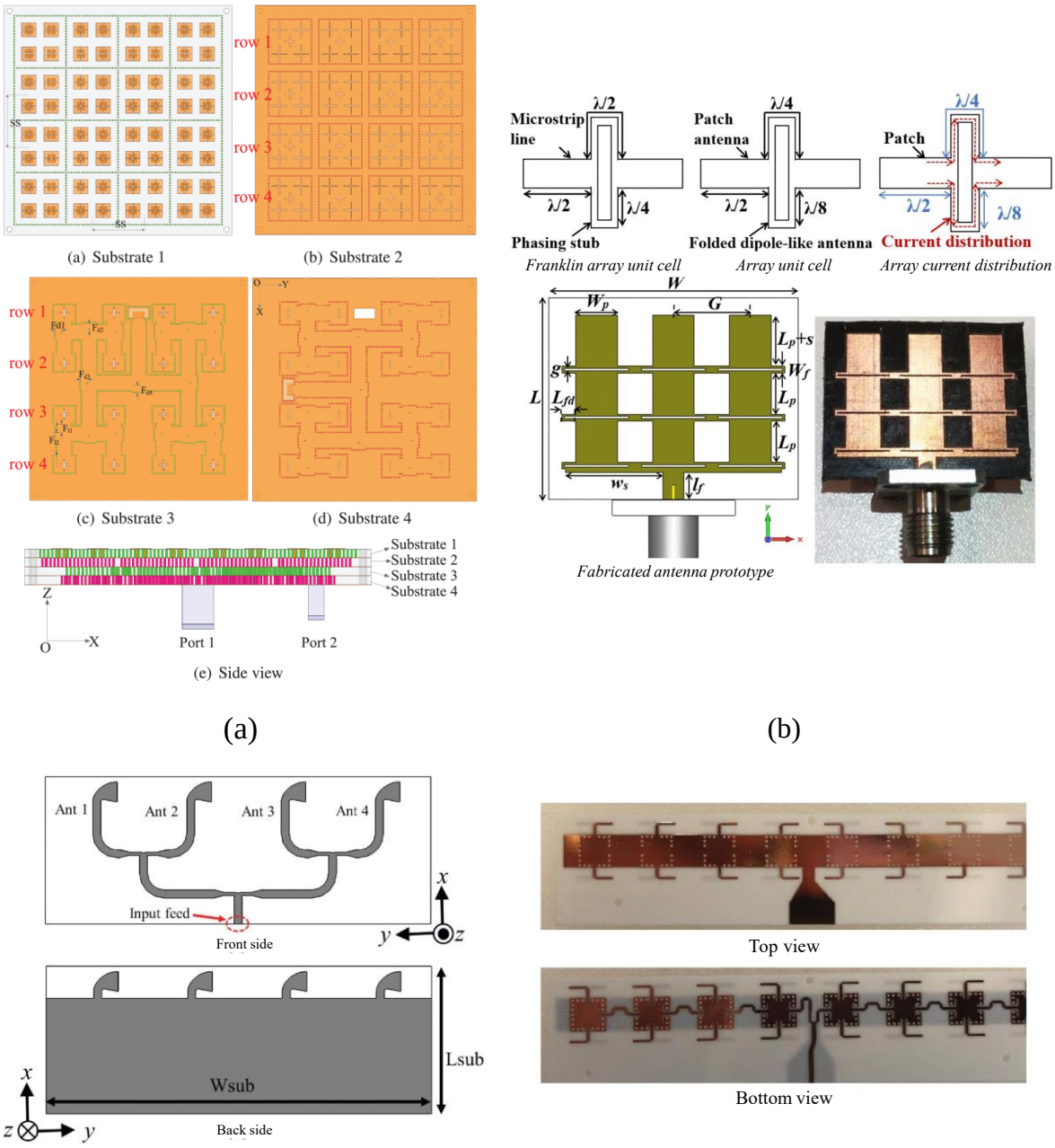

Figure 1-12. (a) Dual linearly-polarized, high gain and high isolation antenna array [43] (b) Multiband 2-D array based on enhanced Franklin antenna [44] (c) High gain and wideband narrow-beam antenna [45] (d) Planar array antenna with reduced sidelobes [46]

Overall, a high gain antenna is a good solution to the path loss problem. This solution is increasingly attracting attention and is being now well developed. Gain enhancement can be accomplished through many methods such as the addition of lenses or the use of FSSs or MTMs. In addition to achieving high gain, several other properties such as dual polarization,

high isolation, narrow beam, low sidelobe level or multiband are also considered when designing specific applications.

Category 2: Use steerable antennas

As discussed in the previous sections, in FWA system, a base station will be used to accommodate various CPEs in the space. In theory, the base station antennas should be omnidirectional to handle various CPEs simultaneously. However, the omnidirectional characteristic presents a low gain and scatters the antenna energy in all directions. This makes the path loss issue more important. To solve this problem, a widely used solution today is the beamforming (BF) technique. Beamforming steers the majority of signals generated from an array of antennas to an intended angular direction [53]. Beamforming is usually used with Multiple Input Multiple Output (MIMO) to focus the wireless signal in a specific direction, as shown in Figure 1-13. MIMO can be defined as a wireless technology in which multiple antennas are used both at the source (transmitter) and at the destination (receiver) to exploit multipath propagation. In general, BF technique can help increase the Signal to Interference and Noise Ratio (SINR) for intended user and provide advantages for the system such as higher system capacities, lower transmission power, and a higher frequency re-use factor within a given area [54].

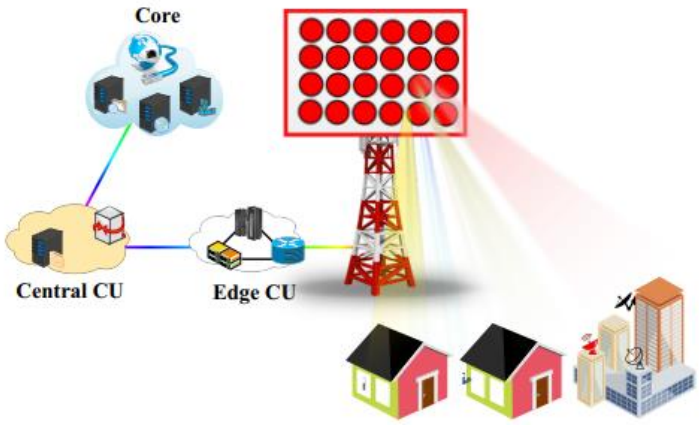

Figure 1-13. FWA network using Multiple Input Multiple Output and beamforming [3]

BF has evolved from one-dimension (2D) to three-dimension (3D) [54], whereby it covers not only the space in the horizontal direction but also in the vertical direction. 2D BF employs linear array antennas in which elements are arranged in a straight with a calculated distance apart. Because of such structural limitations, a linear array can only generate beams in one dimension,

vertical or horizontal. That means, it can only distinguish users at different angles of the same vertical or horizontal plane but cannot distinguish users on both planes at the same time. Therefore, 2D BF cannot take full advantage of the 3D spatial domain [54]. However, the structure of the linear array in 2D BF is quite compact in terms of space and simple in terms of control. Thus, 2D BF with linear array is still widely used, especially in applications with spatial limitations in one dimension, for example in phones and CPE devices. To overcome the disadvantages of 2D BF operating range, 3D BF has been developed by using two-dimensional rectangular arrays, or sometimes called planar arrays. 3D BF becomes more and more attractive in MIMO systems with the capacity of steering to any angle within the specified range of the system. The MIMO concept has evolved from multi-user MIMO (MU MIMO) to massive MIMO (mMIMO), where the numbers of antenna elements in the base station system can reach hundreds or thousands [53]. 3D beamforming mMIMO become a key factor in 5G FWA. Using a large number of antennas in mMIMO helps reduce uncorrelated noise and fast fading, create narrower and highly directive beams. This helps the system obtain a sufficient signal-to-noise-ratio (SNR) to overcome high path losses and improve spectral and energy efficiency, leading to higher capacities and better cell edge coverage.

BF can be divided into three main categories: analog BF, digital BF, and hybrid BF, as shown in Figure 1-14. Analog BF uses a single common RF (Radio Frequency) source and a splitter among multiple antenna elements. The beam is controlled by adjusting analog phase shifters along the RF path. The advantage of analog BF is simple, low cost and low power consumption. However, this type of BF is not flexible because it has a low degree of freedom and there is only one data stream between transmitter and receiver. Meanwhile, in the digital BF system, each antenna has a dedicated RF signal and path. Phases and amplitudes are digitally controlled by baseband processing. Hence, digital BF presents a higher flexibility with a high degree of freedom, providing a good beam control and can provide multiple data streams in wireless communication. However, this technique suffers from high power consumption and high cost due to the large number of RF chains. Especially with the huge number of antennas in mMIMO, digital BF deployment becomes difficult and expensive. Therefore, hybrid BF was proposed as a combination of analog BF and digital BF to reduce the number of RF chains. This will help the system reduce energy consumption while maintaining flexibility.

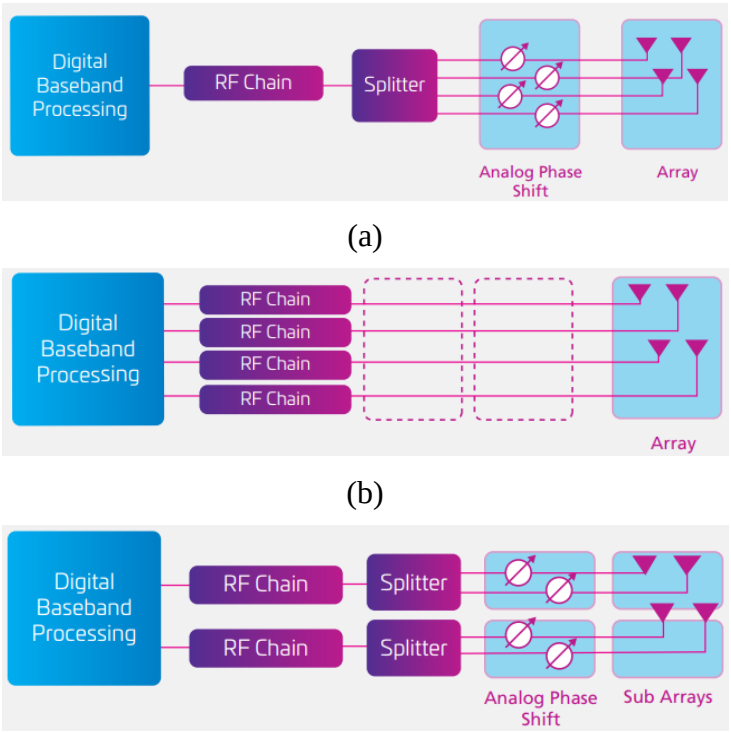

Figure 1-14. Structure of (a) Analog BF (b) Digital BF (c) Hybrid BF [55]

In a basic analog BF, each antenna is connected to a phase shifter to ensure that the phase difference is the same between two adjacent antennas. A signal is then applied to each branch. By controlling this signal and the phase difference between the antennas, a beam with a defined direction will be formed. In a digital BF, a technique called precoding is used to combine beams of antenna elements, so their superimposed emissions from all elements produce beams along multiple desired paths simultaneously. Both techniques require the construction of a relatively complex system which may occupy a large volume of space. Therefore, these two techniques, as well as hybrid BF, are often used in large systems or base stations. However, in small systems like CPE or compact mobile devices, it is quite difficult to build such complex systems. Thus, efforts are made to create beam former antenna systems, or sometimes called steerable antennas, without having to build an entirely complex system. These studies often result in a switched beam system rather than an adaptive BF system. However, this is usually sufficient for small applications. Switched beam systems create fixed beam patterns [56]. On the contrary, the adaptive BF technique synthesizes beams in arbitrary directions of interest while simultaneously cancelling interfering signals in unintended angles of direction.

One of the simplest and most compact BF systems is the Rotman lens-based BF system [57]. This lens allows forming different beams without the need of switches or phase shifters. The

Rotman lens-based BF system of [57] is presented in Figure 1-15(a). A basic Rotman lens consists of a set of input ports (array ports) and output ports (beam ports) arranged along an arc, and a parallel plate region. Dummy loads can also be connected on two sides of the plate region, which serve as absorbers to reduce multiple reflections and standing waves. The principle of Rotman lens is inspired by the principle of optical lenses, which focus light by means of refraction. In a microstrip Rotman lens, the signals are injected into the plate region through the input ports. The phases of input signals are passively shifted after passing the plate region and output ports. These shifted signals are finally used to excite a linear antenna array to form a beam with a desired pattern. The form of the plate regions and the lengths of the transmission lines are carefully calculated to produce a wavefront across the output that is phased by the time-delay in the signal transmission [58]. When one of the beam ports is excited, a tilted beam is radiated from the antenna array. By switching between input ports, the radiated beam can be scanned.

Another compact BF system that has been developed is the resonant cavity antenna (RCA) system [59], [60]. RCAs are made of a partially reflective surface (PRS) placed at a proper distance above a ground plane, surrounding a radiator or an array of radiators that feeds the entire structure [59]. Figure 1-15(b) presents the general structure of RCA in [60]. The PRS is designed to produce a frequency scanning capability for the whole system. Frequency scanning systems are used to develop multiple access techniques when the frequency domain is shared among multiple users. By doing this way, power consumption or bit error rate can be reduced by using the spatial diversity option in the user management system and assigning different frequencies to different users. Therefore, more users can be served at the maximum antenna gain, while the propagation loss is low [60]. In [60], the unit cell is designed to provide low-to-high reflection phase variation over frequency, easily adjustable over the desired frequency scanning. The use of metallic wall in this example is used to create the unidirectional scanning ability for the system.

Besides the above two methods, the mechanical control can also be used to perform beamforming function. As shown in Figure 1-15(c), [61] proposes dipole antennas with mechanically steerable main beam. This system consists of a bent dipole antenna placed a distance H above the reflector layer. The paper shows that changing H will change the direction and gain of the main beam. In other words, steering angle and gain could be controlled by mechanically changing distance between the dipole and the reflector. The merit of this

technique is that a BF system can be achieved in a simple antenna design that has minimal additional components.

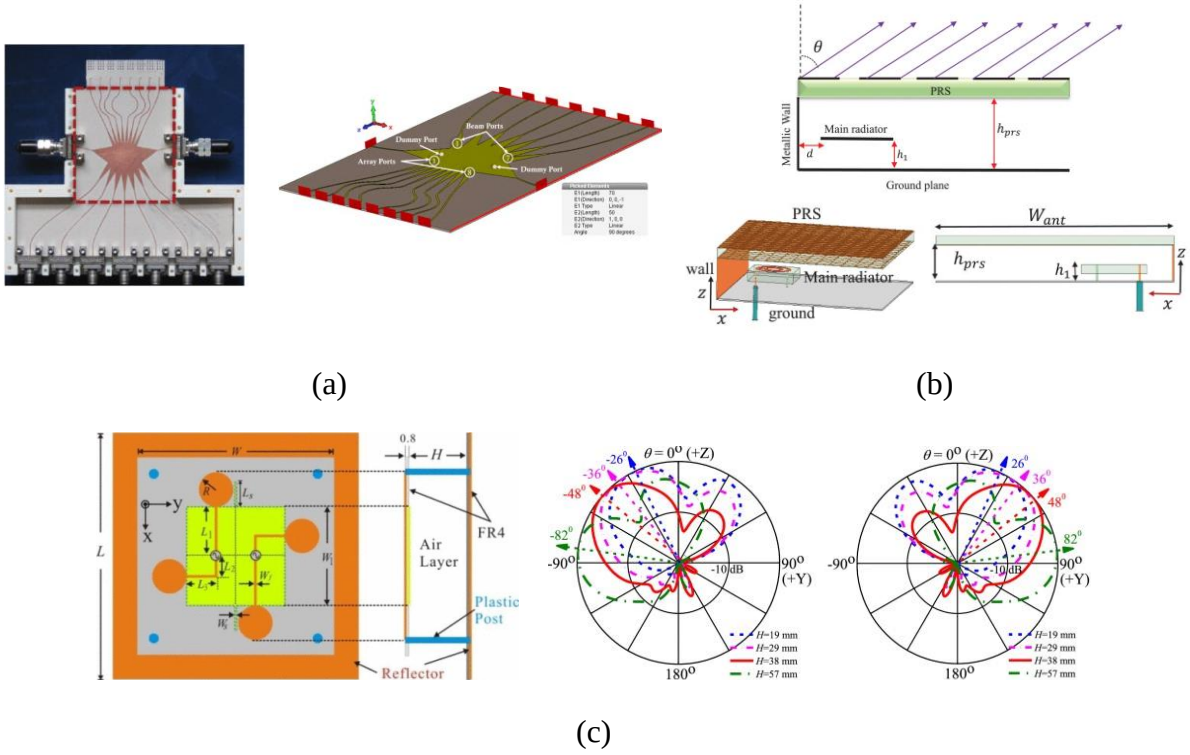

Figure 1-15. (a) Rotman lens-based beamforming system [57] (b) Resonant cavity antenna [60] (c) Mechanical steerable antenna [61]

Category 3: Improve materials of buildings

As mentioned in the previous section, wireless signals are rapidly attenuated when passing through buildings. Short wavelengths like high frequencies used in 5G are very easy to be blocked or reflected by standard building materials, making it difficult to establish and maintain a link between a nearby 5G FWA tower and CPE in buildings. One of them, which has the reputation of greatly attenuating wireless signals is low-emissivity (low-e) glass. The low-e glass was made with the purpose of minimizing the passage of infrared and ultraviolet light, thereby minimizing heat loss for the whole building. A basic low-e glass consists of glass layers and metallic microscopical thin films, which are optically transparent and reflect heat, coated on the surface of glass, between glass layers. While very effective at blocking heat loss, these metallic films also inadvertently block many wireless signals. In order to improve this issue while retaining thermal resistance, many methods have been proposed. One of the most promising approaches is the use of metasurface. For instance, as presented in Figure 1-16(a), the authors in [62] propose an air-connected structure, which means removing the vertical and

horizontal metal lines, with a defined period, instead of a full metallic coating. The use of this structure allows wireless signals to pass through. However, data concerning the ability to block light in the invisible band when using the metasurface coating are not mentioned in this paper.

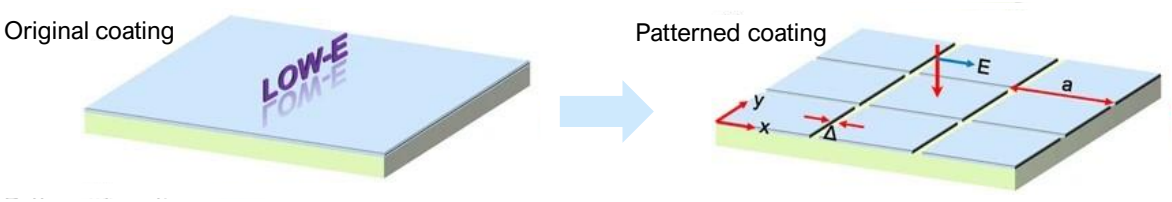

(a)

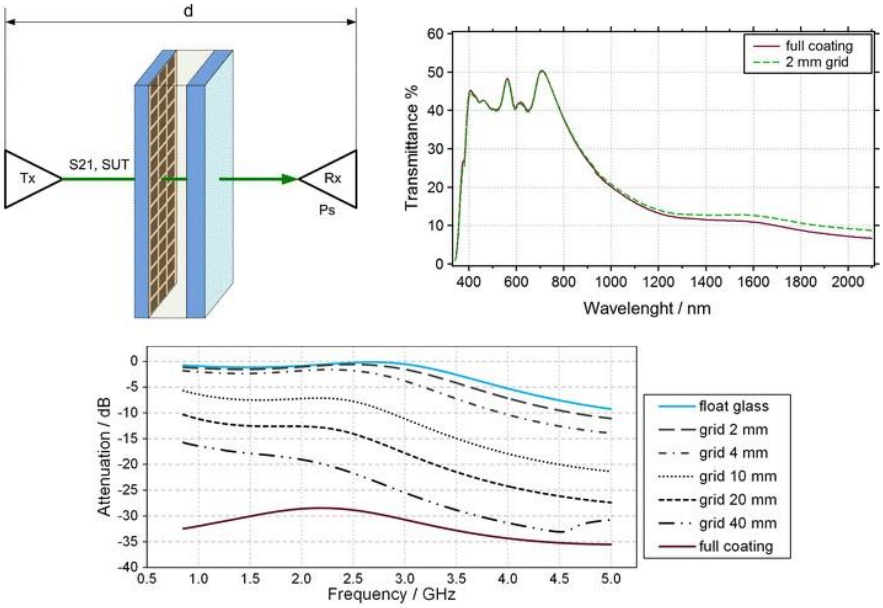

(b)

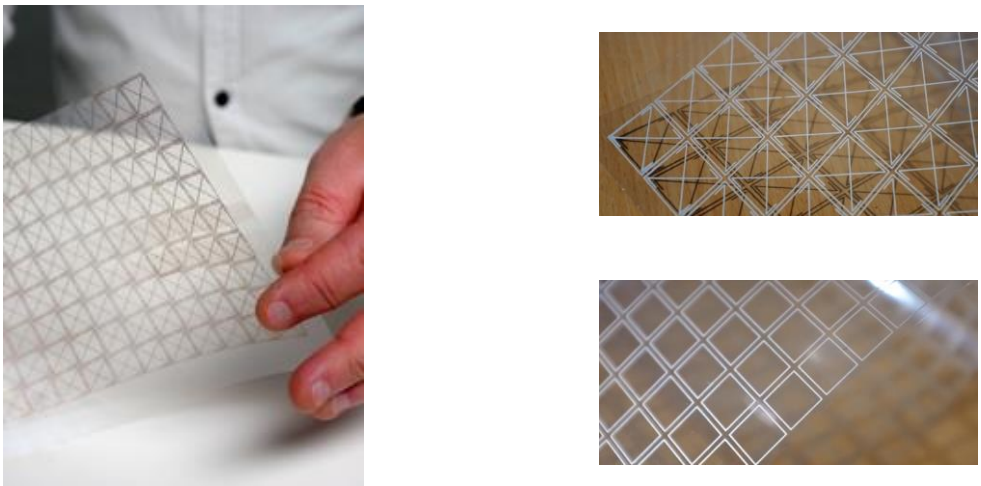

(c)

Figure 1-16. (a) Low-e material covered by full metallic film and air-connected pattern [62] (b) Metasurface coating to replace the full metallic coating of a double-glazing glow-e window in [63] (c) Printed FSS plastique film of Lichens with different patterns to improve transmission signal through low-e glass

In [63], a metasurface coating is designed to replace the full metallic coating of a double-glazing low-e window as presented in Figure 1-16(b). With a suitable pattern, the metasurface coating can achieve a visible light blocking capacity similar to a full metallic coating while exhibiting a good transmittance as an uncoated double glazing (float glass) in the 1-5 GHz frequency band. However, in the examples above, the metasurface coatings are all newly fabricated. It means that the entire window needs to be re-fabricated, especially with double-layer windows, which are becoming more and more popular in the market. This is very disadvantageous for buildings that have installed low-e glass because replacing all glass doors is very expensive and time consuming. Therefore, a new solution was developed: adhesive printed film. Figure 1-16(c) presents some adhesive printed films which are presented by the Lichens company. These films are fabricated with selected Frequency Selective Surface (FSS) patterns, thereby improving the transmission of high frequency waves through the low-e glass. The films are completely passive and do not require any external power supply. They are also very flexible. Users simply attach the film to the glass door surface to use and remove the film, if necessary, rather than replacing the whole glass door.

1.3. Thesis Overview

As discussed in the previous sections, the key issue in 5G FWA is to maintain an acceptable level of losses. To solve this issue, many solutions can be used, such as using high gain antennas, using beamforming techniques, and improving building materials.

In this thesis, we focus on the first two solutions: using high gain antennas and beamforming techniques. These methods are built on the basis of applications for compact devices such as mobile devices or CPEs rather than large range applications such as station antennas.

With the solution of using high gain antennas, we explore and propose methods to increase the gain of a Vivaldi antenna while keeping its flat and compact structure. Two proposed and implemented methods are presented in Chapter 2. These antennas are built to operate in the Ka-band (26-40GHz). The Ka-band covers many mmWave bands used for 5G FWA research. To improve antenna gain while preserving the planar structure, we focused on developing flat lens constructions. The first method is based on the substrate lens and quasi-SIW (Substrate Integrated Waveguide) structure. Usually, the SIW architecture is used as a low-loss transmission line, as it is considered as a waveguide integrated in the substrate. So, we take advantage of a SIW-based structure and a substrate lens to increase the gain of the antenna as well as to explore other applications where SIW could be involved. The second method is based

on PCL (Phase Compensation Lens). This approach has been used in several studies. However, according to the author's knowledge, the PCL design process as well as its disadvantages are generally not clearly presented. Therefore, in the last part of Chapter 2, we propose a PCL design process by leveraging popular software such as CST Studio and MATLAB.

Next, in Chapter 3, we focus on beamforming techniques, based on FSS on a 3D surface. For the loss caused by the influence of building materials, besides improving the building materials, the use of outdoor CPE is also a good solution. Outdoor CPE are devices placed outdoors, near buildings or offices, used to support communication between inside and outside the building, especially in cases where low-e glass window is present. However, this also means that outdoor CPEs are affected by environmental factors such as rain and wind. To protect the electronic circuits inside, CPEs are equipped with a shell, usually called “radome”, which is normally sealed and waterproof. Radome is a weatherproof structural enclosure used to protect wireless communication systems and is almost transparent to electromagnetic waves. The primary function of a radome is to protect the internal system. This is relatively wasteful because in many cases, the radome occupies a certain space while having only a single function. Thus, in our study, we propose to print FSS structures on the surface of the radome. Therefore, the radome can both protect the internal system and regulate the system's radiation. Some similar studies have also been done; however, these studies are usually performed on 1D surfaces instead of 3D, while protective covers generally do not have a simple planar structure. To carry out the printing of FSS patterns on the radome surface, we use the direct jetting technique, which is especially efficient on 3D planes. This is a newly developed technique which has many advantages compared to equivalent printing techniques. To add a function while retaining the circuit protection function of the radome, FSS patterns need to be printed inside the radome. However, due to current technical limitations, the print head is still too big. To be able to print inside the radome, we need a semispherical radome with a radius of at least 1-2 m. This is too large and difficult to study in the laboratory. So, in our study, we will only use small radomes (with a radius of 10 cm) and the FSS patterns will be printed on the outer surface of the radome. In this section, designs will be done at the center frequency of 3.6 GHz - one of the 5G FWA frequencies being deployed civilly.

Finally, in Chapter 4, we present research on a future trend - the use of biosourced substrates. Nowadays, most electronic systems use common substrates like FR4 or Rogers. They are effective substrates. However, they are produced from fossil resources, which are not environmentally friendly due to their low recyclability, as the production and recycling process

is energy intensive. In the context of environmental pollution and its increasingly serious consequences, actions to protect the environment need to be reinforced. Therefore, the application of biosourced substrates to consider the possibility of replacing traditional substrates should be of interest. In this chapter, we will use paper substrates to design and fabricate composites, such as antennas or lenses, for applications in 5G FWA.

Chapter 2. High Gain Vivaldi Antenna – Two Methods to Enhance the Antenna Gain

The main objective of this chapter is to propose two methods to improve the gain of a directive Vivaldi antenna which operates in the Ka-band (26–40 GHz). The first method is based on quasi-SIW (Substrate Integrated Waveguide) and substrate lens, while the second method is based on phase compensation lens. The advantages and disadvantages as well as the comparison of these two methods will be discussed.

2.1. Overview

As mentioned in the first chapter, Ka-band (26–40 GHz) is one of the bands that receiving attention in the discovery and development of 5G. However, this frequency band is quite large. Therefore, to work well across the entire band, wideband antennas are preferred, and one of the most prominent among them is the Vivaldi antenna. Vivaldi antenna was first introduced by P.J. Gibson [64], belongs to the end-fire traveling antenna family. Vivaldi antenna is famous for its wide bandwidth, high radiation efficiency and good directional radiation. In many 5G applications, high gain antennas are very popular to overcome the high path loss issue. Therefore, improving antenna gain, in this case the Vivaldi antenna, received a lot of attention.

A common way to improve antenna gain is to use a dielectric rod, as illustrated in Figure 2-1, to direct the radiated wave, thereby helping to improve the gain [65] [66]. In [65], a uniform polystyrene rod, which is considered to work as a traveling wave antenna, is fabricated. This rod includes three parts: a launcher section, a propagation section, and a radiation section. A 75 mm rod gives a gain improvement of 3 dB on average in the 6-8 GHz frequency band. Another cylindrical dielectric rod, consisting of two different dielectric materials, is presented in [66]. The combination of two different dielectric layers, ensuring that the dielectric constant of the inner layer is greater than that of the outer layer, helps to confine the high frequency energy close to the inner core layer. Using this technique, a 35 mm rod improves antenna gain by 2-4 dB throughout the 7-13 GHz frequency band. The method of using dielectric rods is simple and provides a high gain enhancement, but the entire antenna system becomes bulky and not flat, making it difficult to integrate with other microstrip systems.

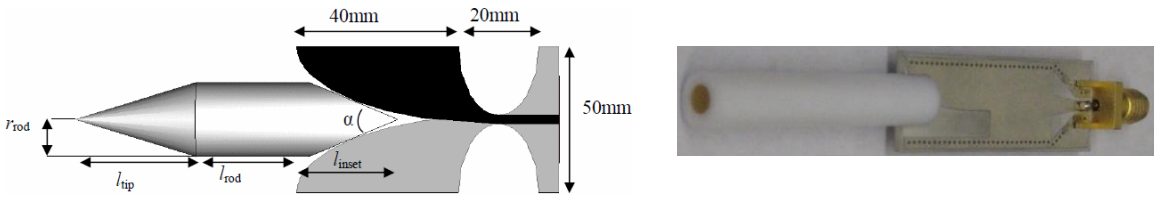

(a) (b)

Figure 2-1. (a) Ultra-wideband antipodal Vivaldi antenna with protruded polystyrene rod [65] (b) Ultra-wideband antipodal Vivaldi antenna with two-layer rod [66]

With the aim of providing a technology that maintains an integrable system, flat dielectric lenses of various shapes have been well developed [42], [67], [68]. [67] introduces a dielectric lens replacing a portion of the substrate in antenna aperture. By using a higher dielectric constant than the antenna substrate and an exponential shape, the dielectric lens in [67] produces a gain improvement of around 2 dB in the 2-14 GHz frequency band. In [68] and [42], the authors used the same antenna substrate with different shapes to create lenses instead of using another material. In this way, the antenna structure is more robust than in [67]. The lenses in these two papers improve antenna gain in the whole frequency range and specially at high frequencies. The gain enhancement range is about 0-10 dB in the 5-50 GHz frequency band in [68] and about 0.5-7.5 dB in the 3.4-40 GHz frequency band in [42].

(a) (b) (c)

Figure 2-2. (a) Vivaldi antenna with exponential dielectric lens [67] (b) Vivaldi antenna with elliptical dielectric lens [68] (c) Vivaldi antenna with trapezoidal lens [42]

To take advantage of dielectric lens surface, lenses based on the metasurface and phase adjusting unit cell were developed. These techniques implement microstrip patterns, thus making it possible to effectively use the surface of dielectric lenses to improve antenna gain without increasing the difficulty of antenna fabrication. Figure 2-3 introduces some examples of lenses using these two techniques [69]–[72].

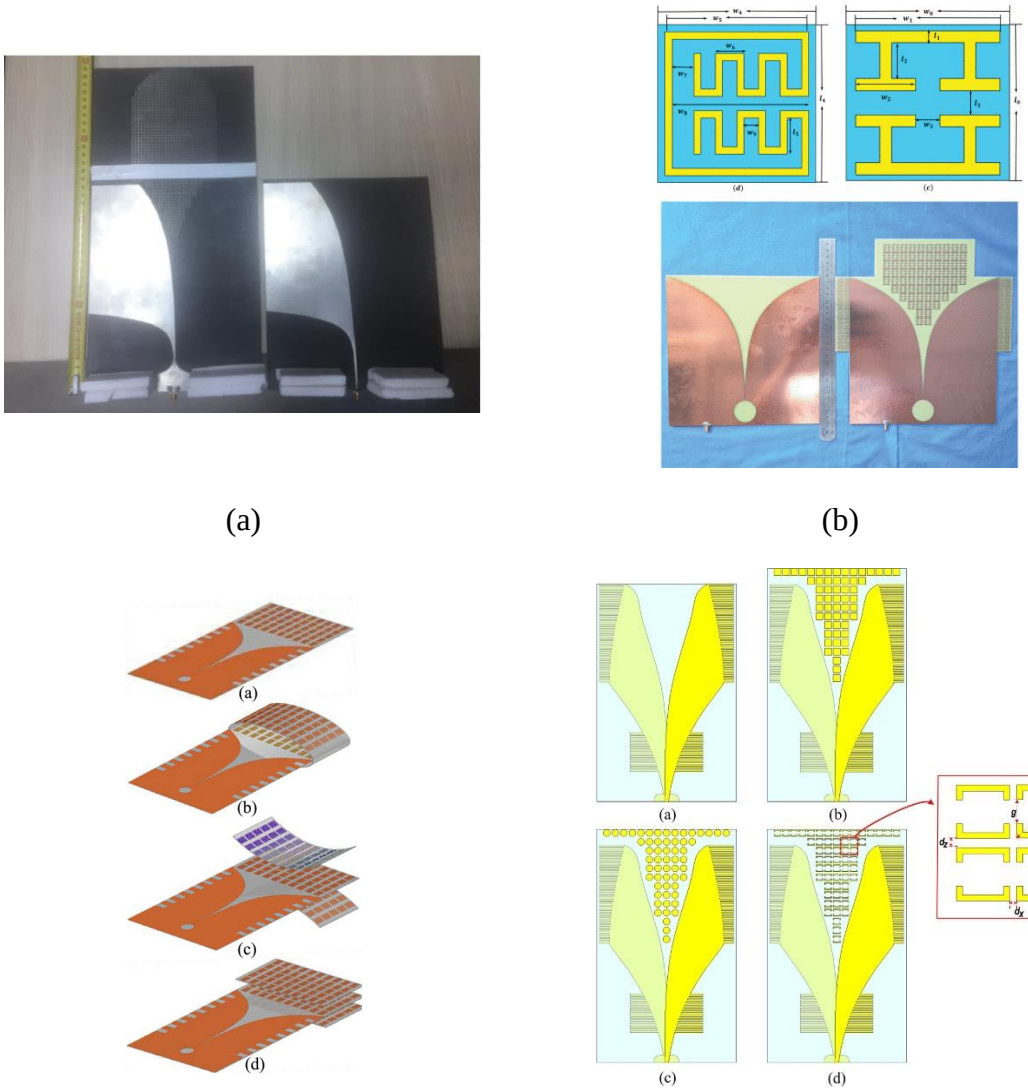

Figure 2-3. (a) UWB metasurface lens for an antipodal Vivaldi antenna [69] (b) Vivaldi antenna with artificial material lens and sidelobe suppressor [70] (c) UWB Vivaldi antenna with phase adjusting unit lens [71] (d) Modified antipodal Vivaldi antenna with a phase compensation lens [72]

In [69], the topology named “capital I with stroke (CIWS)” for unit cell is used to create a high permittivity metasurface. In [70], an artificial material lens is designed to create a transmission effect and a focusing effect on electromagnetic waves. In addition to the metasurface technique, phase compensations lenses are also considered. In [71] and [72], different types of phase adjusting unit cells are used to create lenses with the aim of correcting the electric field phase to improve antenna gain.

Above are some techniques which have been and are being used to improve the gain of Vivaldi antennas. Based on these theories, two methods are proposed in this chapter to enhance Vivaldi antenna gain:

- Method 1: Also based on the use of the dielectric lens, the quasi-SIW structure is integrated in the dielectric lens to direct the electromagnetic waves to increase antenna gain.
- Method 2: This method is based on the phase compensation lens (PCL). PCL is an interesting new way to enhance antenna gain. In this chapter, a comprehensive study of how to construct a PCL by leveraging simulation software like CST Studio is presented.

An overview of several gain improvement methods for Vivaldi antennas, as well as the two suggested methods which will be presented in this chapter, has been introduced. In the following sections, the antenna design will be detailed. First, the original antipodal Vivaldi antenna will be designed at the Ka-band. Then, two methods for improving antenna gain will be constructed based on this original antenna. All antennas in this chapter are designed on a 0.6 mm thick RO4003C substrate with a dielectric constant of 3.55 to operate in the Ka-band (26-40 GHz).

2.2. Original Vivaldi Antenna

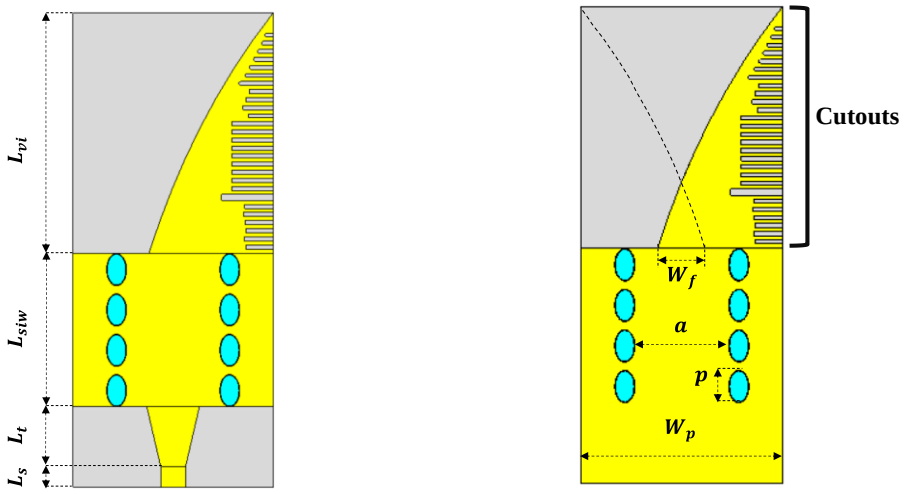

(a) (b)

Figure 2-4. Structure of proposed original Vivaldi antenna (a) Top view (b) Bottom view

The proposed original Vivaldi antenna structure is presented in the Figure 2-4. This antenna is composed of two major parts: (1) SIW transmission line and (2) the radiation part.

2.2.1. SIW Transmission Line

2.2.1.a. Basic theory of SIW

SIW (Substrate Integrated Waveguide) was introduced in [73]. The idea of this structure is to integrate the rectangular waveguide (RWG) structure into the dielectric substrate. The general structure of SIW is shown in Figure 2-5. This structure consists of metal holes of diameter *d*. These metal holes are placed in two parallel rows with a distance of *a*. In each row of metallic holes, the holes are arranged cyclically, the distance between two adjacent holes is *p*. In this way, the rectangular waveguide structure has been integrated into the substrate, allowing connection to other integrated systems using microstrip technology. SIW structure is increasingly favored as a transmission line because of its flat structure and lower losses than traditional microstrip line.

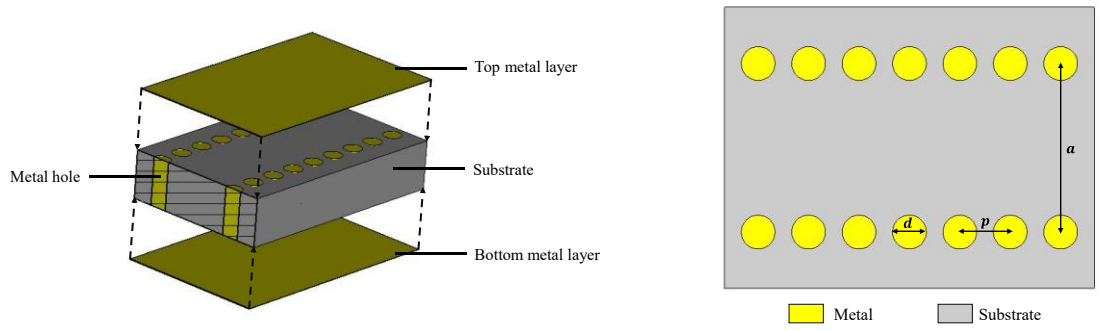

(a) (b)

Figure 2-5. SIW structure (a) Expanded 3D view (b) Cross section of substrate

The transmission characteristics of SIW are roughly equivalent to those of RWG when the radiation losses through the apertures is small enough. To ensure that, conditions (2.1), (2.2) and (2.3) must be met during the design process [74].

$$p > d \tag{2.1}$$

$$p/\lambda_c < 0.25 \tag{2.2}$$

$$p/\lambda_c > 0.05 \tag{2.3}$$

With $\lambda_c = \frac{1}{f_c\sqrt{\varepsilon_r \varepsilon_0 \mu_0}}$, f_c is the cutoff frequency of the structure.

Condition (2.1) states that the distance between two consecutive holes must be greater than the diameter of each via hole, then the circuit can be physically implemented [74]. Condition (2.2) helps to avoid band gap [74]. The last condition (2.3) ensures that the mechanical stiffness of

the circuit will not be adversely affected by the SIW structure by limiting the number of via holes per wavelength [74].

When the conditions are guaranteed, the SIW structure can be modeled equivalent to the RWG, this relationship can be expressed through formulas (2.4) [7].

$$a_{RWG} = a - \frac{1.08d^2}{p} + 0.1\frac{d^2}{a} \tag{2.4}$$

Where, a_{RWG} is the width of the RWG.

2.2.1.b. SIW transmission line of proposed antenna

Based on the above basic theories, the SIW transmission line for the proposed Vivaldi antenna in the Ka band is designed. The original transmission line, presented in Figure 2-6(a), uses a SIW structure with rectangular holes. This form reduces losses compared to circular holes [75]. However, due to manufacturing limitations, namely the impracticability of creating rectangular via holes, the shape of the holes was modified to an oval shape as shown in Figure 2-6(b). The dimensions of the transmission line are listed in the Table 2.

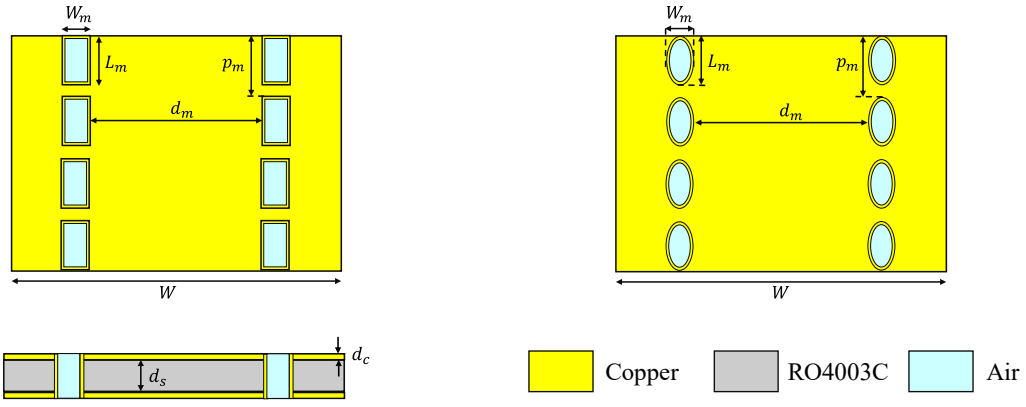

(a) (b)

Figure 2-6. SIW transmission line of the proposed antenna (a) Top view and cross-section view of original rectangular SIW (b) Top view of oval SIW

Table 2. SIW transmission line dimensions

Parameters	W_m	L_m	p_m	d_m	W
Values (mm)	1	1.6	2	4.6	9.9

To connect the antenna with other microstrip systems, a 50 Ohm microstrip line is needed. However, the propagation mode within the microstrip line is Quasi-TEM [76], whereas the

propagation mode within the SIW structure is a TE mode. To connect the SIW structure to the microstrip line with minimized losses, a conversion structure is necessary. The conversion structure used in our design has the taper shape as illustrated in Figure 2-7.

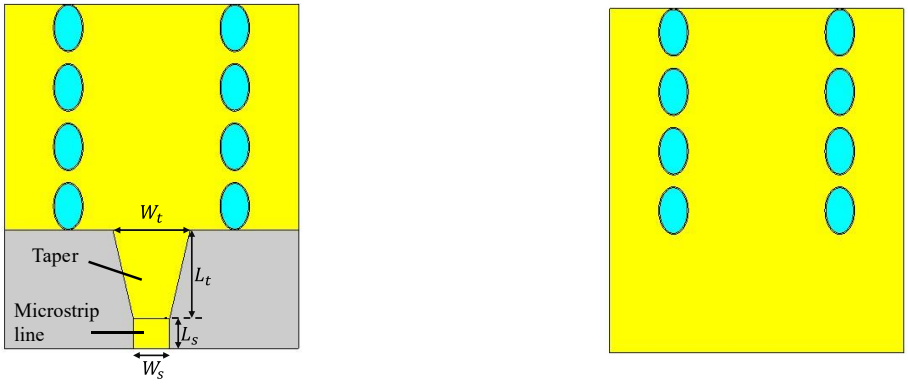

(a) (b)

Figure 2-7. SIW connected to microstrip line using taper structure (a) Top (b) Bottom

The dimensions of the taper are calculated as follows [77]:

- $L_t = k.\frac{\lambda}{4}$ (k=1,3,5, 7…; λ is the wavelength)
- W_s: Microstrip line width
- W_t: Determined by solving the equation $X_1 = X_2$ with

$$X_1 = \begin{cases} \frac{60}{\eta h} ln\left(\frac{8h}{W_t} + \frac{0.25W_t}{h}\right) & if\ \frac{W_t}{h} > 1 \\ \frac{120\pi}{\eta h\left(\frac{W_t}{h} + 1.393 + 0.667ln\left(\frac{W_t}{h} + 1.444\right)\right)} & if\ \frac{W_t}{h} < 1 \end{cases} \quad (2.5)$$

$$X_2 = \frac{4.38}{a} exp\left(-0.627 \frac{\varepsilon_r}{\frac{\varepsilon_r + 1}{2} + \frac{\varepsilon_r - 1}{2\sqrt{1 + \frac{12h}{W_t}}}}\right) if\ \frac{W_t}{h} > 1 \quad (2.6)$$

$\eta = \sqrt{\mu_0/\varepsilon_0}$ (with $\mu_0 = 4\pi.10^{-7}$, $\varepsilon_0 = 8.854.10^{-12}$) is the impedance of the vacuum medium, ε_r is the substrate dielectric constant, h is the thickness of the substrate, a is the equivalent width of SIW structure [78].

The dimensions of the taper and the microstrip line are presented in Table 3.

Table 3. Dimensions of taper and microstrip line

Parameters	W_t	L_t	W_s	L_s
Values (mm)	2.6	2.99	1.22	1

2.2.2. Vivaldi Structure

Vivaldi antennas can be divided into three types: classical, antipodal, and balanced antipodal (BAVA) as shown in Figure 2-8.

(a) (b) (c)

Figure 2-8. Three types of Vivaldi antennas (a) classical (b) antipodal (c) balanced antipodal [79]

In the classical Vivaldi antenna structure, the two radiating elements are on the same plane of the substrate layer as depicted in Figure 2-8(a). This type of antenna can be powered using aperture coupling. However, this feeding technique is rather complicated. To address this issue, Vivaldi antennas with radial symmetry, called antipodal Vivaldi antenna, is proposed. This type of Vivaldi antenna has one radiant element on the top and one on the bottom of the substrate as shown in Figure 2-8(b). Antipodal Vivaldi antenna can be easily powered by microstrip lines or directly powered by the power supply port. The balanced antipodal Vivaldi antenna (BAVA) consists of three metal layers as presented in Figure 2-8(c). This structure can be built from an antipodal Vivaldi structure by adding a dielectric layer to the top surface of the structure and then adding a metal layer with the same structure as the lowest layer. In an antipodal Vivaldi antenna, due to the absence of planar symmetry, the antipodal structure radiates an electric field which is not completely linearly polarized. Using a structure with three metal layers as in BAVA helps restore the planar symmetry. However, the manufacture of BAVA is quite complicated with two-layer structure. In order to obtain good radiation characteristics, but not too difficult to design and manufacture, the antipodal Vivaldi structure is chosen. The complete structure of the Vivaldi antenna is presented in Figure 2-9.

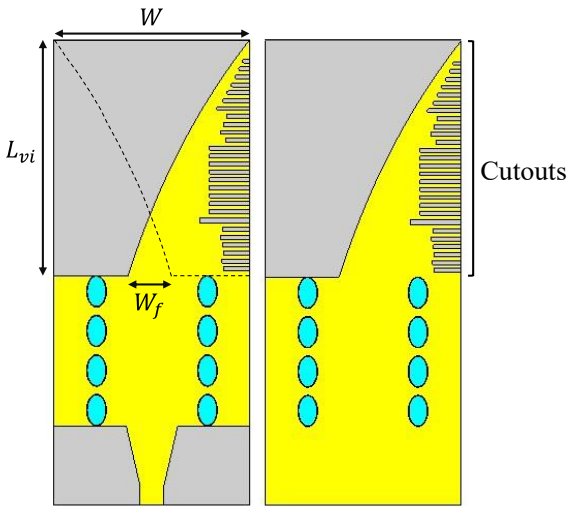

Figure 2-9. Proposed Vivaldi antenna structure, top view (left) and bottom view (right)

The top and bottom radiating metal element of the Vivaldi antenna exhibit an exponential taper profile, which is designed based on the equations (2.7) [66]. The parameter values for the Vivaldi antenna are presented in Table 4.

$$\begin{aligned} y &= Ae^{rx} + B \\ A &= \frac{W + W_f}{2}.(e^{r.L_{vi}} - 1)^{-1} \\ B &= -\frac{W + W_f e^{r.L_{vi}}}{2}.(e^{r.L_{vi}} - 1)^{-1} \end{aligned} \tag{2.7}$$

r is the taper rate and other antenna parameters are indicated in Figure 2-9.

Table 4. Dimensions of Vivaldi structure

Parameters	W_f	L_{vi}	W	r
Values (mm)	2.4	11.93	10	0.0075

Cutouts have been added to the radiating elements of the antenna to improve impedance matching at some specific frequencies [79]. Equation (2.8) presenting the formula for calculating the slot length l_s can be found in [79]. The simulated reflection coefficient of the proposed antenna with and without cutouts is presented in Figure 2-10.

$$l_s = \frac{\lambda}{4}.\sqrt{\frac{1 + \varepsilon_r}{2}} \tag{2.8}$$

l_s is the length of each cutout, λ is the resonant wavelength of each cutout and ε_r is the dielectric constant of the substrate.

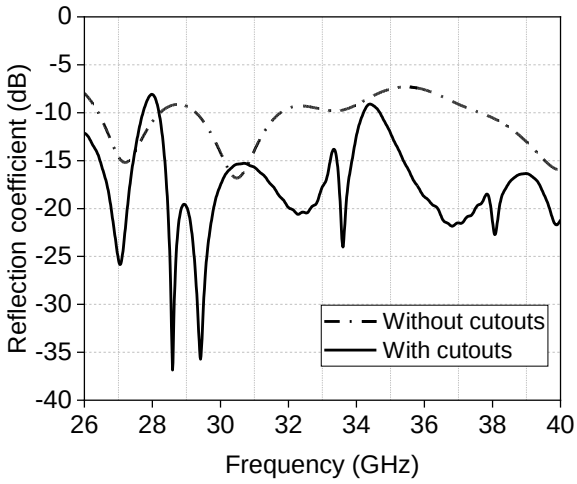

Figure 2-10. Simulated reflection coefficient of Vivaldi antenna with and without cutouts

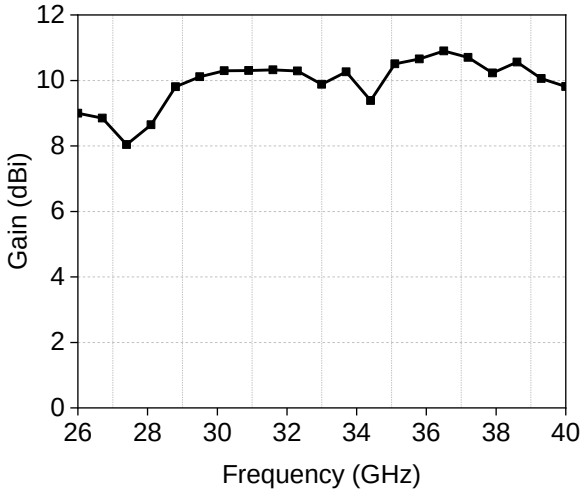

Figure 2-11. Simulated gain of the original Vivaldi antenna, with cutouts

It can be seen that the proposed Vivaldi antenna can operate throughout the Ka-band. However, the gain of this antenna is not really high, from 8 dBi to 10.5 dBi as shown in Figure 2-11. Therefore, two proposed methods which are studied with the aim of improving the gain of the Vivaldi antenna will be presented in sections 2.3 and 2.4 of this chapter.

2.3. Method 1: Substrate Lens and Quasi - Substrate Integrated Waveguide (Quasi-SIW) Structure

2.3.1. Quasi-SIW Structure

The idea of the quasi-SIW in this method comes from the principle of the E-plane rectangular horn antenna structure as shown in Figure 2-12. The horn flares act as transitions from waveguide mode to free-space mode. This transformation helps to reduce the reflected waves

and emphasize the transmitted waves. This traveling wave behavior, as can be seen in other antennas, results in low voltage standing wave ratio (VSWR) and wide bandwidth [80]. Therefore, the idea of using a flared metal waveguide shaped behind the radiant elements of the Vivaldi antenna was proposed.

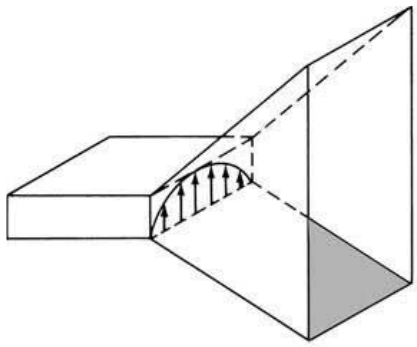

Figure 2-12. E-plane rectangular horn antenna [81]

However, this structure is non-planar. Therefore, a flared SIW-based structure, as shown in Figure 2-13, was used to integrate the non-planar structure into the designed antenna. However, in the proposed structure, the two flared metallic rows are not connected by the metallic layers on the top and bottom of the substrate, this is why the structure is called quasi-SIW rather than SIW. In the E-plane horn antenna, the horn is developed from the RWG structure, in other words, the E-plane horn structure is fed by the RWG. In a RWG structure, the wave is transmitted in TE mode or TM mode. However, in the antenna structure in this section, the quasi-SIW is fed by the radiating elements of the Vivaldi antenna. In other words, the quasi-horn is no longer powered by TE (or TM) mode. Using two metallic layers on the top and bottom of the substrate will cause an abrupt transition when changing from TEM mode to TE mode and will cause reflections, reducing antenna gain. Therefore, in this structure, only two flared metallic rows are used to increase the wave concentration in the radiation direction in order to increase the antenna gain in the radiation direction.

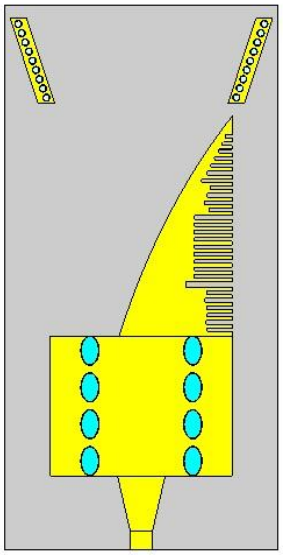

Figure 2-13. The original antenna with quasi-SIW structure

2.3.2. Substrate Lens

To further increase antenna gain, a substrate lens after the quasi-SIW structure is added. The substrate lens is an extension of the antenna substrate, allowing the antenna to maintain its planar structure. The substrate lens has a dielectric constant of 3.55 which is much bigger than that of air (dielectric constant of 1). Therefore, a large number of waves will be reflected inside the lens according to Snell's law. So, instead of being scattered into space, the wave will be focused and oriented along the substrate lens, which increases the gain.

When designing the substrate lens, two issues must be considered:

- *First issue – the length of the lens*

Figure 2-14 shows the antenna gain enhancement (deltaGain) after adding the lens (compared to without the lens) over the change in length L of a rectangular lens at 33 GHz - the center frequency of the K_a-band. It can be shown that the rate of the gain improvement grows up with the increase of L value. But after L exceeds the value of 30 mm, the gain improvement decreases. It can be said that, if we want to increase the antenna gain, we just need to increase the lens length as long as the length does not exceed the limit of 30 mm. However, the longer the lens, the bulkier the antenna. In order to increase the gain while keeping the compact size of the antenna, we choose the antenna length of 4 mm.

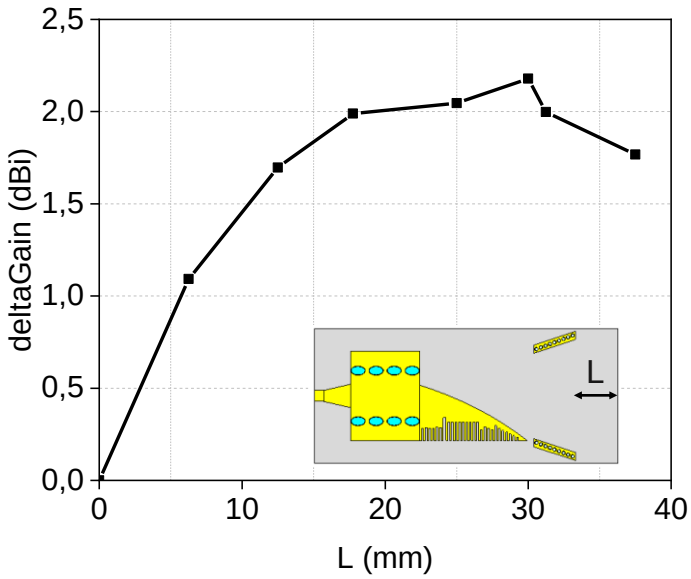

Figure 2-14. Simulated gain improvement versus length of lens at 33 GHz

- *Second issue – the shape of the lens*

Two different forms of lens are considered: rectangular and elliptical. The simulation shows that, with the same length, the rectangular lens gives a gain of 0.1-0.2 dB higher than the elliptical lens. To explain this slight increase, the electrical field phase of the antenna is presented in Figure 2-15(a). It can be seen that the E-field phase after passing through the rectangular lens is slightly more stable than passing through the elliptical lens, in other words, the phase error of the E-field after passing through the rectangular lens is smaller than that of the ellipse. As mentioned in [82], the E-field distribution of the radiator aperture and radiation pattern has a Fourier transform relationship. Thus, to reach a high directivity, it is necessary to have an in-phase aperture E-field. Therefore, the rectangular lens, which provides a more in-phase E-field, will give a better gain than the elliptical lens. However, the difference in phase in both cases is not too significant, particularly in contexts where the substrate thickness is much smaller than the wavelength, leading to the change in gain is not too obvious. Besides, the disadvantage of the rectangle lens is that it increases slightly the side lobe level as shown in Figure 2-15(b). Furthermore, the elliptical lens increases gain more consistently throughout the entire frequency range, while the rectangular lens focuses on increasing gain at high frequencies. Therefore, the elliptical lens is selected for the final design.

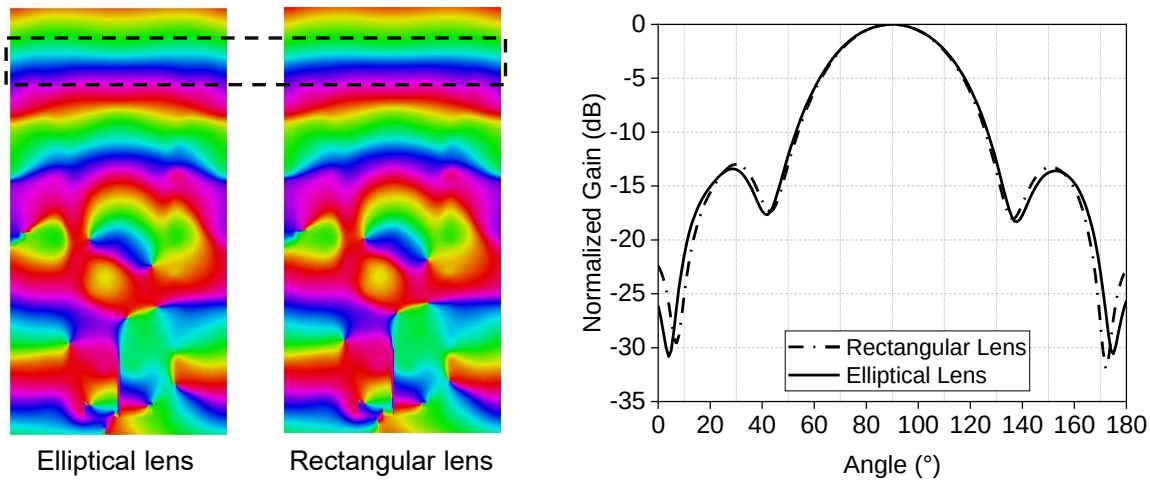

(a) (b)

Figure 2-15. (a) Simulated E-field phase (b) Simulated normalized gain of the antenna with elliptical and rectangular lens at 33 GHz

The entire antenna structure is presented in Figure 2-16. The antenna dimensions are given in Table 5.

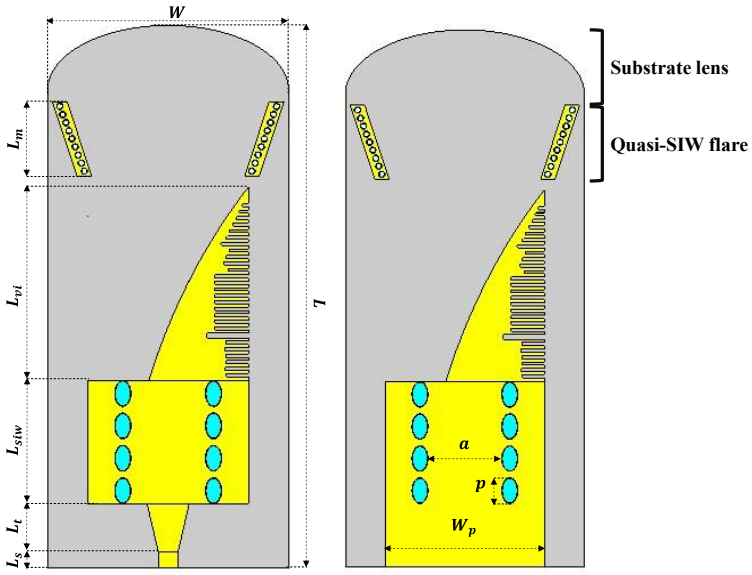

Figure 2-16. Full structure of antenna in the method 1

Table 5. Dimensions of antenna in the method 1

Parameters	W	L	W_p	L_s	L_t	L_{siw}	L_{vi}	L_m	a	p
Values (mm)	14.9	33.5	9.9	1	2.99	7.6	11.9	4.6	4.6	1.6

2.4. Method 2: Phase Compensation Lens (PCL)

This method aims to reduce the phase error (the difference in phase between the center point and the edges) of the E-field on the radiation plane to increase antenna gain [82]. Ideally, when a source is excited, the radiation waves in space have a spherical waveform. The E-field distribution of the radiator aperture and radiation pattern has a Fourier transform relationship [82]. Therefore, PCL method was proposed with the main idea of using lens to convert the cylindrical phase of incoming wavefront to quasi-in-phase for outgoing wavefront. Several special lenses are presented in Figure 2-17. Most of these lenses are based on generating different phase velocities (in average) at different locations to correct the phase of the wave as it passes through.

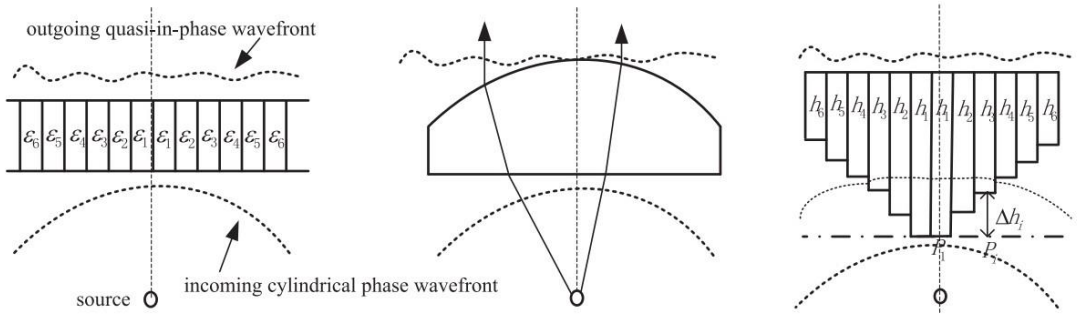

(a) (b) (c)

Figure 2-17. (a) Multi-dielectric lens (b) Hyperbolic lens (c) Planar quasi-hyperbolic structure [82]

However, these lens structures are often not flat, making it difficult to integrate into microstrip antennas. Therefore, flat PCL structures, constructed by using microstrip unit cells to correct phase error, were introduced [72], [82]. However, in these papers, the PCL configurations are built mainly on experiments of unit cell arrangement without reference method or process to base on. In addition, some comparisons to evaluate the gain improvement effect when adding PCL is done compared to the original antenna, before expanding the substrate. To add PCL metallic unit cell patterns, it is necessary to add a part of the substrate, or to expand the substrate in other words. As discussed in the previous section, the use of substrate lenses can increase the antenna gain. Therefore, in this section, we focus on leveraging simulation software to propose a process that can be used as reference when building PCL. The gain enhancement effect by PCL unit cells without considering the effect of substrate addition will be also discussed to assess the effectiveness of PCL method.

The PCL was designed at 33 GHz – center frequency of the Ka-band (26-40 GHz) according to the following steps:

- *Step 1: Examine the electrical phase of the antenna. Mesh the antenna and plot the phase matrix - which consists of the phases at selected points in the grid.*

The size of the original antenna (Figure 2-9) is 9.9 mm x 23.5 mm. To facilitate the meshing, the matrixing process and lens construction, we extended the antenna size to 10 mm x 25 mm. The extended antenna is simulated in the CST Studio software. The Ex-field phase in the xy-plane at 33 GHz is presented in Figure 2-21(a). Next, the antenna is divided into a grid with a mesh size of 1 mm x 1 mm. The phase value of each grid node is taken. We obtain a matrix where the value of each element of matrix is the phase value of the corresponding grid node (Figure 2-21 (b)). In simple terms, we have just digitized the Ex-field phase in the xy-plane.

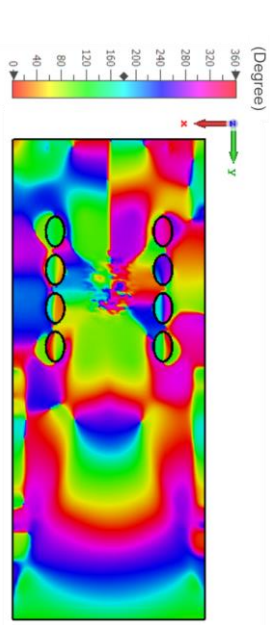

(Degree)

	1	2	3	4	5	6	7	8	9	10
1	-14.71	-21.78	-95.05	-168.5	-176.9	1.78	8.974	78.36	130.8	96.8
2	-9.292	-5.32	46.87	89.45	100.5	-74.9	-85.92	-128.7	164.7	130.9
3	-8.151	7.353	30	47.03	56.88	-121.2	-132.7	-150.4	-175.4	158.7
4	-14.98	6.078	8.701	-4.685	6.788	177.2	168.2	-174.5	-173.5	174.6
5	-30	-10.99	-12.71	-34.95	-26.01	138.8	137.3	163.7	172.1	175.5
6	-36.29	-30.84	-32.79	-32.84	-29.11	132.4	140.5	144.7	154.5	176
7	-29.93	-46.71	-46.19	-41.11	-34.68	116.9	132	132.5	139.8	174.2
8	-32.2	-60.37	-63.46	-53.31	-40.53	73.63	111.8	112.5	130.5	161.5
9	-57.8	-72.45	-71.85	-56.96	-31.21	48.26	90.48	100	123.6	159
10	-79.46	-72.76	-66.87	-20.1	13.31	39.3	66.09	77.19	120.6	170.4
11	-72.83	-48.9	11.23	42.07	45.15	37.61	32.25	45	53.63	-105.7
12	-46.43	-17.63	38.45	61.67	58.87	36.59	-13.7	-40.15	-12.7	-18.12
13	-19.09	-16.1	25.86	65.8	57.8	16.45	-61.88	-83.7	-13.2	25.64
14	8.03	-15.7	8.815	33.23	14.71	-52.91	-95.09	-111.3	21.3	48.19
15	33.98	-2.077	-12.76	-52.72	-71.88	-96.94	-119.5	-141.8	119.1	74.22
16	27.2	12.04	14	-119.3	-115.5	-126	-150.3	170.4	105.6	111
17	-1.441	11.78	59.28	158.1	-166.4	-168.4	160.5	118.8	80	88.53
18	-9.806	3.77	55.54	102.2	128.7	132.8	114.7	87.7	59.25	64.58
19	-24.09	-9.973	40.18	72.02	87.44	91.55	83.57	61.95	34.48	38.29
20	-45.78	-31.4	13.22	42.82	56.02	58.29	49.32	24.74	-5.158	-17.24
21	-59.22	-62.81	-31.82	0.3713	16.1	14.96	-2.634	-30.02	-48.05	-48.76
22	-89.58	-99.16	-79.45	-57.63	-43.6	-44.45	-56.34	-70.38	-82.31	69.65
23	-146.8	-131.6	-115.6	-103.7	-95.97	-93.87	-96.9	-103.5	-115.8	-143.5
24	177.4	-172.6	-154.2	-142.1	-135.5	-133.9	-137.6	-148.1	-169.7	-176.8
25	143.3	148.6	163.3	176.8	-175.7	-175.6	177.4	165.2	152.8	154.1
26	107.2	112.7	120.7	129.4	135.2	135.2	130.5	124.4	119.6	117.8

(a) (b)

Figure 2-18. PCL design – Step 1 (a) Ex-field phase in xy-plane at 33 GHz, before adding the PCL (b) Ex-field phase matrix

- *Step 2: Create the phase correction target*

An ideal antenna in this method is an antenna with zero phase differences at the aperture face, or in our case - at the bottom row of the matrix from *Step 1* - row 26 in Figure 2-21(b). It means that each matrix element in row 26 should be the same value. The task of the PCL unit cells is to make equal values of all matrix elements in row 26. To determine the phase correction target,

a matrix element in row 26 is first selected as the reference value (element *Ref*). For example, in our case, the element (26,1) is chosen as the reference value. Then, we subtract the *Ref* value in turn from others matrix elements of this bottom row as shown in Figure 2-19. The difference got at each position is the phase deviation that the unit cell must provide at that position to achieve a quasi-in-phase at the antenna aperture.

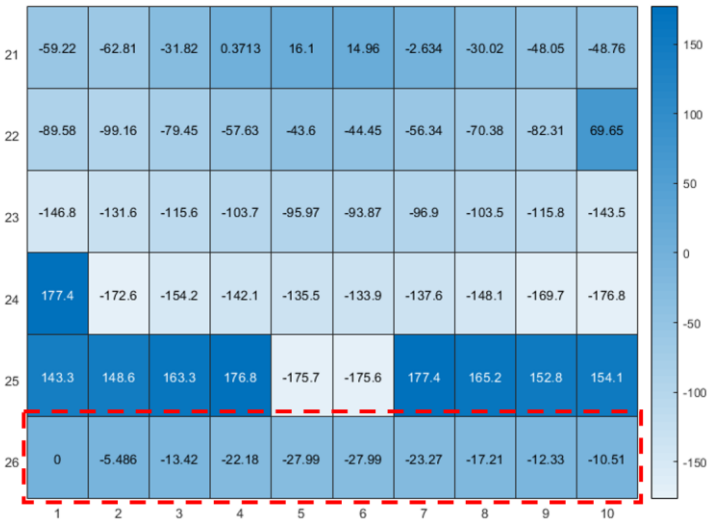

Figure 2-19. PCL design – Step 2: Row 26 – phase correction target

- *Step 3*: *Design and select a unit cell pattern. Investigate the phase deviation that the unit cell can produce with different sizes.*

In our concept, a simple unit cell - square unit cell is used. The use of this unit cell gives us a better vision of the constructability and the effect of PCL on the antenna, even when using simple unit cells. The phase deviation induced by changing the unit cell size at 33 GHz is studied and presented in Figure 2-20 with W_s = 1.

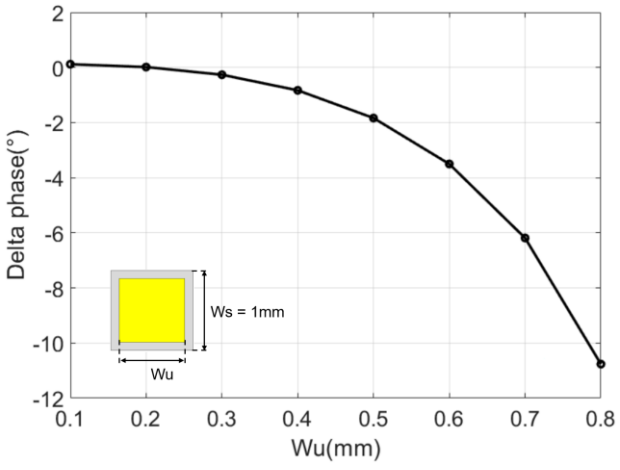

Figure 2-20. PCL design – Step 3: Unit cell phase deviation versus W_u at 33 GHz

- *<u>Step 4</u>: Build the PCL (matrix of unit cells) based on the calculated phase correction target (step 2) and selected unit cell (step 3).*

Based on the phase correction target and the chosen unit cell pattern, a PCL is designed as shown in Figure 2-21(a). The phase of Ex-field of the added lens antenna in xy-plane at 33 GHz is presented in Figure 2-21(b).

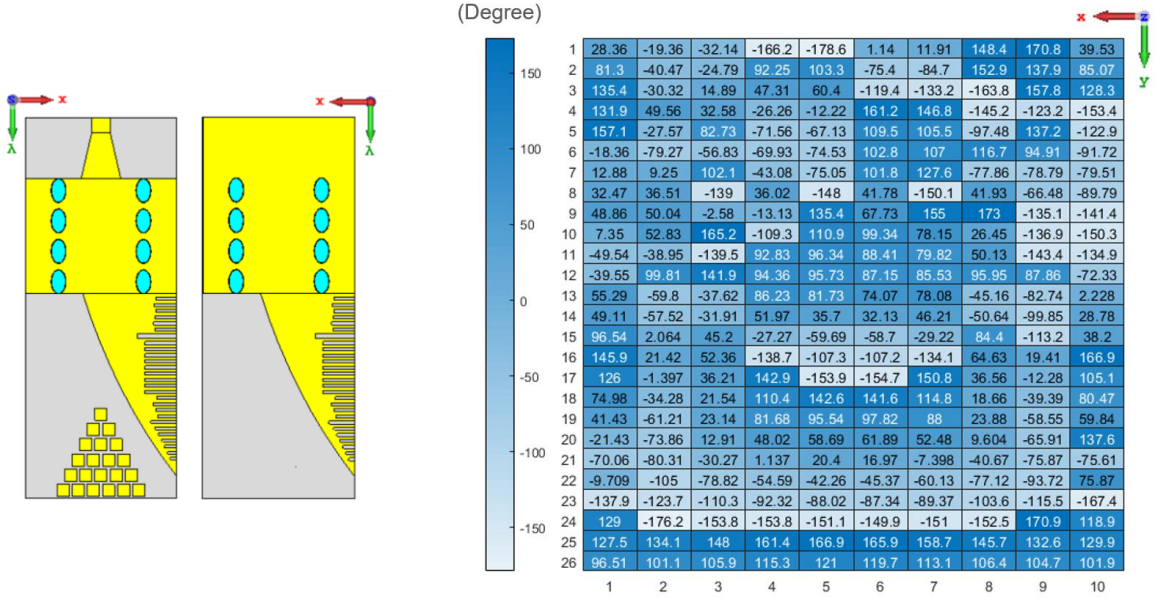

	1	2	3	4	5	6	7	8	9	10
1	28.36	-19.36	-32.14	-166.2	-178.6	1.14	11.91	148.4	170.8	39.53
2	81.3	-40.47	-24.79	92.25	103.3	-75.4	-84.7	152.9	137.9	85.07
3	135.4	-30.32	14.89	47.31	60.4	-119.4	-133.2	-163.8	157.8	128.3
4	131.9	49.56	32.58	-26.26	-12.22	161.2	146.8	-145.2	-123.2	-153.4
5	157.1	-27.57	82.73	-71.56	-67.13	109.5	105.5	-97.48	137.2	-122.9
6	-18.36	-79.27	-56.83	-69.93	-74.53	102.8	107	116.7	94.91	-91.72
7	12.88	9.25	102.1	-43.08	-75.05	101.8	127.6	-77.86	-78.79	-79.51
8	32.47	36.51	-139	36.02	-148	41.78	-150.1	41.93	-66.48	-89.79
9	48.86	50.04	-2.58	-13.13	135.4	67.73	155	173	-135.1	-141.4
10	7.35	52.83	165.2	-109.3	110.9	99.34	78.15	26.45	-136.9	-150.3
11	-49.54	-38.95	-139.5	92.83	96.34	88.41	79.82	50.13	-143.4	-134.9
12	-39.55	99.81	141.9	94.36	95.73	87.15	85.53	95.95	87.86	-72.33
13	55.29	-59.8	-37.62	86.23	81.73	74.07	78.08	-45.16	-82.74	2.228
14	49.11	-57.52	-31.91	51.97	35.7	32.13	46.21	-50.64	-99.85	28.78
15	96.54	2.064	45.2	-27.27	-59.69	-58.7	-29.22	84.4	-113.2	38.2
16	145.9	21.42	52.36	-138.7	-107.3	-107.2	-134.1	64.63	19.41	166.9
17	126	-1.397	36.21	142.9	-153.9	-154.7	150.8	36.56	-12.28	105.1
18	74.98	-34.28	21.54	110.4	142.6	141.6	114.8	18.66	-39.39	80.47
19	41.43	-61.21	23.14	81.68	95.54	97.82	88	23.88	-58.55	59.84
20	-21.43	-73.86	12.91	48.02	58.69	61.89	52.48	9.604	-65.91	137.6
21	-70.06	-80.31	-30.27	1.137	20.4	16.97	-7.398	-40.67	-75.87	-75.61
22	-9.709	-105	-78.82	-54.59	-42.26	-45.37	-60.13	-77.12	-93.72	75.87
23	-137.9	-123.7	-110.3	-92.32	-88.02	-87.34	-89.37	-103.6	-115.5	-167.4
24	129	-176.2	-153.8	-153.8	-151.1	-149.9	-151	-152.5	170.9	118.9
25	127.5	134.1	148	161.4	166.9	165.9	158.7	145.7	132.6	129.9
26	96.51	101.1	105.9	115.3	121	119.7	113.1	106.4	104.7	101.9

(a) (b)

Figure 2-21. PCL design – Step 4 (a) The completed antenna (b) Phase of Ex-field in xy-plane at 33 GHz, after adding the PCL.

2.5. Experimental Results and Comparison between the Two Methods

2.5.1. Experimental Results

Three antenna versions were fabricated:

- Ant 0 (Figure 2-22(a)): The extended version of the original antenna used in the method 2, with the size of 10 mm x 25 mm. This version was selected to fabricate rather than the original version with the size of 9.9 mm x 23.5 mm because the difference between this version and the original antenna is quite small, especially compared to the final antenna in method 1. In addition, the use of this version make allows valuating the effect of PCL unit cells on the antenna without considering the effect of substrate extension.
- Ant 1 (Figure 2-22 (b)): The final antenna in the method 1
- Ant 2 (Figure 2-22 (c)): The final antenna in the method 2

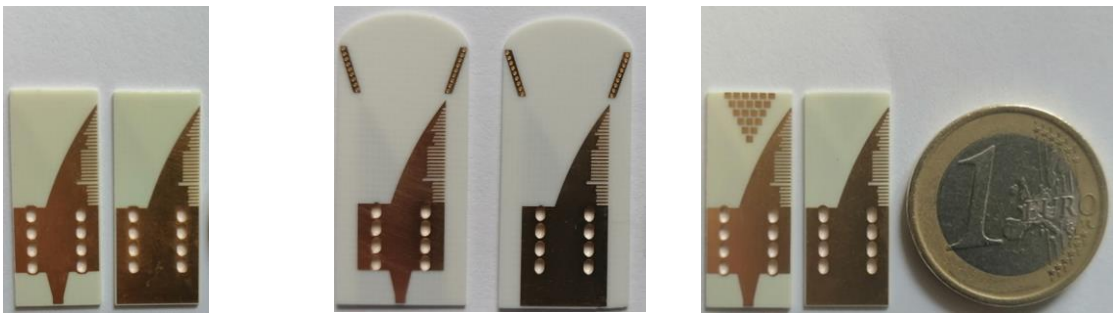

(a) (b) (c)

Figure 2-22. Fabricated antennas (a) Ant 0 (b) Ant 1 (c) Ant 2

The measured reflection coefficients of three fabricated antennas are presented in Figure 2-23. It can be seen that all three antennas have good impedance matching in the whole Ka-band. Figure 2-24 shows the measured gain of three antennas in the Ka-band. It can be shown that, method 1 helps to improve the gain of the original antenna up to 8 dB in peak. In method 2, by simply adding the PCL metallic unit cells without changing the antenna size, an average gain improvement of 1 dB is achieved. The three antennas work well in the whole Ka-band with a radiation efficiency of about 70 - 90% over the frequency band.

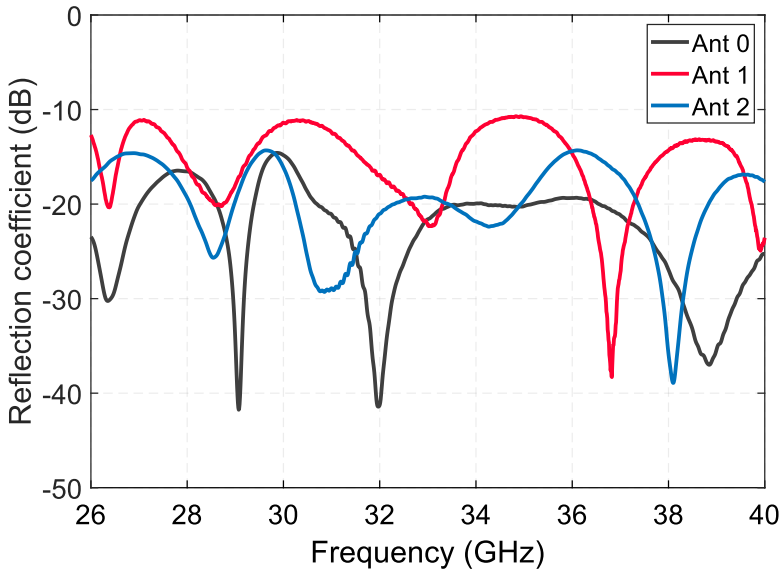

Figure 2-23. Measured reflection coefficient S_{11} of three fabricated antennas

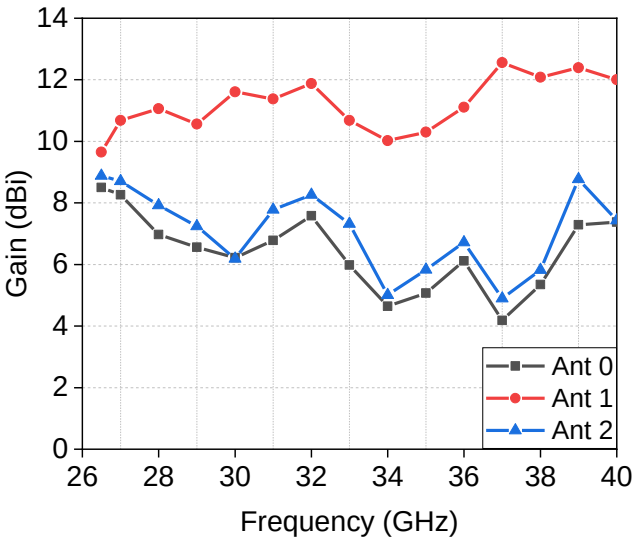

Figure 2-24. Measured gain versus frequency of three fabricated antennas

The measured radiation patterns in E-plane and H-plane at 33 GHz of three fabricated antennas are presented in the Figure 2-25 and Figure 2-26 respectively. The measurements show that all three antennas have a good directional radiation property. The reason for the fact that the main beam in the H-plane is slightly deviated from 0° could be due to the structural dissimilarity between the top surface containing the microstrip line and the lower surface containing the ground of the antennas.

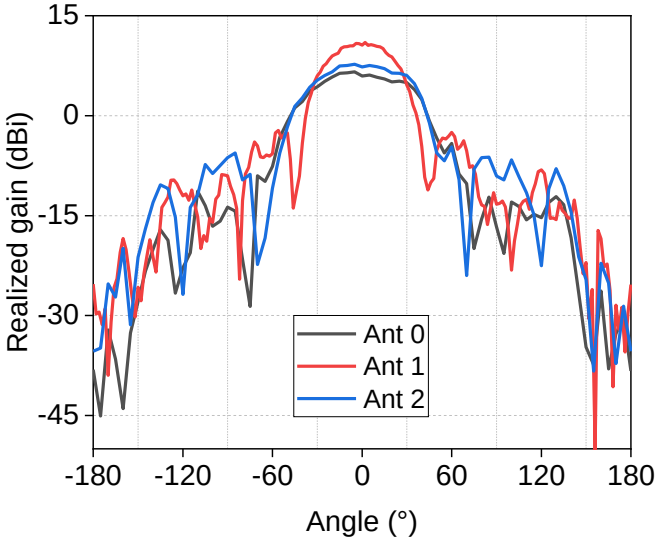

Figure 2-25. Measured radiation pattern co-polarization in E-plane at 33 GHz of three fabricated antennas

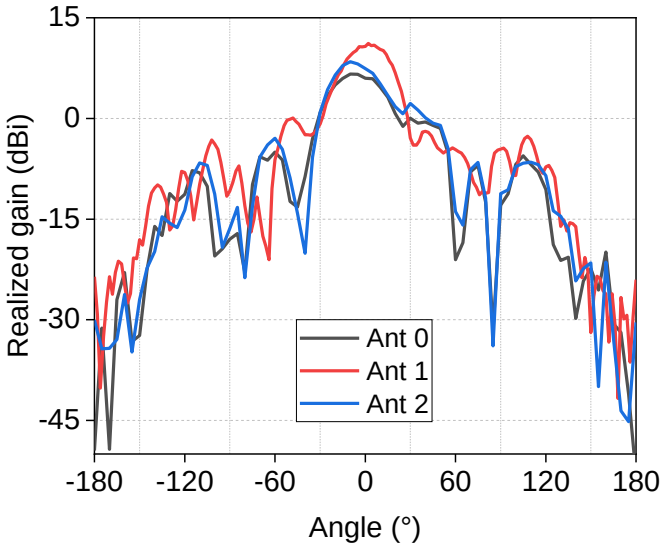

Figure 2-26. Measured radiation pattern co-polarization in H-plane at 33 GHz of three fabricated antennas

2.5.2. Comparison between the Two Methods

From the measurement results, it can be seen that the second method provides a much better gain improvement than the second method. However, the first method also has some disadvantages compared to the second method. Some advantages and disadvantages of each method are listed in the Table 6.

Table 6. Comparison between the two methods

	Method 1	Method 2
Advantage	1. *An effective gain improvement* This method gives a gain enhancement of 4 dB in average and 8 dB in peak.	1. *Slightly increased in antenna size* If compared to the extended antenna, the PCL lens in the method 2 improves the gain by about 1 dB without changing the antenna size. If compared to the original antenna before being extended, with an increase of about 6% in volume, the antenna gain is increased by about 1.5 dB. 2. *Uncomplicated structure*

		The unit cells that make up the PCL have an uncomplicated structure that does not increase the difficulty of antenna fabrication, unlike the metal via holes in SIW.
Disadvantage	1. *A noticeable antenna's size increase* The volume of the antenna has been increased by 42%. 2. *Quasi-SIW structure increases fabrication complexity* The use of quasi-SIW structures with relatively small metal via holes increases the complexity of fabrication. In our antenna, the SIW structure has been used in the transmission, so the quasi-SIW structure can be considered as not changing the difficulty of this antenna fabrication. However, in other antennas, if SIW has not been used before, the quasi-SIW structure, which is used to increase the gain of the antenna, will maybe increase the difficulty and also the cost in antenna fabrication.	1. *Not excellent in gain improvement* This method brings a gain enhancement of about 1 dB compared to the extended antenna, or 1.5 dB compared to the original antenna, which is not excellent compared to the method 1.

2.6. Conclusion of the Chapter

An overview of several commonly used methods for improving antenna gain was presented. Then, on the basis of these theories, two methods are proposed: quasi-SIW combining with dielectric lens and PCL. Each approach has its own strengths and weaknesses.

The method 1 leverages the dielectric substrate and flared quasi-SIW structure to focus and direct the wave in the direction of radiation, thereby improving the antenna gain. However, this method also requires an increase in antenna size and an increase in manufacturing difficulty caused by the use of metallic holes. The comparison of the antenna in the method 1 with other related works is presented in Table 7. In [83], a metamaterial lens is designed to increase the antenna gain. With a 15.8% increase in antenna volume, the method provides a 5 dBi enhancement gain peak. [40] presents a Vivaldi antenna in Ka-band using a dielectric load with printed metal transition to reach higher gain. With 144% increase in antenna volume, the method achieves a gain enhancement peak of approximately 6 dBi. In our method, the antenna volume is increased by 42 % compared to the original antenna, but the gain is improved up to 7.5 dBi. It can be seen that our proposed method gives a good gain improvement and a fairly stable gain in the whole frequency band but does not make the antenna too bulky compared to other related works.

Table 7. Comparison of Method 1 with related works

	[83]	[40]	Method 1
Frequency (GHz)	1-12	24-44	26-40
Dimension (mm)	180 x 240 (~3.9λ x 5.2λ)	14 x 33 (~1.59λ x 3.74λ)	13.95 x 33.52 (~1.53λ x 3.69λ)
Gain enhancement (dB)	0.5-5	4.5-6	1.5-7.5

The method 2 has the advantage of being simple, being able to enhance the antenna gain without increasing the antenna size. However, the improvement achieved in the presented example is not significant. Here are some reasons that can be used to explain this behavior:

- 1D structure: This PCL only adjusts the phase of the E-field on a single cross-section. In other words, it is only a 1D lens structure. Thus, its effect on phase correction is not significant, especially when compared to 3D lenses placed perpendicular to the radiation direction of the antenna. Furthermore, the substrate thickness is small, making the effect of PCL even more blurry.

- Not good unit cell: It can be observed that the transmission phase deviation provided by the unit cell is not significant. This limits the ability to correct the phase error, leading to many locations where phase error cannot be completely corrected as the target.
- Not perfect boundary conditions: In comparison with the simulation boundary conditions, there are some differences in the actual electromagnetic field conditions. The simulation of unit cells under ideal conditions is equivalent to the hypothesis that the unit cell plane will contain an infinite number of unit cells. However, in practice, the number of unit cells is not infinite. This changes the ability of unit cells to create phase deviation due to changes in the coupling between unit cells. Especially, with edge unit cells, there is less coupling between unit cells than unit cells at the center (surrounded by other unit cells). These edge unit cells provide the weakest phase correction.

One of the solutions to improve the efficiency of PCL is to select a good unit cell. Some suggestions for the design of unit cells are:

- Do not choose unit cells which are too large. A unit cell often provides different phase deviations at the center and the edge of the unit cell. Using too large unit cells may cause ripples in the E-field phase. However, unit cells that are too small can either make it difficult to fabricate or cannot make a big enough phase deviation.
- The unit cell should have a high transmission coefficient S_{21} (closer to 0 dB) and a low reflection coefficient S_{11}. This is to ensure that the wave can pass through the unit cell without too much loss due to reflection.

Chapter 3. 3D Antenna: Printed Radome

This chapter presents ideas on leveraging the radome to improve antenna functionality through the use of 3D printing technology to print different metallic and conductive structures on existing dome surfaces. By doing this way, the radome will help protect and improve the functions of the antenna. The antenna-radome systems in this chapter are designed at 3.6 GHz as a proof of concept.

3.1. Overview

Radomes are often used to protect antennas from environmental influences such as wind, snow, rain or to minimize the effects of other physical influences [84]. They are also used to hide the antenna from view, and thus prevent identifying the type of antennas or its polarization. In other words, the main function of a radome is to protect the antenna. This is relatively wasteful because radomes occupy a large area while providing only one effect. To limit this waste, more and more research is being done with the aim of utilizing radome to improve or control the antenna properties. Some studies are shown in Figure 3-1 ([85], [86]).

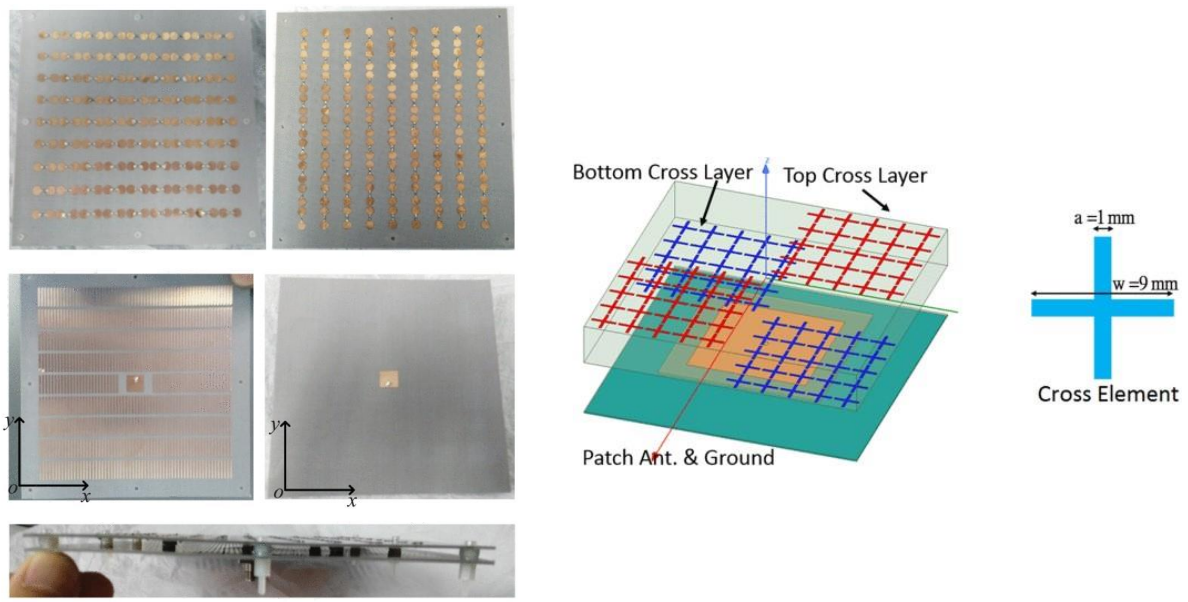

(a) (b)

Figure 3-1. (a) Antenna with absorbent frequency selective radome [85] (b) FSS-integrated low-RCS radome [86]

In [85], a pair of circular slot resonators is printed on the upper and lower surface of the absorbent frequency selective radome (AFSR) to create a transmitting effect in the vertical polarization and an absorbing effect in the horizontal polarization. An antenna co-designed with

this AFSR is realized to achieve a low radar cross section (RCS) and a low profile. Another frequency selective surface (FSS) which is compatible with existing radome structures to create an RCS suppression band is presented in [86]. Two FSS layers made of band-stop elements are applied on the top and bottom of the radome dielectric slab. By choosing a thickness of an odd multiple of a quarter wavelength, these two layers create a phase cancellation structure and suppress returns. Hence, the system can provide a broadband low RCS without perturbing radar antenna operations. However, these radomes are only 2D planar, whereas commonly used radomes often have 3D structures to protect the antenna system. These 2D structures have some disadvantages if they are used in practice.

Some 3D functionalized radomes which are realized by three different techniques including origami, printed mask and engraving [87]–[89] are presented in Figure 3-2. [87] presents a conical FSS radome constructed from coupled-resonator spatial filter (CSRF) unit cells. To create the conical radome, FSS unit cells are arranged to fit a fan-shaped planar form, which is the form of a cone when spread out in a plane. Then the fan-shaped planar FSS is rolled and adhered to form a conical FSS radome. In [88], the authors present a rapid electromagnetic prototype fabrication using a conformal mask to fabricate a conformal FSS radome. Firstly, a 3D conformal mask is designed to conformally cover a paraboloid surface. Then, the projection of FSS unit cells is removed from the mask. An electron beam evaporation tool was used to deposit copper on the paraboloid surface. Finally, the mask is removed and the copper remaining on the substrate surface is the FSS structure that needs to be printed. [89] proposes a 3D integrated free-standing thick-screen FSS radome with a good pass-band transmittance. The radome is fabricated using a laser robot processing system to create Y-shaped slots on a copper hemisphere. As a result, a thick-screen FSS radome of copper, which is sturdy but quite transparent to radiation waves, is fabricated. However, these three techniques present some disadvantages. The origami technique can only produce radomes with special shapes such as cones or cylinders. The fabrication of a radome with a sphere, for example, is beyond the scope of this method. Printed mask is more flexible in creating radomes with different structures. However, this method requires a printed mask, which needs to be determined by equations. This is complicated and especially in cases where the surface has no specific equation. The disadvantage of the last technique (engraving technique) is the need of using a copper base radome, which is uncommon in practice. In addition, the creation of Y-shaped slots makes the radome open and reduces the antenna protection ability.

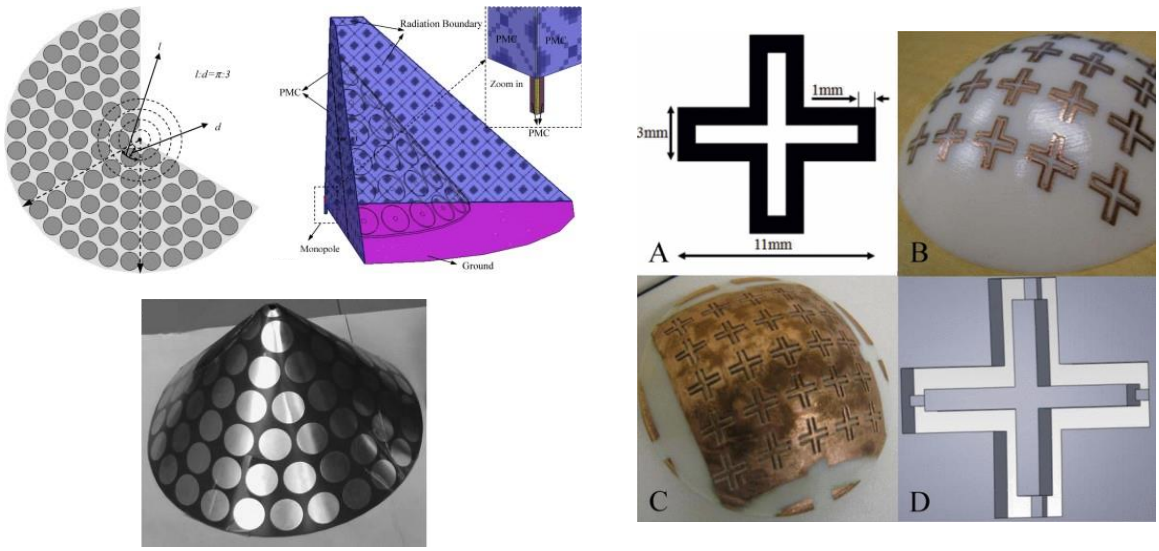

(a) (b)

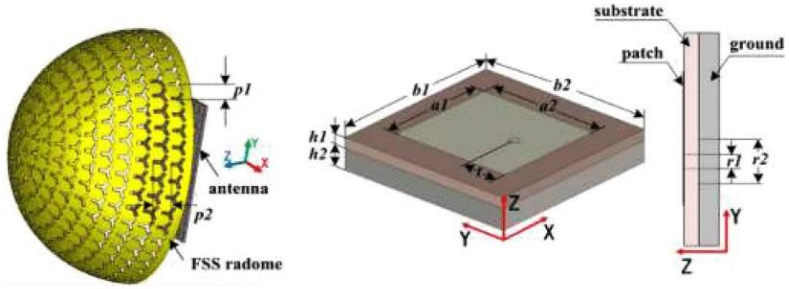

(c)

Figure 3-2. (a) Conical FSS radome [87] (b) Conformal FSS radome [88] (c) Integrated free-standing thick-screen FSS radome [89]

To overcome the disadvantages of the three methods mentioned above, 3D direct writing technology was introduced. This method allows the conductive ink to be placed directly onto a 3D object without contact. In our case, this technique is selected to print the conductive ink onto a plastic hemispherical dome surface. The main technologies in 3D direct writing are inkjet, micro dispensing, aerosol jet and jetting [90]. In this study, jetting piezoelectric technology is chosen for two reasons: one layer of ink on the surface is enough to obtain a required metal layer thickness and printing process is rapid, up to 60 mm/s [90]. To realize the printed radome using jetting piezoelectric technology:

- Firstly, the base material of radome, on which conductive patterns are printed, is studied.

- Secondly, the first demonstration pattern is printed on the radome. This simple pattern is printed to modify the radiation of an antenna and to give a rough estimate of the printing using jetting technology.

- Then, FSS radome is designed to be able to control the antenna radiation. Two different types of FSS patterns are designed and manufactured. An experiment to control the antenna reconfigurability electrically and the problems encountered in this experiment will be discussed.

All systems in this chapter are design to operate at the frequency center of 3.6 GHz. This frequency is selected for two reasons:

- 3.6 GHz is a frequency in the civilly deployed 5G band as described in Chapter 1.
- Designing and printing FSS patterns for Ka-band is difficult because printing small unit cells for this band could exceed the limit of printing technology.

3.2. Material and Method

The printed radome is constructed based on an acrylic hemisphere dome with a diameter of 100 mm, which is presented in Figure 3-3. To be able to simulate accurately in the software CST Studio Suite, dome electrical properties (especially complex permittivity) are measured and calculated using a probe station as shown in Figure 3-4 and the direct probe contact method [91]. The permittivity and loss tangent of the acrylic is presented in Figure 3-5. At 3.6 GHz, the dome has a permittivity (ε_r) of 5.1 and a loss tangent ($tan\delta$) of 0.14.

Figure 3-3. Acrylic hemisphere

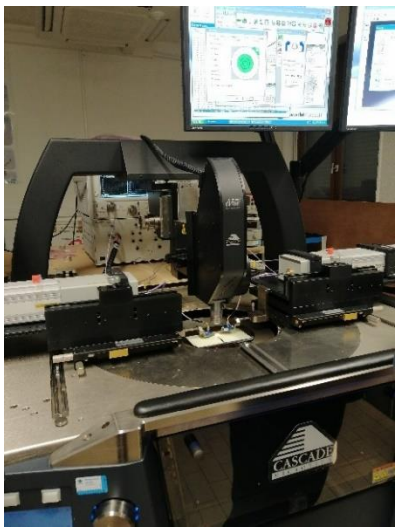

Figure 3-4. Probe station

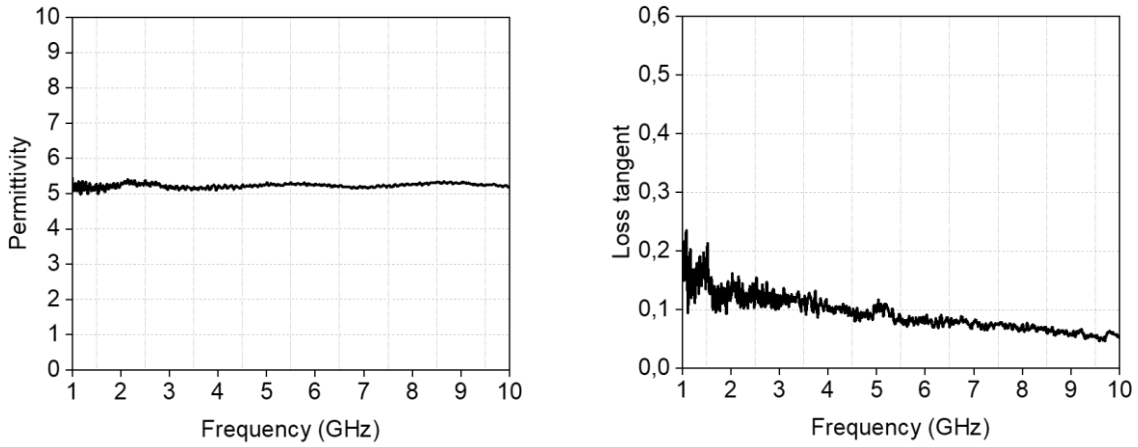

(a) (b)

Figure 3-5. Calculated electrical properties of plastic radome versus frequency (a) Dielectric constant (b) Loss tangent

The printing jet equipment is composed of Vermes MDS 3200A printhead set on a Staubli TX 60 6-axis robot as shown in Figure 3-6(a). The printhead has a dimension of 118.5 mm x 82 mm x 12 mm and a weight of 375 g [90]. This system allows printing on any shape object and especially on a hemisphere. Conductive jet ink is printed without contact between the printhead and the printed surface. The jetting process ejects ink drops at a high frequency (up to 3 kHz) thanks to a piezoelectric actuator that activates the piston [90] as can be seen in the block diagram in Figure 3-6(b). The ink is contained in the pressurized syringe (4 to 5 bars) to promote the flow of viscous ink. It flows through the fluid channel to the nozzle when the piston is raised. When the piston closes at high speed, the fluid contained at the nozzle

is ejected in the form of drop towards the support. The stroke of the piston can be adjusted up to 3 mm. Different nozzle diameters can be used, from 50 µm to 400 µm.

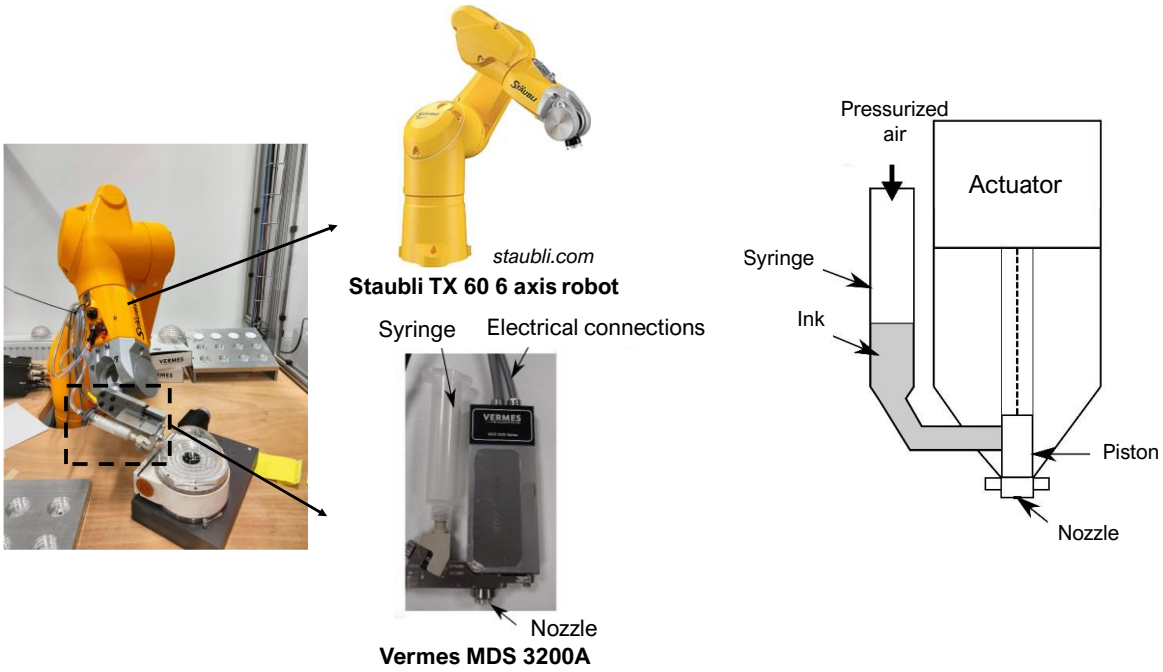

(a) (b)

Figure 3-6. (a) Vermes MDS 3200A set on a Staubli TX 60 6 axis robot (b) Block diagram of the jetting system [90]

3.3. Printed Ring Pattern to Modify Antenna Radiation

The aim of this section is to design a simple printed pattern which can be used to modify the radiation pattern of an antenna and also to validate the printing process on the radome.

3.3.1. Antenna Design

To evaluate the impact of the printed radome on the radiation pattern, an omnidirectional antenna is selected. An annular ring patch is selected because of its simplicity while having good omnidirectional properties. The antenna is designed to operate at 3.6 GHz using the RO4003C substrate (ε_r=3.55) with a thickness of 1.524 mm. The geometry of the antenna is shown in Figure 3-7. It is powered by a 50 Ω microstrip line.

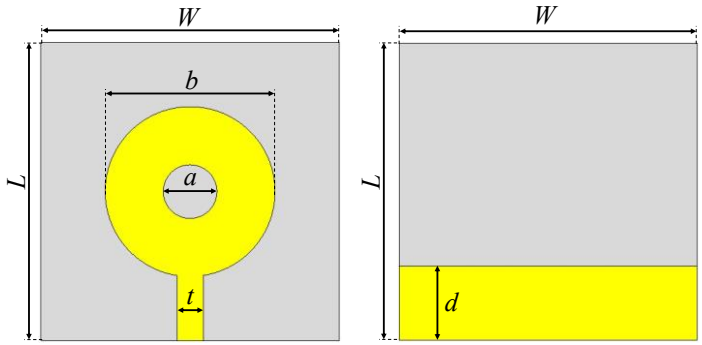

Figure 3-7. Geometry of the annular ring patch antenna

Table 8. Dimensions of designed annular ring patch antenna

Parameters	*W*	*L*	*a*	*b*	*t*	*d*
Values (mm)	40	40	4	7.4	3.5	10

The fabricated antenna is shown in Figure 3-8. Figure 3-9 presents the reflection coefficient S_{11} of the patch antenna in simulation and measurement. The measurement is carried out between 100 MHz and 10 GHz. It can be seen that the measurement result is close to the simulation result in CST Studio Solver. The slight difference could be explained by the influence of the environment and by the effect of the connector which is not perfectly corrected by the calibration of the VNA (Vector Network Analyzer). The antenna has an acceptable level of adaptation at the desired frequency (3.6 GHz).

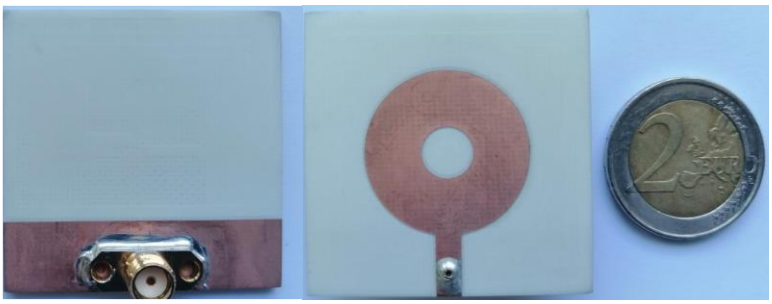

Figure 3-8. Fabricated annular ring patch antenna

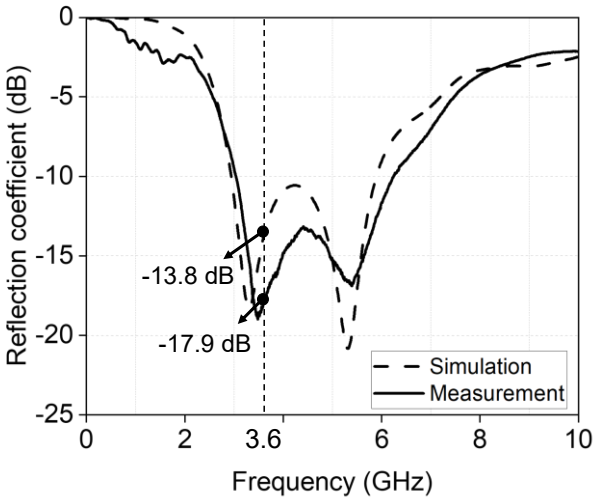

Figure 3-9. Simulated and measured reflection coefficient of the annular ring patch antenna

The simulated and measured radiation pattern of the antenna is presented in Figure 3-10. It can be seen that there is a similarity between measurement and simulation results. The slight difference may come from the environment. The annular ring patch antenna is designed with the ground not completely extended, so it is very sensitive to environmental factors.

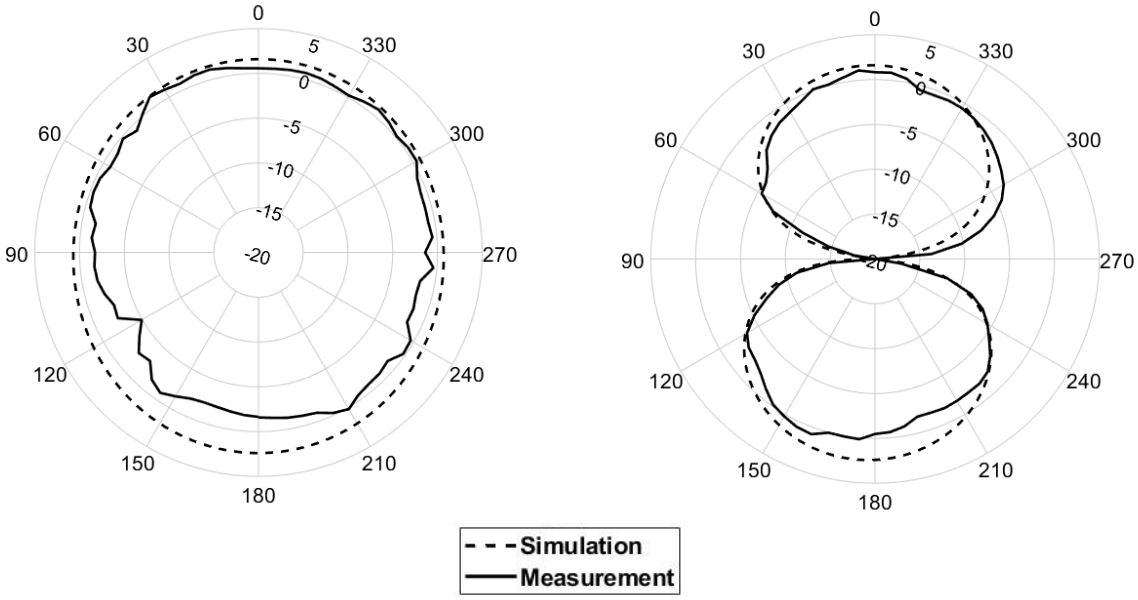

(a) (b)

Figure 3-10. Simulated and measured radiation pattern of the annular ring patch antenna in (a) H-plane (b) E-plane

3.3.2. Radome Pattern design

Figure 3-11 shows the structure of the simulated antenna-radome system. When adding the bare radome, without the printed pattern (Figure 3-11(a)), the maximum antenna gain is reduced slightly from 2.39 dBi to 2.36 dBi in simulation. The antenna radiation pattern is also slightly modified.

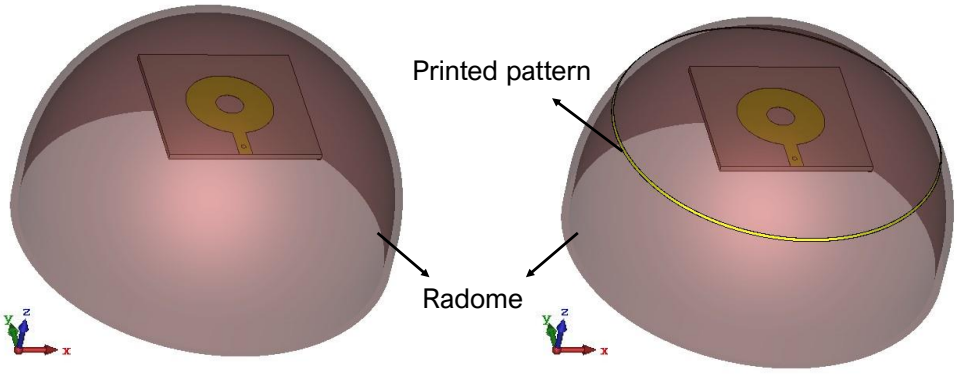

(a) (b)

Figure 3-11. Simulated antenna with its (a) Bare radome (b) Printed radome

The pattern, designed to print on the radome surface, is a conductive ring. This ring is located 36 mm from the base of the hemisphere and has a width of 0.7 mm. It acts as a reflector, which redirects the secondary beam towards the main beam, thus improving the antenna main beam. This idea comes from the principle of the reflector in a 2-element Yagi antenna. The printed radome is shown in Figure 3-12.

Figure 3-12. Printed ring pattern radome

The antenna-radome system was measured in the anechoic chamber. To hold and maintain the distance between the antenna and the radome, a styrofoam support (with a permittivity close to air) was fabricated and used as shown in Figure 3-13. Simulated and measured radiation

patterns of the antenna with and without the printed radome are presented in Figure 3-14. It can be seen that the printed radome helps to conform the antenna radiation and improve the gain in a specific direction by 2 dB. The measurement results are close to those obtained by simulation. The difference in the radiation patterns, especially at the back of the antenna (angle of 180°), must probably be caused by the support and cables present during the measurements on the experimental platform. Nevertheless, the effectiveness of the functionalization of the radome on the shaping of the radiation pattern is clearly highlighted. The similarity between measurement and simulation results demonstrates the reliability of the jetting piezoelectric technology.

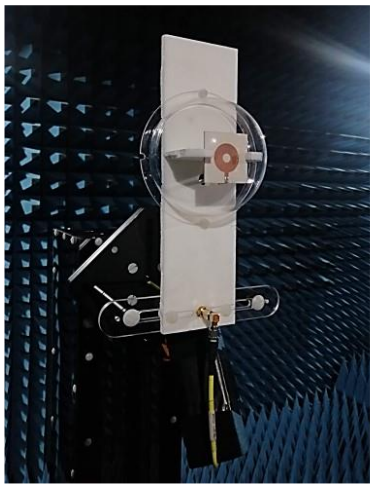

Figure 3-13. Measurement configuration in anechoic chamber using styrofoam support

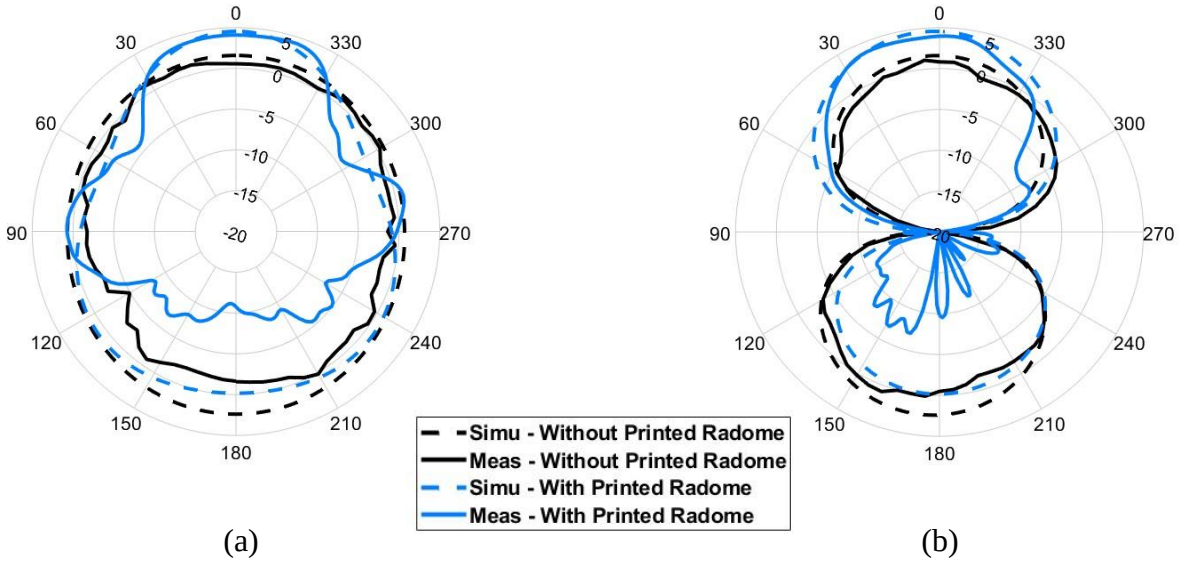

(a) (b)

Figure 3-14. Simulated (Simu.) and measured (Meas.) radiation pattern of antenna-radome system at 3.6 GHz in (a) H-plane (b) E-plane

3.4. Printed FSS-based Pattern to Reconfigure Antenna Radiation

3.4.1. Antenna Design

To have an easier evaluation of radome effect on the antenna, a simple rectangular patch antenna is chosen. This type of antenna is selected because it is simple, stable and can provide a wide angular width. The antenna is designed at the center frequency of 3.6 GHz on the RO4003C substrate (ε_r=3.55) with a thickness of 1.524 mm. The antenna is fed from the bottom through a SMA connector. The SMA connector position is calculated to achieve a good impedance matching. The complete antenna geometry is shown in Figure 3-15.

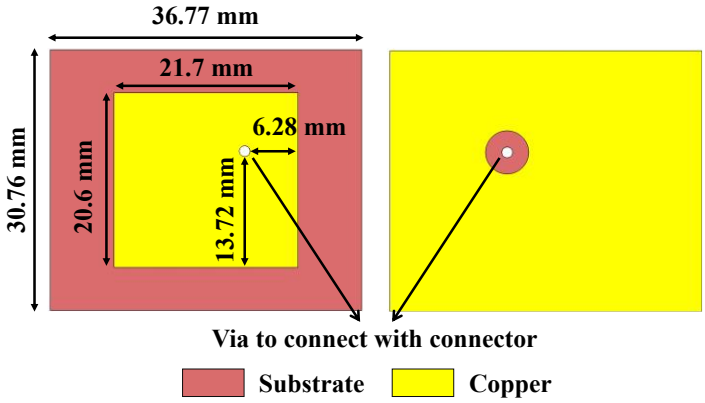

Figure 3-15. Geometry of rectangular patch antenna

The fabricated antenna is presented in Figure 3-16. Figure 3-17 presents a comparison of the patch antenna reflection coefficient in simulation and measurement. It can be seen that the fabrication antenna has a good impedance matching at 3.6 GHz.

Figure 3-16. Fabricated rectangular patch antenna

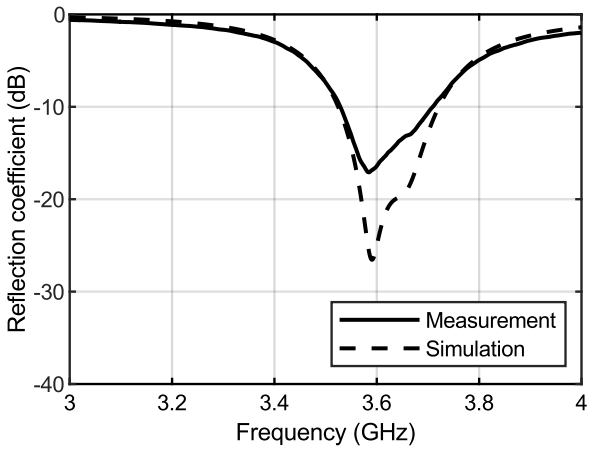

Figure 3-17. Reflection coefficient of the patch antenna

3.4.2. Basic Frequency Selective Surface Unit Cells

Frequency Selective Surface (FSS) is a structure consisting of periodic elements which exhibits frequency filtering properties similar to those of frequency filters in traditional radiofrequency (RF) circuits [92]. FSS can be divided into four basic types as traditional filter: low pass, high pass, band stop and band pass. These four basic FSS and their filter property responses are presented in Figure 3-18 [93].

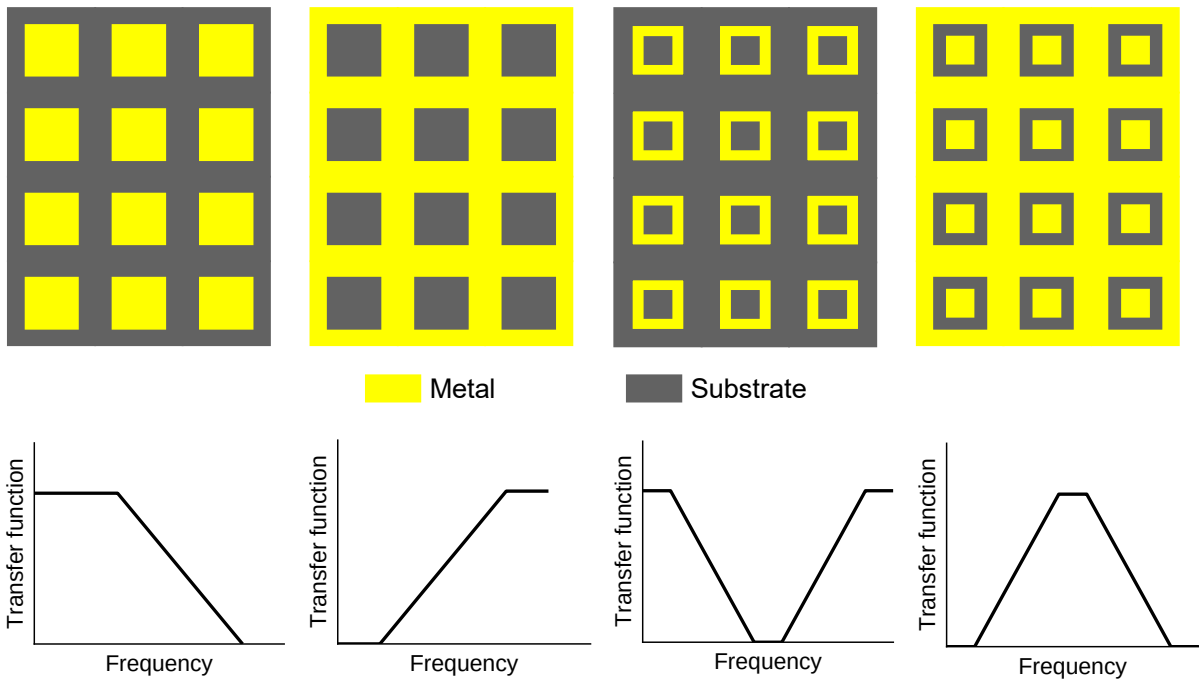

Figure 3-18. Four basic FSS filters (a) Low pass (b) High pass (c) Band stop (d) Band pass

Among the four basic types of unit cells, we can see that the use of diodes to connect unit cells in the high pass and the band pass is not easy. Between the low pass and the band stop, the low pass is simpler to design because the number of parameters to determine the unit cell in the low pass is less than in the band stop. So, the low pass unit cell is selected for the first design.

The general concept of the printed FSS pattern for the radome is that the pattern composes of two different unit cell types:

- A unit cell type that allows waves at 3.6 GHz to pass through (transmission unit cell)
- A unit cell type that reflects waves at 3.6 GHz (reflection unit cell), which is constructed based on the transmission unit cell.

Why must we use the transmission unit cells while without them, the waves can still travel through the radome? In fact, the printed FSS pattern is designed towards the perspective of using only one type of unit cell in combination with diodes to control the antenna radiation. Controlling the diode state (ON/OFF) allow controlling the transmission characteristics of the unit cells (transmission/reflection). The use of two unit cells with similar structures, but with opposite transmission characteristics is considered as an ideal equivalence for using unit cell with diodes. This simplifies the diode problem in the first design.

3.4.3. FSS Low Pass-based Printed Radome

3.4.3.a. Unit cell

To build a FSS pattern on the surface of the radome, it is necessary to choose a suitable unit cell. It is difficult to simulate, study and choose unit cells on 3D sphere surface. So, we first simulated unit cells on a planar substrate to choose a suitable form and dimension for the unit cell as a reference for the printed FSS pattern on radome. In CST Studio Suite, unit cells are simulated on the acrylic substrate with a thickness of 2 mm as the thickness of the acrylic hemisphere. This is the base material of radome and was characterized and in the section *3.2* (ε_r = 5.1 and $tan\delta$ = 0.14 at 3.6 GHz). As mentioned above, the FSS pattern includes two types of unit cell: (1) transmission unit cell (2) reflection unit cell. These two unit cells are designed under the following constraints:

- Both types of unit cells must have a similar structure. The second unit cell must be constructed by adding connection lines to the first unit cell. These lines will represent the state off of diode.

- The first unit cell needs to behave as a low pass filter structure, where 3.6 GHz is in the pass-band region (transmission coefficient S_{21} > -3 dB) while the second unit cell acts as a high pass filter, where 3.6 GHz is in the stop-band region.

The proposed candidates for the two unit cells are shown in Figure 3-19(a) (for the first unit cell) and Figure 3-19(b) (for the second unit cell). ($\vec{k}$ is the propagation vector)

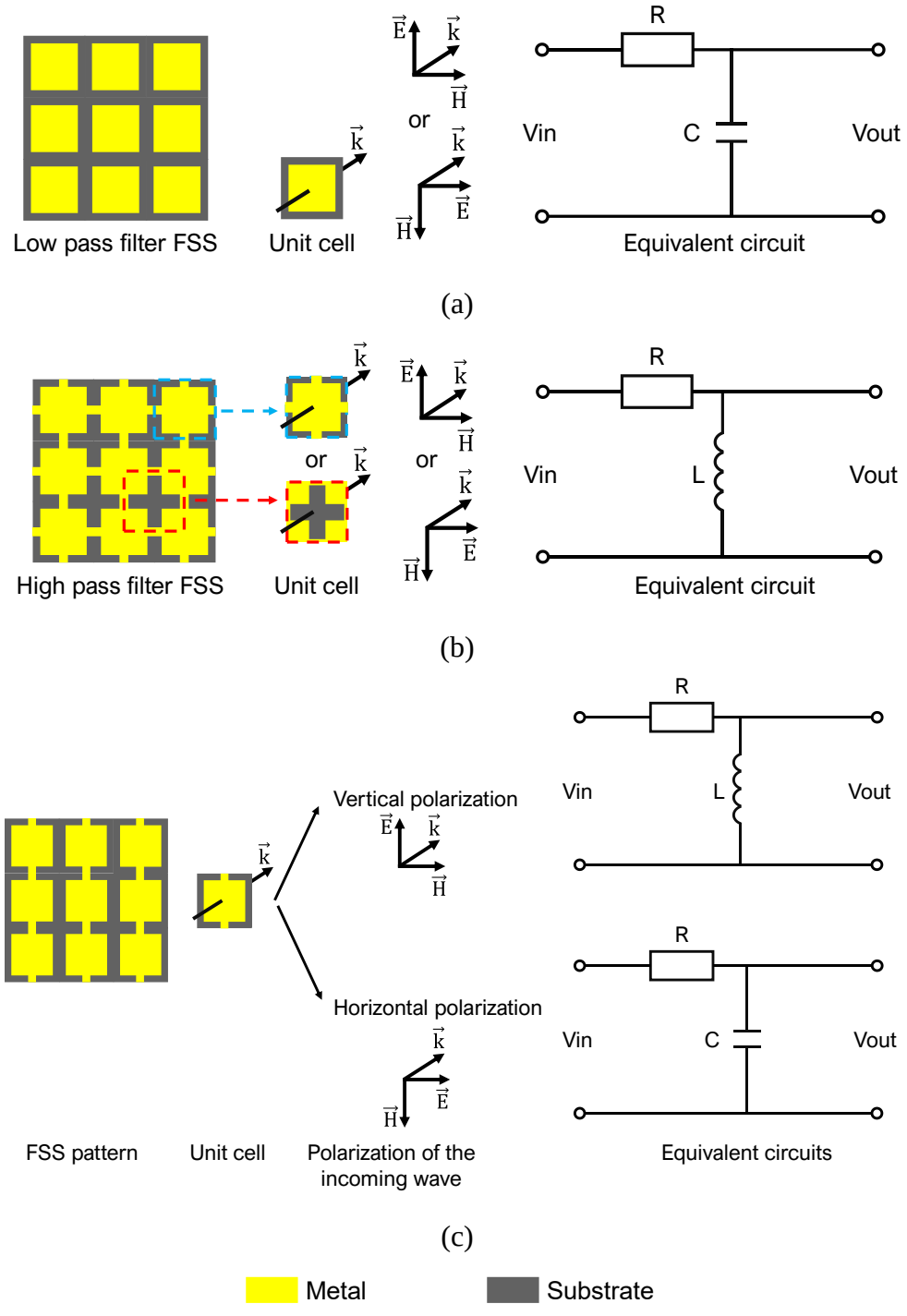

Figure 3-19. FSS unit cells and equivalent circuits (a) Low pass filter (UC1) (b) High pass filter (c) Linear polarization high pass filter (UC2)

- *The first selected unit cell (UC1) – Low pass filter*

The first unit cell (UC1) is a basic unit cell of low pass filter FSS. The general structure and its simplified equivalent circuit are introduced in Figure 3-19(a). Unit cell patches create resistance (R) while gaps between unit cell patches generate capacitance (C). The transfer function of the simplified equivalent circuit of UC1 can be written as (3.1). This is a basic transfer function of a low pass filter. However, the presented equivalent circuit is only a simplified circuit which presents only the most important elements. In this thesis, only equivalent simplified circuits are presented. The full equivalent circuit should include many other sub-elements. The complete transfer function will include several orders of magnitude more than the transfer function in (3.1). Therefore, the simulated transmission coefficient of unit cells will not be exactly the same as the step responses of the simplified transfer functions presented in this section. They will be similar only in terms of trend. However, simplified transfer functions are preferred because they are simple and can still give a prediction of the change in resonant frequency or transmission coefficient of unit cells when unit cell dimensions are changed.

$$H_{UC1}(s) = \frac{1}{sRC + 1} \tag{3.1}$$

Where $s = j\omega$, ω is the angular frequency (rad/s)

- *The high pass filter unit cell*

The high pass filter unit cell is constructed by adding connection lines to UC1, as shown in Figure 3-19(b). The use of connection lines replaces the capacitance C by the inductance (L) in the equivalent circuit. Adding connection lines creates cross-shaped unit cells. Or, from another point of view, we can also say that this structure consists of loop structures with a cross removed in the middle, similar to the typical band stop FSS structure in Figure 3-18(c). The transfer function of the high pass filter unit cell can be written as in (3.2).

$$H_{UC2}(s) = \frac{sL}{sL + R} = \frac{s}{s + \frac{R}{L}} \tag{3.2}$$

This unit cell is capable meeting the set out criteria. However, as discussed above, these designs are towards the prospect of being able to be used with diodes by replacing the connection lines in the design with diodes. Assume that this unit cell is selected, and the four connection lines are replaced by four diodes (two horizontal and two vertical). Constructing a circuit to connect

all diodes, or controlling diodes in separate rows or columns, is difficult. Therefore, in this section, we simplify the high pass filter unit cell to get a more suitable unit cell – the second selected unit cell (UC2) – a linear polarization high pass filter.

- *The second selected unit cell (UC2) – Linear polarization high pass filter*

The structure of UC2 is presented in Figure 3-19(c). Similar to the high pass unit cell, UC2 can also exhibit high pass filtering properties. However, the difference, and also the weakness of UC2 compared to the presented high pass unit cell, is that it can only exhibit high pass filtering properties for incident waves with a vertical polarized incident waves (if assume that the direction of connection lines in UC2 is vertical). With horizontal polarizations, UC2 exhibits low pass filtering properties as UC1. This is the reason why UC2 is called linear polarization high pass filter.

The geometries of selected unit cells are presented in Figure 3-20. Except the connection lines, the dimensions of UC2 are the same as UC1. UC1 is designed to allow waves at 3.6 GHz to pass through (transmission unit cell) while UC2 reflects waves at 3.6 GHz (reflection unit cell).

The substrate dimensions of each unit cell are selected and fixed at 7 mm x 7 mm x 2 mm to ensure that the unit cell is not too small for printing, nor too large and takes up a lot of space. The width of the connection lines in UC2 is also fixed at 1 mm due to the limitation of printing technology.

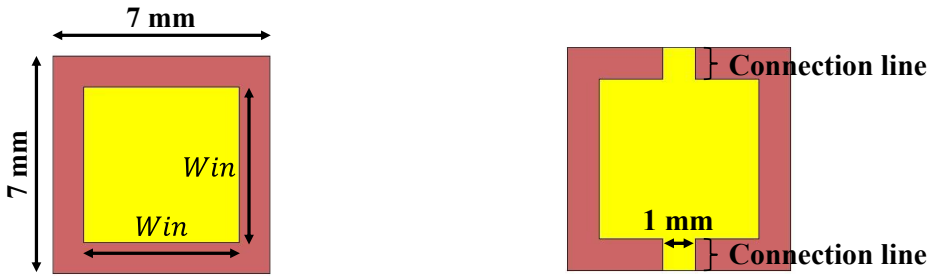

(a) (b)

Figure 3-20. Geometry of (a) Unit cell 1 (UC1) – Transmission unit cell
(b) Unit cell 2 (UC2) - Reflection unit cell

❖ *Effect of W_{in} on unit cell transmission coefficient (S_{21})*

If other dimensions are fixed, the transmission characteristics of both unit cells depend on the selection of W_{in}.

(1) When W_{in} increases, patch area increases while distance between FSS elements decreases.

(2) Thus, R and L will decrease while C will increase, in which, the rate of change of C and L will be faster than R. Therefore, the product $R.C$ and the ratio R/L will increase when W_{in} increase.

(3) From (3.1) and (3.2), we can say that $S_{21} \sim \frac{1}{RC}$ and $S_{21} \sim \frac{1}{R/L}$. Thus, it can be predicted that, if W_{in} increases, transmission coefficient of UC1 and UC2 will both decrease.

Figure 3-21 presents the transmission coefficient versus frequency of UC1 and UC2 when changing W_{in}. As expected, when W_{in} increases, S_{21} of both unit cells decreases. However, this causes a difficulty in choosing the W_{in} value:

- With the transmission unit cell (UC1), a good unit cell should have a highest S_{21} possible (close to zero) at 3.6 GHz to allow the 3.6 GHz waves to pass well. That means W_{in} value must be as small as possible.
- With the reflection unit cell (UC2), a good unit cell needs a S_{21} as small as possible at 3.6 GHz to be able to reflect the entire wave at 3.6 GHz. That means W_{in} must be as big as possible.

Finally, W_{in} was chosen to be equal to 5 mm to give a relatively high S_{21} to UC1 and a relatively small S_{21} to UC2. The simulated transmission coefficient modulus S_{21} of transmission FSS unit cell and reflection unit cell are presented in Figure 3-22.

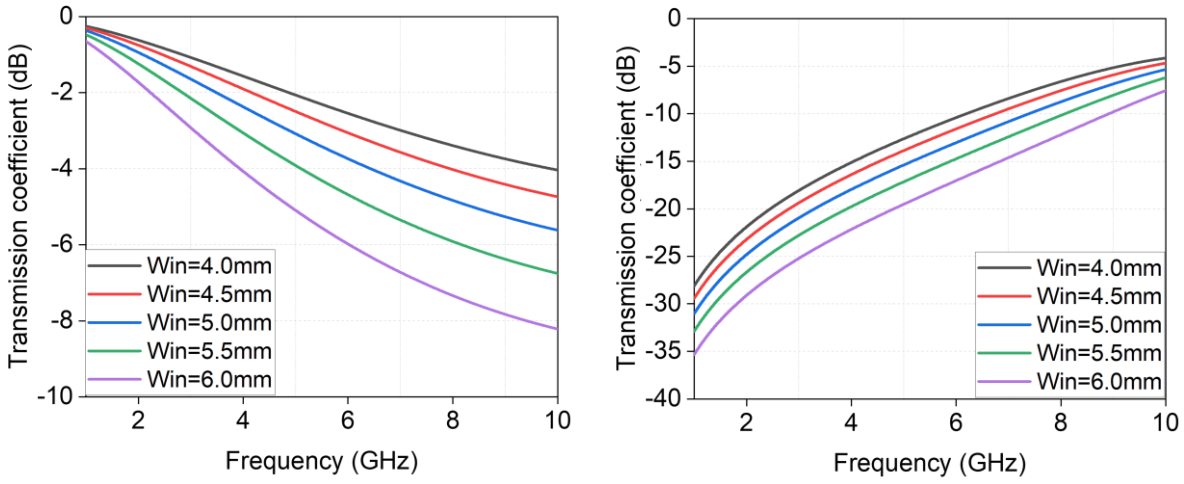

Figure 3-21. Transmission coefficient with difference values of W_{in} of (a) Unit cell 1 (UC1) (b) Unit cell 2 (UC2)

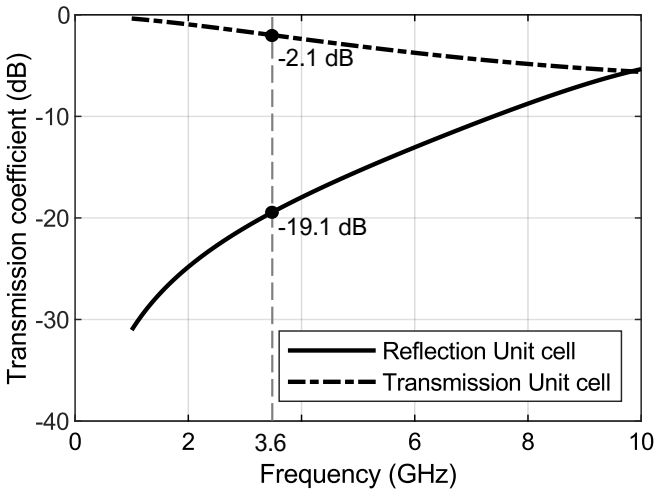

Figure 3-22. Transmission coefficient of unit cells, with W_{in} = 5 mm, in simulation

3.4.3.b. Simulated FSS low pass-based radome

Based on the two selected unit cells, the complete printed FSS pattern is designed. The pattern divides the radome into two halves: half (I), consisting of transmission unit cells (UC1) and half (II) consisting of reflection unit cells (UC2). Consequently, the radome will have one half which is transparent to radiated waves at 3.6 GHz and the other half will prevent 3.6 GHz radiated waves from passing through. In response to the curvilinear structure of the hemisphere, the unit cells have been slightly altered in size and shape from the original structure on planar substrate. The simulated radome with FSS low pass-based pattern is presented in Figure 3-23.

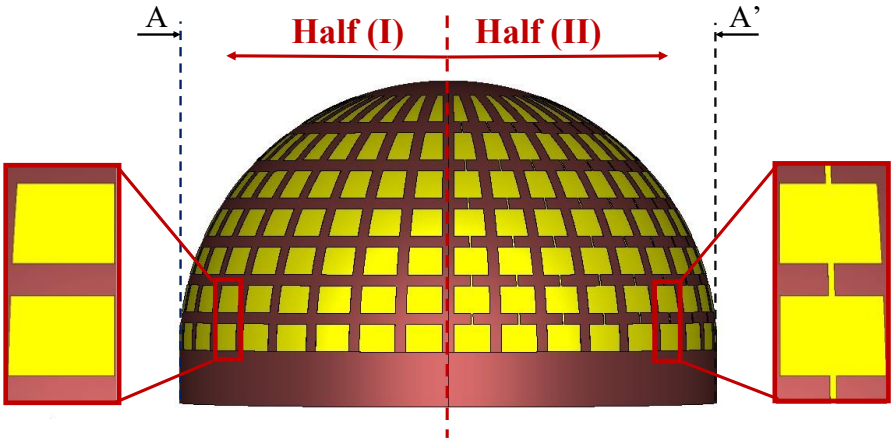

Figure 3-23. Simulated radome with FSS pattern

3.4.3.c. Fabrication and measurement

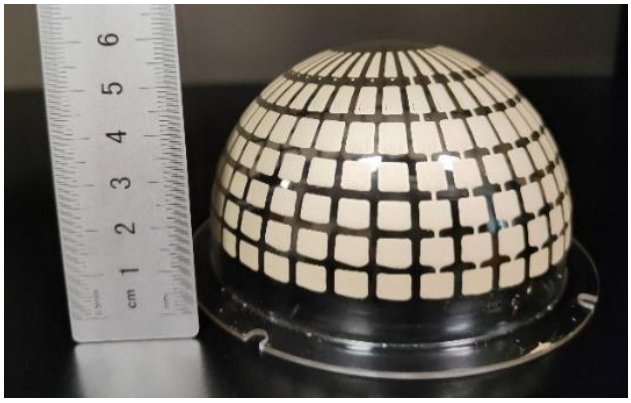

Figure 3-24. Fabricated FSS low pass-based radome

The printed radome is presented in Figure 3-24. Once the radome printing is finished, the antenna - radome system is measured in an anechoic chamber as shown in Figure 3-25. In order to compare the results and evaluate the antenna's navigational effect, two measurements are realized: (1) a measurement of the fabricated patch antenna with the printed radome (2) a measurement of the fabricated patch antenna with the original plastic dome (radome without printed pattern). The measured radiation pattern in the A-A' section of Figure 3-23 for both measurement configurations, and the simulated radiation pattern of the system using the printed radome are shown in Figure 3-26. A good agreement between measurement and simulation is found. We can also see that the antenna main radiation direction has been adjusted to approximately 30 degrees towards the transmission half as expected.

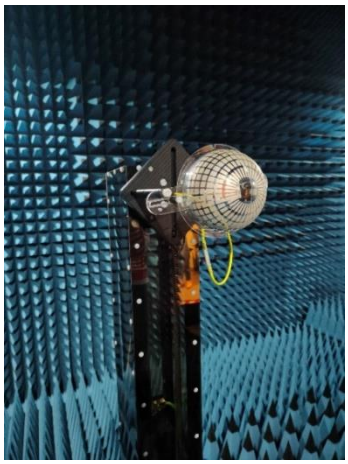

Figure 3-25. System antenna - radome in anechoic chamber

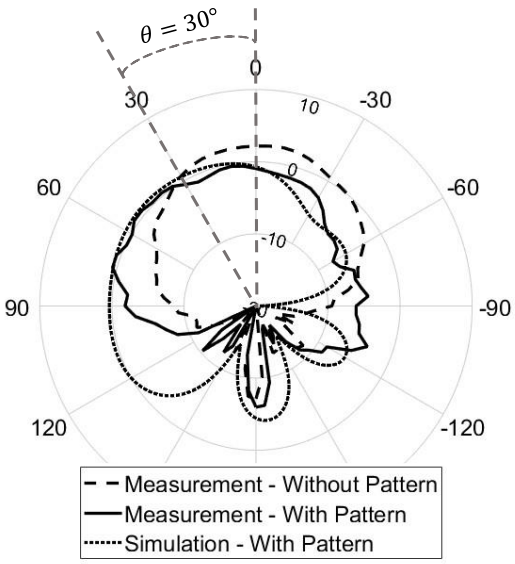

Figure 3-26. Radiation pattern of system antenna - radome in the A-A' section as shown in Figure 3-23

3.4.3.d. Discussion

From the measurement results, some conclusions were drawn:

- There is a good agreement between the measurement and simulation results. Printed pattern has the ability to orient the 3.6 GHz radiated waves about 30 degrees from the main direction.
- The ability to print patterns using jetting technology has been demonstrated. This technology allows performing printing with a measurement result close to the simulation.
- The frequency filtering capability of the FSS pattern which is printed on the radome is close to that of the reference unit cell on the planar substrate. We can say that it is efficient to design unit cells on planar substrates to select a unit cell as a reference for the radome pattern before simulating on the radome surface to simplify the design process and save time.
- The reflectivity of the printed reflection FSS half does not seems strong. In fact, the unit cells in the reflection half are only connected vertically. It means, they have a filtering effect only on wave components whose electric field vectors are parallel to the direction of connection lines in unit cells (vertical). With horizontal wave components, unit cells do not exhibit filtering properties. Therefore, horizontal polarized waves can still penetrate the reflection FSS.

One problem was found in the printing process. The use of full rectangles in the low pass unit cell causes certain difficulties in the fabrication process. To print an entire rectangle, the system must print many small lines with a width of 0.7-0.8 mm until the rectangle is filled. This process is very time-consuming. In addition, when printing the entire rectangles and drying the structure at room temperature, ink flow (downward) phenomenon may occur, as shown in Figure 3-27, especially when the room temperature is higher than usual. Therefore, the filled rectangular structure is not an ideal structure for printing.

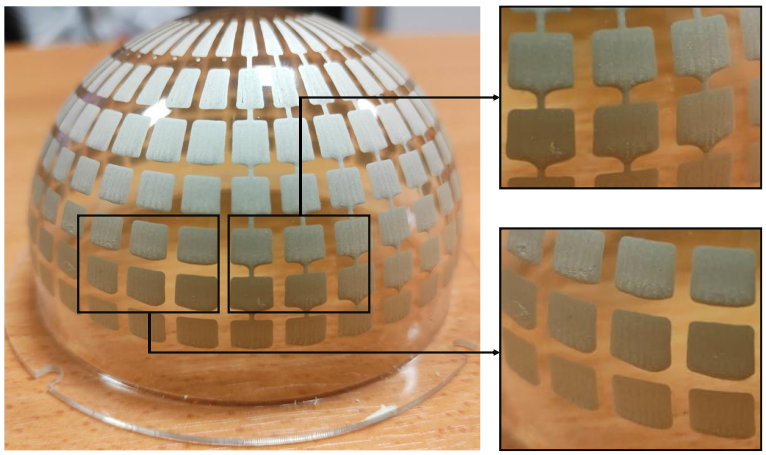

Figure 3-27. Ink flow phenomenon on the radome surface

To solve this problem, an alternative solution has been proposed: use a resonant band stop FSS (as shown in Figure 3-18(c)) instead of the low pass-based FSS. This solution is chosen because the printing process for this type of unit cell does not require as long printing as for the low pass filter. Thus, ink flow phenomenon can be limited. In addition, the printing area of a unit cell is smaller than the low pass unit cell, so the printing time will be saved.

This solution will be presented in detail in the following section (Section 3.4.4). In the upcoming section, in addition to changing the unit cell type, there are two other changes that will be implemented:

- An attempt to use diodes instead of connection lines between two unit is studied. Thus, there will be only one type of unit cell in the structure. The use of diodes will help switch between two states of the unit cells - transmission or reflection. Controlling the operation of these diodes will help control the direction of the antenna main beam.
- The resolution of the printed pattern is reduced. In the previous configuration, there are a total of 37 columns of unit cells. In other words, if diodes are used on each column, the smallest beam controllable vertical angle is 10 degrees. Or we can say that the

resolution of the low pass printed pattern is 10 degrees. Printing these 37 columns is time consuming. So, in the next section, the resolution will be increased to 90 degrees. That is, the antenna main direction will change within a limit of 4 different directions.

3.4.4. FSS Resonant Band Stop-based Printed Radome

3.4.4.a. FSS resonant band stop-based pattern

❖ *General ideal description*

Figure 3-28 describes the ideal transmission coefficient for the desired unit cell. Diodes are used in the unit cells. Controlling the ON and OFF states of the diode can control the unit cell transmittance. In the ideal transmission coefficient, there exists at least one passband frequency (f_p), where the transmission coefficient is close or equal to 0 dB, and one zero-transmission frequency (f_z), where the transmission coefficient is the lowest. The resonant band stop unit cell in this section is designed based on the following ideas:

- When the diodes are OFF, zero-transmission frequency $f_{z\_OFF} \approx 3.6$ GHz, which means the unit cells will reflect the radiated wave at 3.6 GHz.
- When the diodes are ON, passband frequency $f_{p\_ON} \approx 3.6$ GHz, which means the unit cells will allow the radiated wave at 3.6 GHz to pass through.

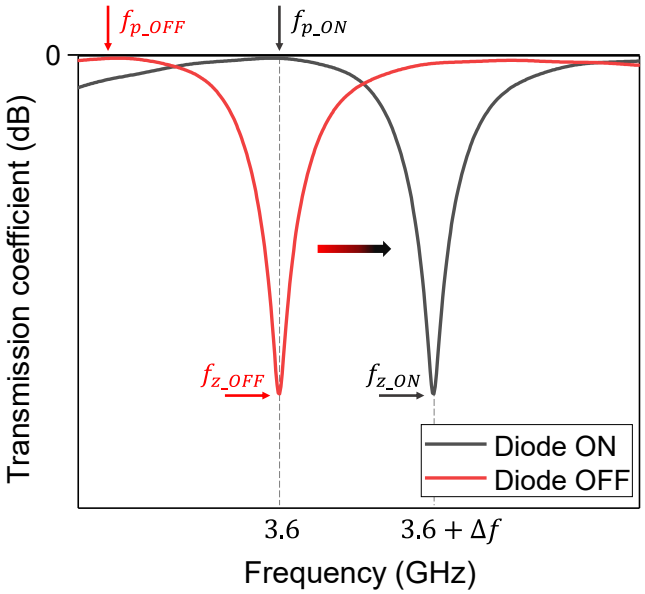

Figure 3-28. Transmission response of band stop FSS

In the first part of this section, to simplify the design in the simulation, the biased diode will be replaced by a strip conductor. When the expression "diode is ON" is used, it is equivalent to

having the FSS elements connected by strip conductors. Specifically, in the simulations presented afterward, a strip conductor with a width of 0.8 mm is used to replace the diode.

❖ *Unit cell geometry description*

Figure 3-29(a) presents the geometry of the resonant band stop unit cell. The unit cell is based on the basic band stop unit cell, which was presented in Figure 3-18(c). Strip conductors (sometimes called connection lines) appear in the design to prepare for diode mounting in later steps. Equivalent strip conductors representing the OFF/ON states of the diode, which are used in CST Studio Suite simulations, are presented in Figure 3-29(b). When the diode is OFF, two adjacent unit cell strip conductors of are not connected. When the diode is ON, these strip conductors are connected. The simplified equivalent circuits of the unit cell when diodes are OFF/ON are introduced in Figure 3-30. The small circuit, L in parallel with C, represents the rectangular ring structure. When the diode is OFF, the capacitance C_1 is generated by the distance between FSS elements. When the diode is ON, all elements of FSS are connected, and as a sequence, L_1 is created.

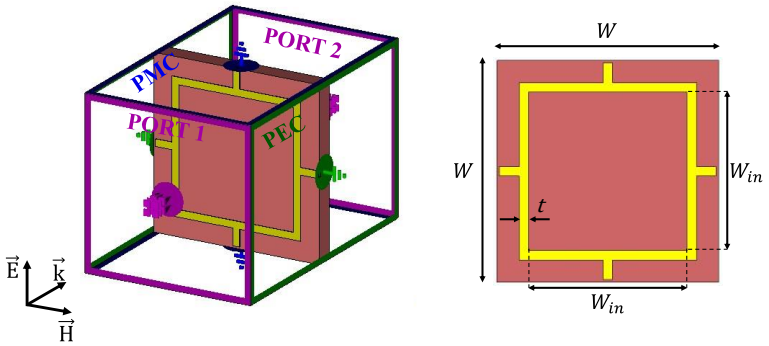

(a)

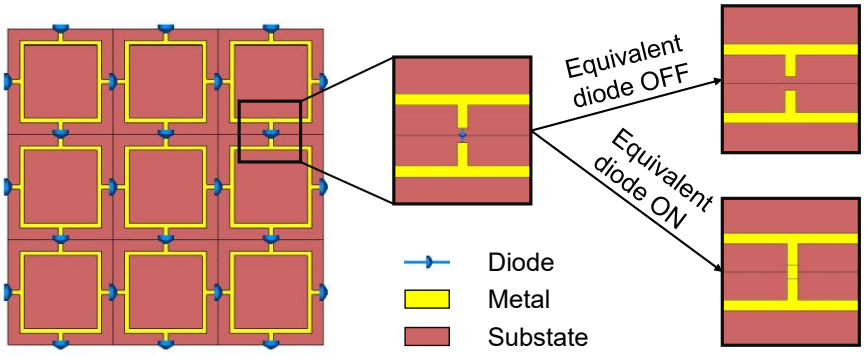

(b)

Figure 3-29. (a) Geometry of unit cell (b) FSS and equivalent strip conductors for ON and OFF states of diode

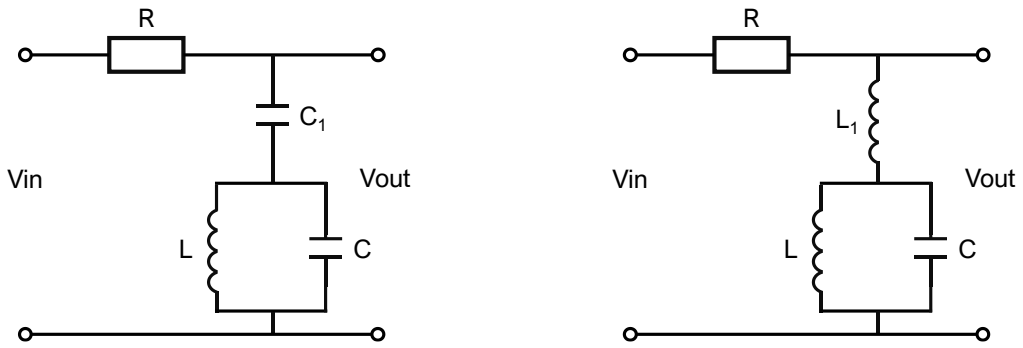

(a) (b)

Figure 3-30. Equivalent circuit of unit cell when (a) Diode is OFF (b) Diode is ON

❖ *Unit cell parameters effects*

The transfer function ($Vout/Vin$) of the unit cell when the diode is OFF ($H_{OFF}(s)$) in linear scale can be written as in (3.3). By making the numerator of $H_{OFF}(s)$ equal to 0, the zero of the function (or zero-transmission frequency f_z) is found as (3.4). Similarly, the transfer function of the unit cell when the diode is ON ($H_{ON}(s)$) can be written as (3.5). The zero-transmission frequency with the ON diode can be calculated as (3.6).

$$H_{OFF}(s) = \frac{1 + s^2(LC + LC_1)}{1 + sRC_1 + s^2(LC_1 + LC) + s^3RLCC_1} \tag{3.3}$$

$$f_{z\_OFF} = \frac{1}{2\pi\sqrt{L(C + C_1)}} \tag{3.4}$$

$$H_{ON}(s) = \frac{s(L + L_1) + s^3LL_1C}{R + s(L + L_1) + s^2RLC + s^3LL_1C} \tag{3.5}$$

$$f_{z\_ON} = \frac{1}{2\pi} \times \sqrt{\frac{L + L_1}{LL_1C}} \tag{3.6}$$

$$\frac{f_{z\_OFF}}{f_{z\_ON}} = \sqrt{\frac{L_1C}{(C + C_1)(L + L_1)}} \tag{3.7}$$

We can see from (3.7) that $\frac{f_{z\_OFF}}{f_{z\_ON}} < 1$. It means that the zero-transmission frequency in diode OFF state (f_{z_OFF}), is lower than the zero-transmission frequency in diode ON state. This sequence is consistent with the desired transmission coefficients in Figure 3-28.

To get the desired transmission coefficients, the current goal is that f_{z_OFF} must be close to the passband frequency in diode ON state (f_{p_ON}). Passband frequency f_p, in general, can be obtained when the numerator and the denominator of transfer function $H(s)$ are close or equal. By setting the numerator and denominator of $H_{ON}(s)$ in (3.5) equal, we obtain a f_{p_ON} as (3.8).

$$f_{p\_ON} = \frac{1}{2\pi\sqrt{LC}} \tag{3.8}$$

$$f_{z\_OFF} \approx f_{p\_ON} \leftrightarrow \frac{1}{\sqrt{L(C + C_1)}} \approx \frac{1}{\sqrt{LC}} \tag{3.9}$$

From (3.9), we see that to achieve a f_{z_OFF} approximately equal to f_{p_ON}, C_1 must be as small as possible. Reducing the width of the connection lines (strip conductors representing diodes) can reduce C_1. It means these connections should be as small as possible. However, due to the limitation of the circuit fabrication method (3D jetting), the minimum width that can be achieved is 0.8 mm. To ensure printability but still obtain a small C_1, the width of the connector is fixed to 0.8 mm.

To achieve $f_{z\_OFF} = 3.6$ GHz, it is necessary to build a structure with suitable L and C values through choosing t, W and W_{in}. To simplify pattern printing, t is fixed at 0.8 mm, equal to the width of the strip conductor that the robot can print in one move. This will simplify the printing process and save time. Similar to the low pass unit cell, W will be fixed so that the structure has a reasonable size. In this design, W is fixed at 19 mm. Therefore, the unit cell properties will be controlled through W_{in}.

Figure 3-31 shows the transmission coefficient of the unit cell with different values of W_{in} when the diode is OFF and ON. It can be seen that, when W_{in} increases, both f_{z_OFF} and f_{p_ON} decrease. W_{in} is selected so that f_{z_OFF} = 3.6 GHz. In simulation, when W_{in} = 13.2 mm, f_{z_OFF} = 3.6 GHz. Table 9 is the summary of unit cell dimensions.

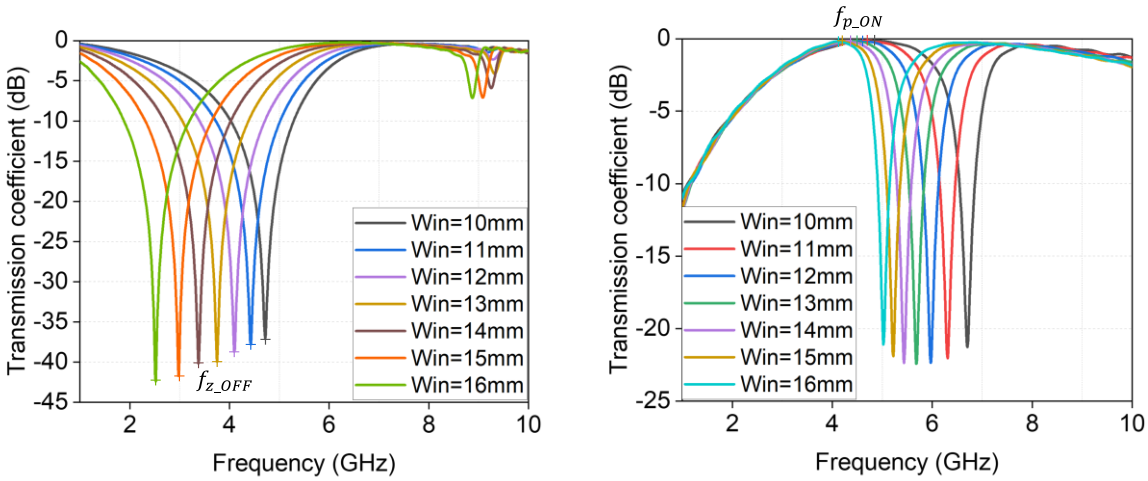

(a) (b)

Figure 3-31. Simulated transmission coefficient of unit cell with different W_{in} (a) Diode is OFF (b) Diode is ON

Table 9. Dimensions of band stop unit cell

Parameters	W	W_{in}	t
Values (mm)	19	13.2	0.8

The simulated transmission coefficient of the final resonant band stop unit cell is presented in Figure 3-32. It can be seen that when the diode is OFF, the zero-transmission frequency of the FSS is 3.6 GHz. When the diode is ON, 3.6 GHz does not precisely coincide with the passband frequency of the FSS but the transmission coefficient at 3.6 GHz still reaches a pretty good value of -1.3 dB. This deviation comes from the width of the connection lines representing the diodes being quite large, resulting in the C_1 value being quite significant. This difference can be adjusted through proper diode selection.

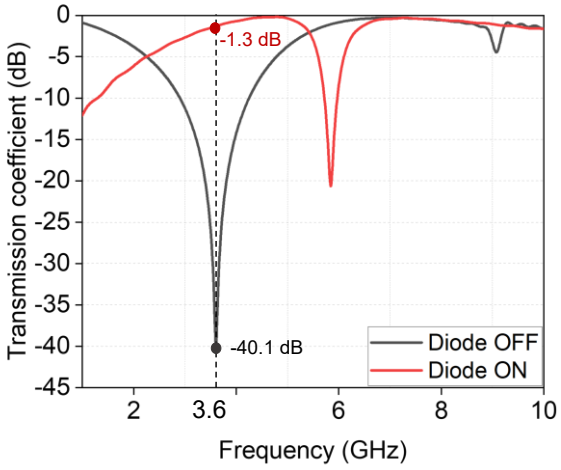

Figure 3-32. Simulated transmission coefficient of FSS when the diode is OFF and ON

3.4.4.b. Diode

Diodes are used to connect the FSS elements to control the system. The choice of the diode should be considered because the diode structure and parameters will affect the FSS transmission property. In our work, the diode was selected based on the following aspects:

- Internal properties of diodes: The equivalent circuit for the OFF/ON state is presented in Figure 3-33. In state OFF, the diode contributes a certain amount of capacitance (C_s) to the FSS unit cell. This value will affect the serial capacitance C_1 of the unit cell (which is introduced in Figure 3-30, section *3.4.4.a*). As presented in section *3.4.4.a*, to have $f_{z\_OFF} \approx f_{p\_ON}$, the value of C_1 needs to be small. Thus, C_s needs to have a small value as well. Therefore, the first criterion for choosing a diode is that it should have a small capacitance.
- Packaging: The size of the diode packaging will affect the electromagnetic wave. A large packaging will disturb waves. If a big diode is chosen, the effect of its package becomes significant. Therefore, small size is the second criterion for diode selection.
- Price: In the FSS structure, the number of diodes that need to be used is not small. Therefore, choosing a diode with a reasonable price also must be considered as the third criterion.

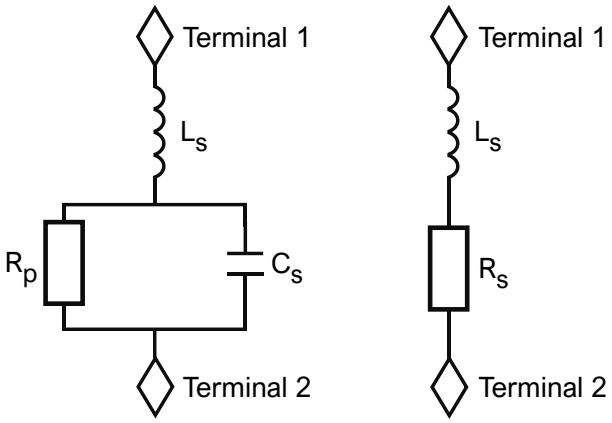

Figure 3-33. Equivalent circuit of diode in (a) ON state (b) OFF state

Table 10 presents some candidates for the diode. These candidates all have relatively small packaging sizes. Among those diodes, based on the balance between the internal capacitance value and the price, the diode SMPA1345-040LF was chosen to use in the design. The measured

forward current and the calculated diode resistance versus forward voltage of SMPA1345-040LF are presented in Figure 3-34.

Table 10. Information of some candidate diodes

Name	Internal Capacitance (pF)	Package	Price (euro)/unity (In *Mouser*)
GMP4201-GM1	0.07	SOD-323 (1.7 x 1.25 x 0.95 mm)	3.41
SMPA1345-040LF	0.15	SOD-882 (1.0 x 0.6 x 0.5 mm)	0.83
BAR 64-02EL	0.53	TSLP-2-19 (1.0 x 0.6 x 0.31 mm)	0.47
1SS390SMFH	1.2	SOD-523 (1.2 x 0.8 x 0.6 mm)	0.42

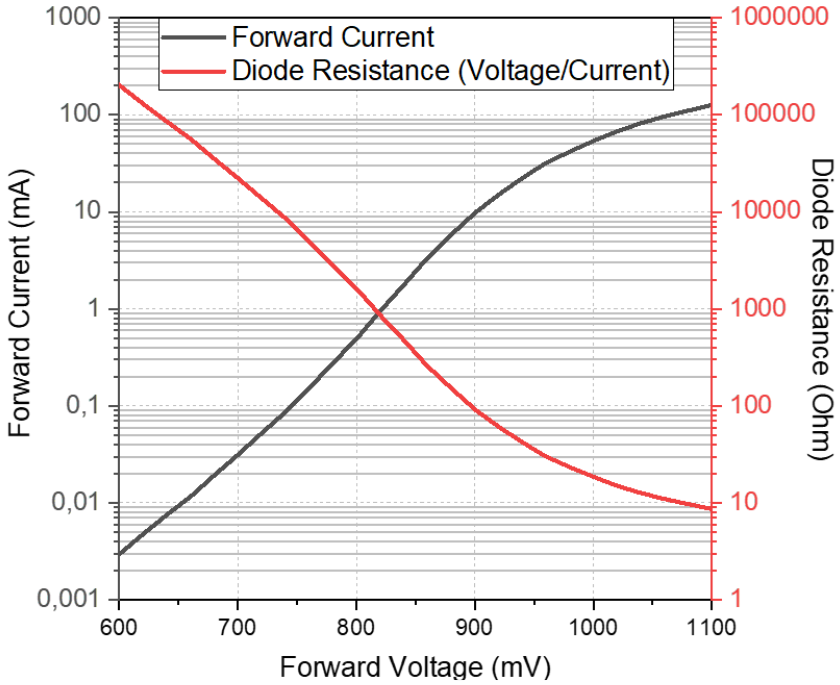

Figure 3-34. Measured forward current and calculated diode resistance versus forward voltage of the diode SMPA1345-040LF

Equivalent circuits in Figure 3-33 is used to replace the diode in CST Studio Suite simulations with the following set of parameters: L_s = 0.45 nH, C_s = 0.15 pF, R_s = 20 Ω and R_p = 55000 Ω.

The value of R_s does not affect the resonant frequency of the transmission coefficient, but it changes the level of the transmission coefficient at that frequency. Figure 3-35 shows the simulated transmission coefficient using the equivalent circuits with the presented set of parameters (L_s, C_s, R_s, R_p) for the diode OFF/ON. In addition, this figure also presents the transmission coefficient when using a different value of R_s (R_s=1.5 Ω) to see the effect of R_s. We can see that, increasing the value of R_s will decrease the transmission coefficient level at 3.6 GHz, which is not good for the design. To decrease the value of R_s, it is necessary to increase the voltage applied to the diode. However, this increases the possibility of diode breaking. In conclusion, when choosing a diode, besides the low capacitance, a diode with low resistance (V/I) should be selected.

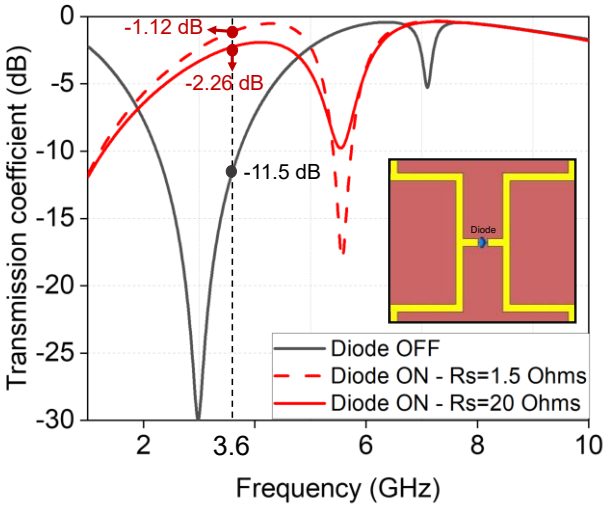

Figure 3-35. Transmission coefficient of FSS with diode, simulated in CST Studio Suite

Compare the S_{21} of FSS when using a diode, as presented in Figure 3-35, and the S_{21} of FSS when using the equivalent strip conductors, as in Figure 3-32, we can see that the use of a diode changes the value of f_{z_OFF}. The value of f_{z_OFF} is reduced when using a diode, so 3.6 GHz is no longer the zero-transmission frequency of the system. However, the S_{21} value at 3.6 GHz still reaches -11.5 dB, so the FSS filtering capacity at 3.6 GHz is still quite good. To bring 3.6 GHz back to f_{z_OFF} when using diodes, we can reduce the W_{in} value. However, reducing the W_{in} value will shift S_{21} when diodes are ON to the right. The value of S_{21} at 3.6 GHz in the diode ON state is reduced. In other words, the transmittance of the FSS when diodes are ON is worse. Thus, we decided to keep the original value of W_{in} (W_{in} = 13.2 mm).

Figure 3-36 shows the effect of diode packaging on the FSS transmission coefficient (assuming that no electrical equivalent circuit is used). The diode packaging is simulated, including a

silicon body with dimensions of 1 mm x 0.6 mm x 0.4 mm and two silver pins below the body with dimensions of 0.25 mm x 0.5 mm x 0.04 mm. We can see that, if only the physical effect of the packaging is considered (without considering the electrical effect), the diode will only change the zero-transmission frequency a little. This effect is much less than the diode electrical effect. Combining both effects (diode packaging and electrical equivalent circuit), when using a diode in the OFF state, the FSS has a transmission coefficient of approximately -10 dB at 3.6 GHz. This value is still enough to say that when the diode is OFF, the FSS can filter and remove the waves at 3.6 GHz.

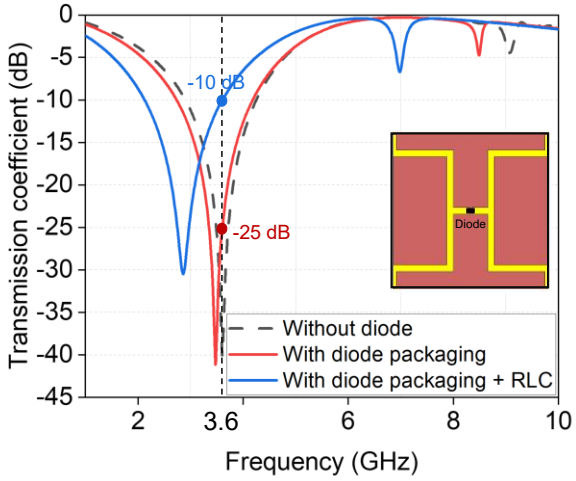

Figure 3-36. Effect of diode packaging on FSS, when diodes are not forward biased

3.4.4.c. 1D FSS

To verify the diodes, FSS performance, and the consistency between simulation and measurement, the 1D FSS is fabricated and measured. This process also helps verify difficulties encountered while working with the diode before fabricating FSS on the hemisphere dome. 1D FSS is realized on a planar substrate. The fabricated FSS unit cell is the resonant band stop, as analyzed in the last section (*3.4.4.b)*. However, unit cell dimensions will be re-selected to adapt to changes in planar FSS fabrication. There are two constraints for the 1D FSS fabrication:

- The configuration to measure the transmission coefficient of the FSS is illustrated in Figure 3-37. The FSS must be large enough to be attached to the measurement window. The size of the window is 110 mm x 180 mm. FSS must be larger than this size.
- The number of unit cells should not be too large to avoid exploding the number of required diodes.

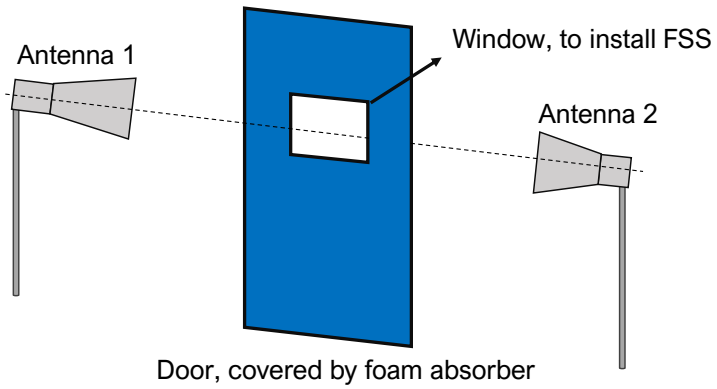

Figure 3-37. Configuration to measure the FSS transmission coefficient

After considering these two constraints, we decided to increase the unit cell size. The substrate width of a unit cell (W in Figure 3-29) is increased from 19 mm (in section *3.4.4.b*) to 25 mm. Thus, the number of unit cells and diodes will be reduced. If W increases while keeping W_{in} unchanged, the length of the connection line also increases. So, the value of L in (3.4) ($f_{z\_OFF} = \frac{1}{2\pi\sqrt{L(C+C_1)}}$) increases, leading to a decrease in the f_{z_OFF}. To ensure that the zero-transmission frequency in diode OFF state is still 3.6 GHz, it is necessary to reduce W_{in}.

To fabricate the planar FSS, LPKF engraving machine is used. Thanks to the manufacturing technique, the strip conductor width can be reduced. We decided to reduce the width of strip conductors between unit cells, which are used to mount diodes, to reduce the difference between f_{z_OFF} and f_{p_ON}. The strip conductor width after being reduced is 0.4 mm.

In the last sections, unit cells are simulated on the acrylic substrate of the radome base. However, we do not have a planar acrylic substrate. Therefore, Roger 4003C substrate ($\varepsilon_r = 3.55, tan\delta = 0.0027$ at 10 GHz) is selected for 1D FSS fabrication. Changing the dielectric substrate (or, changing the dielectric permittivity) changes the unit cell zero-transmission frequency.

❖ *Dielectric substrate effects*

To investigate the effect of substrate on FSS properties, an approach can be obtained by using substrate equivalent circuit as introduced in [94]. However, we take a different approach in this section, through equivalent substrate, to study dielectric substrate effects on FSS unit cell.

In previous sections, the dielectric substrate did not change when studying the effects of unit cell parameters. The capacitance of FSS unit cells was performed by assuming that the FSS was

in a homogeneous medium. In practice, the FSS patterns lie at the boundary between two mediums: air and dielectric as shown in Figure 3-38(a).

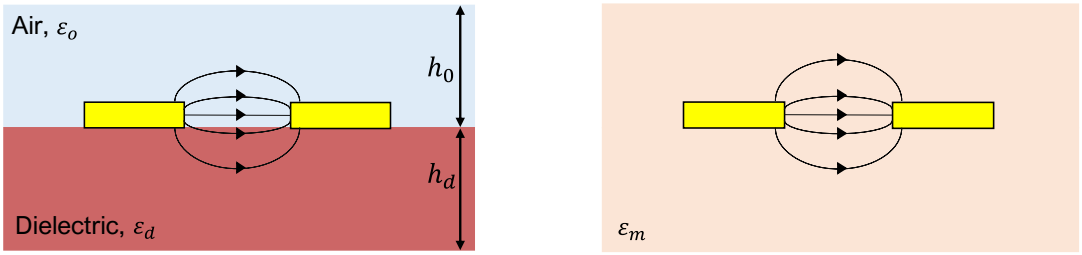

(a) (b)

Figure 3-38. Coupling between two metallic lines of FSS unit cell (a) Between the two mediums: air and dielectric (b) In an equivalent mixture of air and dielectric

The capacitance between two parallel metal plates in a homogeneous medium can be calculated as the formula (3.10).

$$C = \frac{\varepsilon . A}{d} \tag{3.10}$$

Where:

C: Capacitance (Farads)

ε: Permittivity of medium

A: Area of plate overlap (m^2)

d: Distance between two plates (m)

This formula only applies to homogeneous media. In our case, the coupling phenomenon, which causes capacitance, occurs in two different environments. Therefore, applying the above formula to calculate capacitance directly is impossible. A proposed solution to simplify this case is to use an equivalent dielectric, with a permittivity of ε_m, for the mixture of air and dielectric, as illustrated in Figure 3-38(b). This way, the formula (3.10) can be used with $\varepsilon = \varepsilon_m$. To calculate ε_m, we assume that the permittivity and thickness of the air layer are ε_o and h_o, and of the dielectric layer are ε_d and h_d. Based on [95], ε_m can be approximated as:

$$\varepsilon_m = \left({\varepsilon_o}^{1/2} + v_d . \left({\varepsilon_d}^{1/2} - {\varepsilon_o}^{1/2}\right)\right)^2 \tag{3.11}$$

Where, v_d is the volumetric proportion of the dielectric in the air and dielectric mixture.

Assuming that the horizontal surface area of the air and the dielectrics are the same, v_d can be written as:

$$v_d = \frac{h_d}{h_d + h_o} \quad (3.12)$$

From (3.10), (3.11) and (3.12), we have:

$$C = \left({\varepsilon_o}^{1/2} + \frac{h_d}{h_d + h_o} . \left({\varepsilon_d}^{1/2} - {\varepsilon_o}^{1/2} \right) \right)^2 . \frac{A}{d} \quad (3.13)$$

From (3.4), we know that $f_z \sim \frac{1}{\sqrt{C}}$. Combined with (3.13), we have some conclusions:

- If the substrate permittivity decreases while other parameters are unchanged, C will decrease. Therefore, the zero-transmission frequency (f_z) will increase.
- If the substrate height decreases while other parameters are unchanged, C will decrease. Therefore, the zero-transmission frequency (f_z) will increase. However, the rate of change of $\frac{h_d}{h_d+h_o}$ is slower than that of ε_d. So, the frequency change rate when changing the substrate thickness is slower than when changing the substrate permittivity.

These conclusions are demonstrated through simulation results when changing the substrate permittivity and height while keeping other parameters as shown in Figure 3-39.

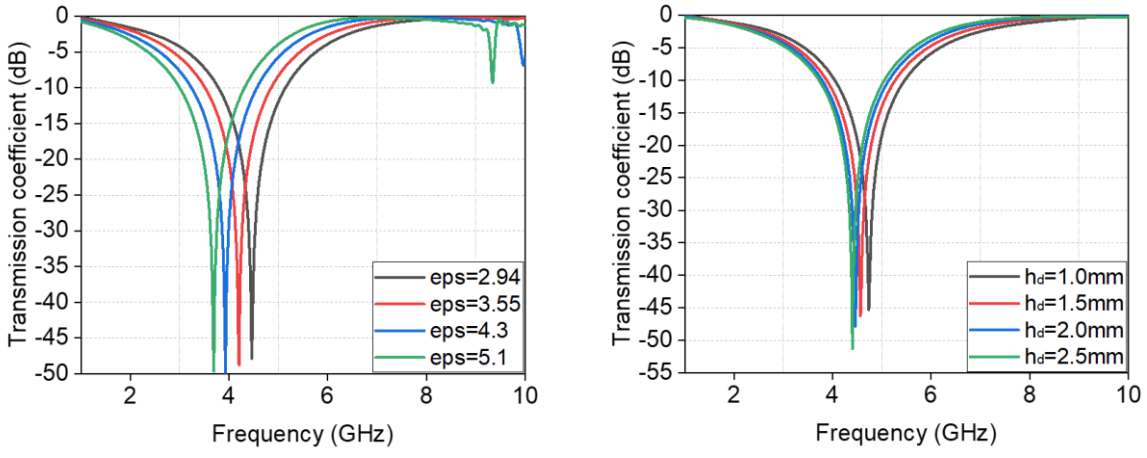

(a) (b)

Figure 3-39. Transmission coefficient of FSS when changing (a) Substrate permittivity (*eps*) (b) Substrate height (*h*)

In conclusion, when changing the substrate from acrylic (ε_d = 5.1, h_d = 2 mm) to the RO4003C dielectric with (ε_d = 3.55, h_d = 1.524 mm), the zero-transmission frequency in diode OFF state

f_{z_OFF} increases. As a sequence, W_{in} needs to be increased to bring the resonant frequency back to 3.6 GHz. The final dimensions of the unit cell are shown in Figure 3-40(a). The W_{in} is chosen so that the zero-transmission frequency when no diode is mounted on the circuit, is 3.6 GHz.

❖ *Incident wave polarization effects*

To verify the effect of incident wave polarization on the FSS, diodes are mounted in only one direction. In our design, we assume that only diodes in vertical columns are mounted and used. Figure 3-40(b) presents the simulated transmission coefficient of the unit cell in fours case:

(1) No diode is mounted on the unit cell ("Without diode", black line)

(2) All diodes in vertical columns are mounted, but they are not forward-biased. The incident wave has vertical polarization ("With diode OFF – Vertical pol.", red line)

(3) All diodes in vertical columns are mounted and forward-biased. The incident wave has vertical polarization ("With diode ON – Vertical pol.", blue line)

(4) All diodes in vertical columns are mounted and forward-biased. The incident wave has horizontal polarization ("With diode – Vertical pol.", yellow line)

We can see that, in the simulation, adding diodes will reduce the value and level of zero-transmission frequency f_z (sometimes called resonant frequency). When the diode is attached to the circuit but not forward-biased, the FSS exhibits a filtering property at 3.6 GHz but is not as powerful as when the diode is not attached. The simulation results also show that when the diode is turned ON, FSS will allow waves at 3.6 GHz with vertical polarization to pass through and block waves at 3.6 GHz with horizontal polarization.

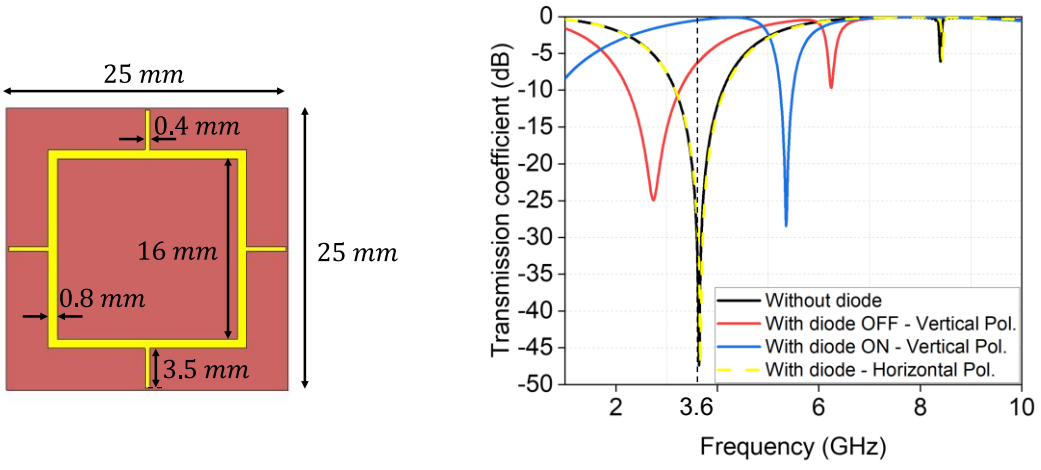

(a) (b)

Figure 3-40. (a) Unit cell geometry of FSS (b) The transmission coefficient of FSS in difference scenarios

The geometry of the 1D FSS in the simulation is presented in Figure 3-41(a). In this structure, two strip conductors are added to supply a DC voltage to the diodes. Only diodes on vertical columns are used. The fabricated 1D FSS is presented in Figure 3-41(b). Some problems encountered in the manufacturing process that need to be considered:

- The chosen diode is sensitive. Therefore, in manipulating diodes, it is necessary to limit direct body contact with diodes because contact can cause discharge and damage diodes.
- The diode size is small. Soldering the diode onto the circuit by hand is impossible. To overcome this, diodes were attached to the FSS circuit using conductive glue. With this RC4003C substrate, conventional conductive glues can be used since the substrate is heat resistant for the glue curing process in the oven. However, the acrylic plastic of the radome base cannot withstand high temperatures above 60 degrees. Therefore, conventional conductive glues cannot be applied as they need to be cured in an oven at a relatively high temperature, above 60 degrees. To solve this problem, a conductive glue capable of drying at room temperature is proposed in the diode mounting process on the radome. In 1D FSS, this conductive glue is also used to attach the diode to the circuit.

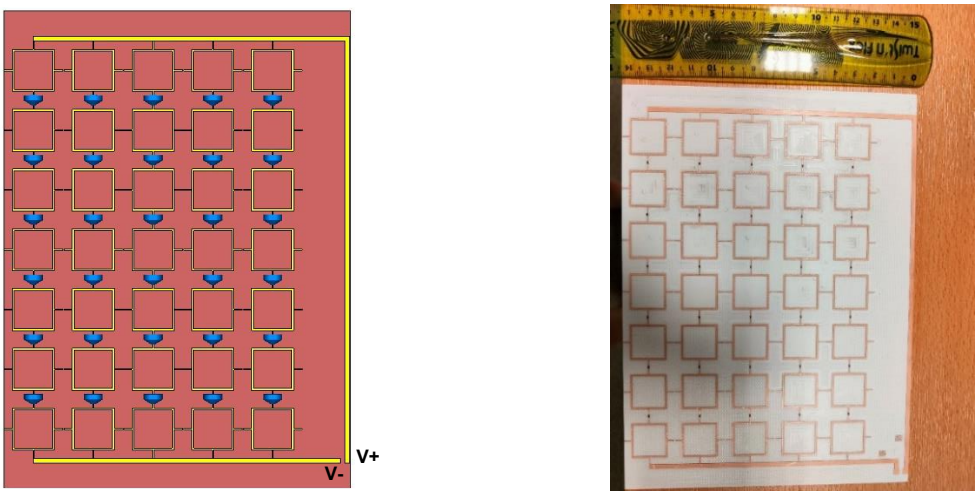

(a) (b)

Figure 3-41. (a) 1D FSS geometry in simulation (b) Fabricated 1D FSS using RO4003C

The measurement results are presented in Figure 3-42.

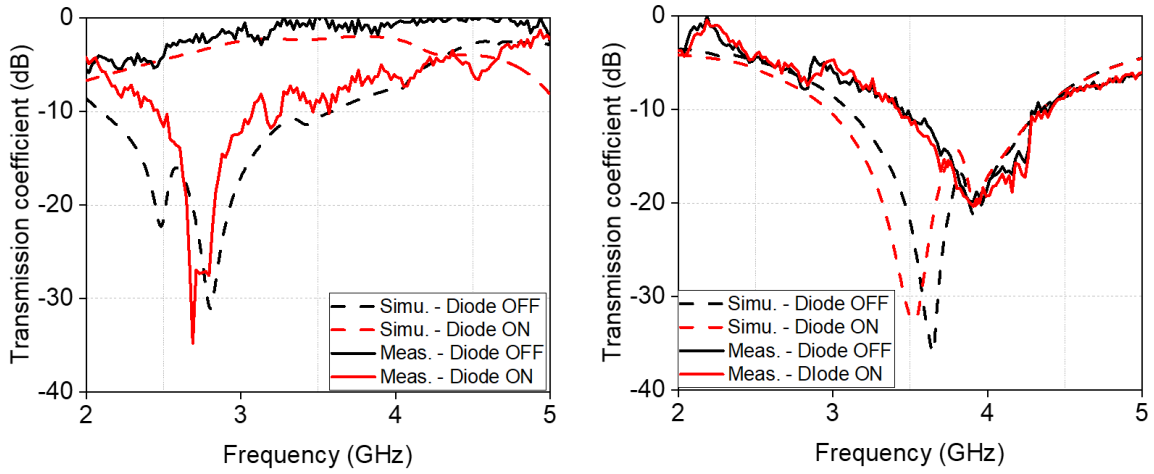

(a) (b)

Figure 3-42. Measured and simulated transmission coefficient of 1D FSS when diodes are off and on, when applied waves have (a) Vertical polarization (b) Horizontal polarization

3.4.4.d. FSS band stop-based radome simulation and fabrication

After designing and studying the FSS structure on the plane, the FSS pattern for the radome is simulated and fabricated. The pattern for the radome is designed based on the unit cell selected in section *3.4.4.a* ($W = 19\ mm, W_{in} = 13.2\ mm$). Similar to the previous sections, the diodes will be connected in columns, or in other words, the radome when the diodes are active will show the transmittance only for the longitudinally biased component (parallel to the diode mounting column). The simulated radome and the fabricated radome are presented in Figure 3-43. Due to some technical reasons, the process of mounting the diode on the radome and the measurement process has not been completed yet. The simulated 3D radiation patterns of the system radome – antenna when all diodes are ON and OFF are presented in Figure 3-44.

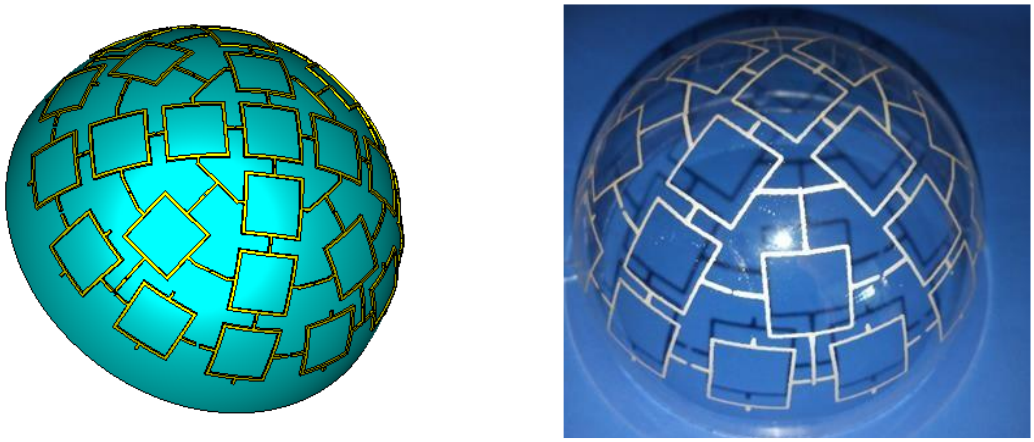

(a) (b)

Figure 3-43. (a) Simulated radome (b) Printed radome

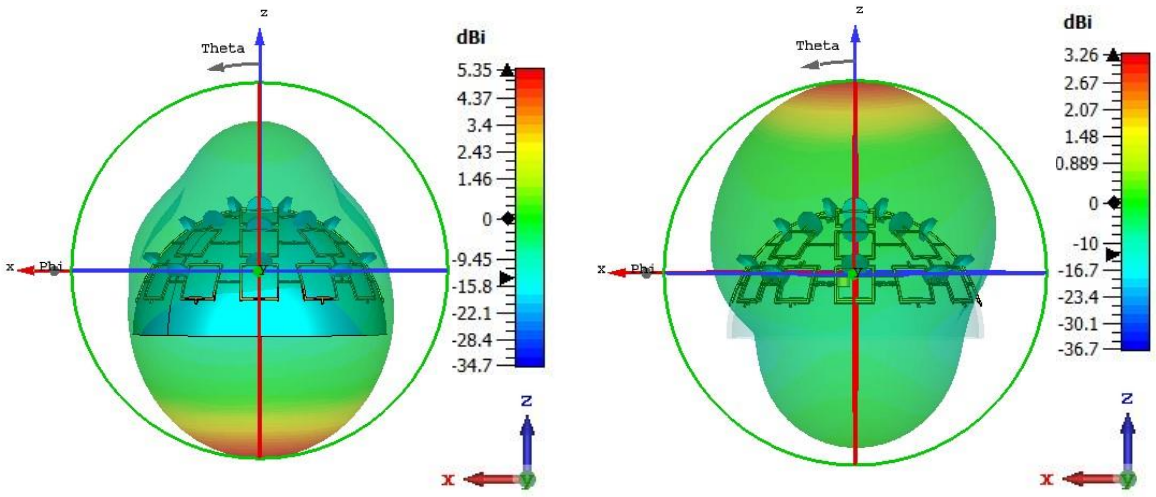

(a) (b)

Figure 3-44. Simulated 3D radiation pattern of system radome - antenna when (a) All diodes are OFF (b) All diode are ON

3.5. Conclusion

In this chapter, we have demonstrated the application of a new technique - 3D jetting in some RF applications, specifically in the fabrication of printed radome. This printing technique allows printing on 3D surfaces directly without contact.

Using 3D jetting for printing begins with a simple pattern - the reflector ring. This motif is printed on the surface of the radome aiming to reflect the second beam and improve the main beam of the antenna. The measurement results are quite similar to the simulation results.

Then a more complex pattern - low pass based FSS was implemented printed on the surface of the radome. There is coherence between the measurement and simulation result. Some printing problems were also found.

Finally, the resonant band stop FSS is printed on the surface of the radome. This FSS structure is used in conjunction with the diode to be able to control the radiated insulation of the antenna.

There are still some problems such as ink flow, printing size limitation. However, this printing technique is still very promising in RF applications.

This chapter has also focused on studying FSS architectures, including low-pass based unit cells and especially resonant unit cells. The influence of unit cell sizes as well as unit cell substrates on the properties of transmission coefficient, namely zero-transmission coefficient frequency f_z is studied. Figure 3-45 summarizes some unit cell parameters and its influence on f_z, which

is studied in this chapter. Studying these influencing trends will make the design process of unit cells easier.

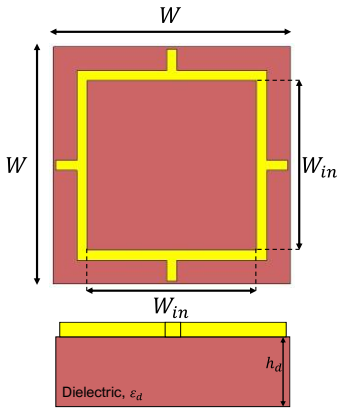

Parameters	W	W_{in}	ε_d	h_d
Dimension change	↑	↑	↑	↑
f_z	↓	↓	↓	↓

Figure 3-45. Summary of unit cell properties influence on zero-transmission frequency

The use of the FSS resonant in combination with diodes has also been discussed in this chapter. It can be seen that the use of a diode is quite useful in electrically controlling the properties of the FSS. The properties of the diode have a significant influence on the properties of the FSS. Table 11 summarizes some factors need to be considered when choosing a diode and the influences of these factors on the FSS properties.

Table 11. Some diode factors and its influence on FSS properties

	Factor	Affection
1	Capacitance	High capacitance increases the difference between f_{z_OFF} and f_{p_ON}
2	Resistance	High resistance reduces FSS transmittance when diode is ON
3	Packaging	Large packaging obstructs the passage of waves while small packaging makes the manufacturing process difficult
4	Price	Should be considered as can be used in large quantities

Chapter 4. 5G Applications Using Paper Substrate

This chapter presents the use of bio-source paper substrate in 5G applications. This substrate offers many advantages, such as environmental friendliness, good recyclability, energy saving for the production process, and flexibility. Therefore, the use of this substrate in 5G applications needs to receive the necessary attention to achieve environmentally sustainable development - an important development in the future. The two presented applications are frequency reconfigurable antennas and FSS (Frequency Selective Surface). Applications are designed at 3.6 GHz.

4.1. Overview

Wireless electronic devices are growing rapidly with an explosion in the number of devices, which will consequently produce a considerable amount of electronic waste. Especially in the context that new generations of electronic devices are coming out quickly to replace the old ones, the life cycle of many devices has been shortened. The increase in the number of electronic devices and their shorter life cycle considerably impact the environment. They become an issue that needs to be considered seriously.

Most electronic devices contain Printed Circuit Boards (PCBs). Conventional PCBs consist of a core dielectric layer with a conductive material on both sides. The core substrate plays an important role, especially in wireless applications, because it dramatically affects the performance of components. Some commonly used substrates are, for instance, FR4, Rogers substrates (RO4003, RO5002, RO6002), or Arlon. These substrates contain ingredients derived from non-renewable resources. For example, Flame Retardant (FR4) consists of three main components: epoxy resin, woven Glass Fiber (GF), and copper foil [96]. Epoxy resin is derived from non-renewable crude oil, while the GF manufacturing process is energy intensive. Different techniques are applied to remove the excess copper layer, such as using chemicals or lasers, to process the copper layer and to print necessary patterns. In general, there is a lot of waste and energy consumption in the fabrication and the use of these substrates. With the explosion of electronic devices, these wastes and environmental impacts have become more noticeable and severe. The development of more environmentally sustainable solutions and designs is required. The bio-based substrates are one of the leading solutions today due to their ability to meet the requirements of embedded electronics, such as flexibility, lightweight, printable, and low cost. The environmental profile of these products can thus be improved by

integrating these concepts of biodegradability and reduction of energy used during the manufacturing process [96].

Studies have been conducted to examine and compare the environmental effects of different PCB manufacturing processes. Ref. [96] studied five different scenarios of PCB fabrication, as listed in Table 12. Results on the impact environment based on ten different criteria of all five scenarios are presented in Figure 4-1. The higher the value, the more negative impact on the environment.

Table 12. Scenarios for PCB production [96]

Scenario	Substrate	Conductive Material
S1	FR4	Etched-Copper
S2	FR4	Ag NPs
S3	PET	Ag NPs
S4	PLA60%-GF40%	Ag NPs
S5	Paper	Ag NPs

(PET: polyethylene terephthalate, PLA: polylactic acid, GF: glass fiber, NPs: nanoparticles)

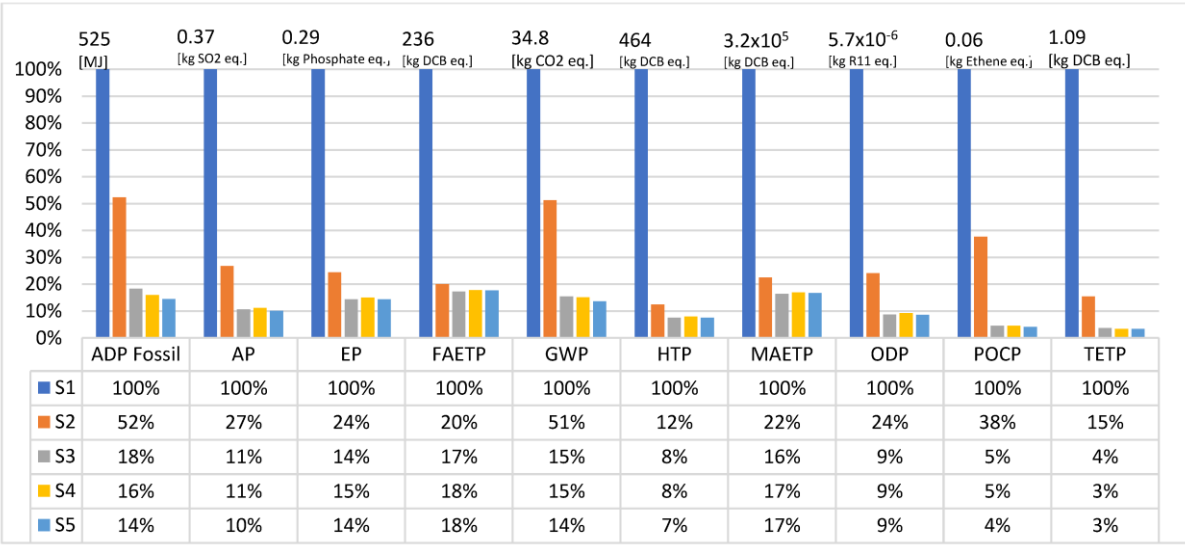

	ADP Fossil	AP	EP	FAETP	GWP	HTP	MAETP	ODP	POCP	TETP
S1	100%	100%	100%	100%	100%	100%	100%	100%	100%	100%
S2	52%	27%	24%	20%	51%	12%	22%	24%	38%	15%
S3	18%	11%	14%	17%	15%	8%	16%	9%	5%	4%
S4	16%	11%	15%	18%	15%	8%	17%	9%	5%	3%
S5	14%	10%	14%	18%	14%	7%	17%	9%	4%	3%

Figure 4-1. Lifecycle comparison of five scenarios [96]

(ADP: Abiotic Deletion Potential, AP: Acidification Potential, EP: Eutrophication Potential, FAETP: Freshwater Aquatic Ecotoxicity Potential, GWP: Global Warming Potential, HTP: Human Toxic Potential, MAETP: Marine Aquatic Ecotoxicity Potential, ODP: Ozone Layer Depletion Potential, POCP: Photochemical Ozone Creation Potential, TETP: Terrestrial Eco-toxicity Potential)

Figure 4-1 shows that using the traditional substrate and conductive material greatly affects the environment, especially when compared with other substrates. By using silver nanoparticles (Ag NPs), these adverse effects have been significantly reduced but are still quite high compared to others. The other three substrates (PET, PLA/GF40, paper) have much less impact on the environment than FR4. Among these three types, it can be said that paper substrate causes the slightest effect.

Applications using substrate paper are being researched and strongly developed thanks to its environmentally friendly nature, biodegrading anility, and high recyclability [97]–[103]. In this chapter, we present two applications in 5G using paper substrate: frequency-reconfigurable antenna and Frequency Selective Surface (FSS).

As mentioned, in the context of the rapid development of new generations which replace older ones more quickly, completely replacing devices suitable for old generations with new devices is impossible in the short term. As a result, the ability to connect at different frequencies to adapt to the wireless generation in use and under development is a highly valued criterion for a wireless system. To meet this need, frequency reconfigurable antennas are presented as a practical solution [102], [104], [105]. By combining active components such as P-I-N diode, users can switch the antenna operating frequency within a pre-designed set of frequencies. In [104], a bow-tie antenna who can be tuned by controlling embedded P-I-N diodes to operate in either 2.2-2.53 GHz, 2.97-3.71 GHz or 4.51-6 GHz frequency bands is presented. A 4-elements frequency reconfigurable multiple input multiple output antenna is designed in [102]. By combining a modified annular slot antenna with varactor diodes in the same FR-4 substrate, the design can operate in three bands: 1.7-2.8 GHz, 2.5-2.85 GHz, and 2.9-3.1 GHz. Ref [105] presents an antenna who can switch between L-band single-frequency and S-band dual-frequency modes. The antenna is constructed from an annular ring and sawtooth on Rogers 5880 substrate and fed by coupling two slots of feed structure on FR4 substrate. However, these examples all use common substrates that are not environmentally friendly. Therefore, we propose using a paper substrate to fabricate a frequency-reconfigurable antenna in this chapter.

Many studies related to paper substrates applications have been developed. Most of them have focused on antennas, while there are other components in the system of wireless devices. The substrate replacement using paper needs to be also studied for other components besides the antenna. So, we can get closer to replacing the entire system with paper substrates. One of the components that is heavily influenced by the substrate and used in many applications is the FSS

(Frequency Selective Surface). With the ability to select frequencies, FSS is very useful in controlling radiated waves. For example, in [100], a single-layer paper substrate-based dual-band FSS for shielding GSM (Global System for Mobile communication) applications is proposed. The FSS consists of modified double square loop elements. It is fabricated and glued into the paper substrate. This FSS offers 18 dB shielding for a bandwidth of 100 MHz for the 930 MHz center frequency, a bandwidth of 173 MHz for the 1720 MHz center frequency and an angular independent operation up to 60°. In [103], a low-cost FSS paper poster consisting of square loop unit cells is fabricated to reduce the drop of 5G signals in the indoor environment by reflecting indoor signals at 25.2 GHz.

FSS has also been presented in Chapter 3 of this thesis. In Chapter 3, despite using jetting technology with Ag NPs, which helps to reduce the impact on the environment, FSS is still printed on acrylic resin substrates. Therefore, in this chapter, we will present the use of paper substrates to fabricate FSS. However, the limitation of the paper substrate is that it is challenging to create a hemispherical form as used in Chapter 3. So, the FSS will be designed on 1D planar surface. In addition, thanks to the paper flexibility, the 1D FSS can also be rolled up to form a cylinder in some applications to suit space and packaging requirements. Diodes are also used to control FSS properties for both vertical and horizontal polarized incident waves.

4.2. Material and Printing Method

The applications presented in this chapter use the paper substrate PowerCoat XD of Arjowiggins company with a thickness of 125 µm. This type of paper is chosen for its high roll-to-roll strength, good sintering capabilities in air thermal, photonic and RF processes, and a thermal stability in color and size. The paper substrate needs to be characterized to simulate in CST Studio Suite. To do that, the resonant cavities, as shown in Figure 4-2, and cavity perturbation techniques were used [106]. First, the transmission coefficient of the resonant cavity is measured. Then, the paper sample will be inserted into the resonant cavity at the slots. The complex permittivity of the sample is extracted from the variation of the transmission coefficient when the sample is inserted into the cavity. This method has the advantage of being simple and saving time. However, with this method, we can only measure results at discrete frequencies. Measured transmission coefficients of the 2480 MHz resonant cavity with and without paper sample are presented in Figure 4-3. Using formulas presented in [106], the paper complex permittivity at 24800 MHz is extracted. The paper has a permittivity of approximately

3.3 and a loss tangent of 0.11 at 2.48 GHz. These parameters are used for simulations at 2.4 GHz and 3.6 GHz.

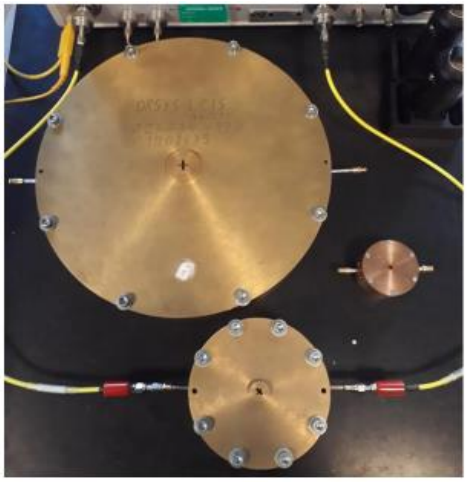

Figure 4-2. Three resonant cavities, from left to right: 930 MHz, 2480 MHz, and 5740 MHz

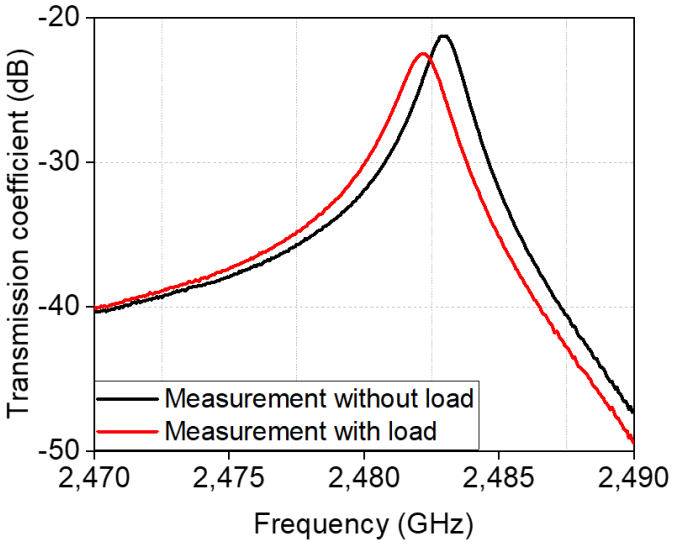

Figure 4-3. Measured transmission coefficient of the 2480 MHz resonant cavity with and without load (paper sample)

Paper antennas or paper microwave structures can be fabricated by printing conductive ink onto the surface of paper substrates. Some popular printing techniques are microcontact printing, ink-jet, screen-printing, and offset-printing [107]. In this thesis, the screen-printing process is chosen due to its simplicity, low cost, and time-saving. The screen-printing principle is presented in Figure 4-4(a). Firstly, the conductive ink is deposited on the screen frame. The screen frame is typically composed of polyester forming a mesh network to control the printed pattern and the amount of conductive ink. For each specific application or pattern, a screen

frame is fabricated. Secondly, an amount of conductive ink is added to the top surface of the screen frame. Then, to print the ink onto the substrate placed below the frame screen, a squeegee is moved over the frame screen surface. With the development of technology, this process is now done by automatic or semi-automatic machines instead of by hand. In our work, we use a the semi-automatic sheet-to-sheet machine Svecia SSM, as shown in Figure 4-4(b). The used conductive ink is silver ink - Henkel ECI 1010. After being printed, the silver ink needs a heat treatment to vaporize the organic compounds present in its formulation. This process helps to establish its electrical conduction properties.

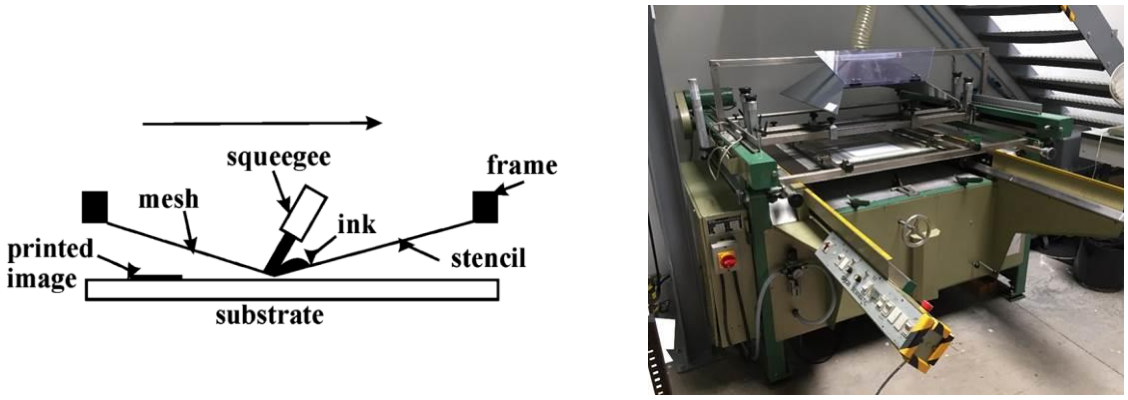

(a) (b)

Figure 4-4. (a) Principle of the screen-printing process [107] (b) Semi-automatic sheet to sheet machine - Svecia SSM

4.3. Frequency Reconfigurable Paper Patch Antenna

4.3.1. Antenna Design

The antenna is designed to operate at the central frequency of 3.6 GHz in the 5G band. The sub-frequency that the antenna can switch to is 2.4 GHz. This is a frequency that is mainly used in Wi-Fi routers.

To operate at these two frequencies, a patch antenna structure was chosen. This structure is simple, easy to fabricate, and stable. Controlling the operating frequency of a patch structure is not too difficult. The operating frequency adjustment can be made by adjusting the patch length. To add an extra operating frequency, an extra patch can be added. By controlling these two patches, we can control the antenna operating frequencies. The geometry of our antenna is presented in Figure 4-5, and antenna parameters are presented in Table 13. The antenna is

designed on one side of the paper. It can be divided into four main parts: coplanar waveguide (CPW) feed, primary patch, supplementary patch, and diode.

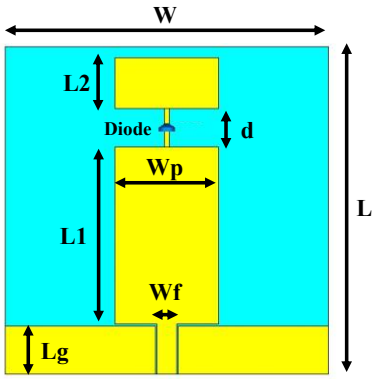

Figure 4-5. Frequency reconfigurable patch antenna geometry

Table 13. Antenna dimensions

Parameters	**L**	**L1**	**L2**	**Lg**	**W**	**Wf**	**Wp**	**d**
Value (mm)	40.3	22.9	6.5	5.2	41.8	2.6	13.4	5

In the feeding section, a CPW structure is selected. In our design, this type of feed is preferred over a classic microstrip feed line for two reasons:

- Using a microstrip feed line would require a bottom ground layer on the other side of the paper, which complicates the printing process. Screen-printing can only print one paper side at a time. If we want to print both sides, we have to print two times. In that case, it is necessary to print correctly so that patterns on both sides does not deviate from each other. It is more complicated than printing on only one side. With CPW, we must print only one paper face.
- The paper we used is relatively thin, with a thickness of 125 µm. The connection to a connector during the measurement is quite complex with this thickness. Using a classic microstrip line with a bottom ground layer will make it more challenging to connect to the connector than when using a coplanar structure.

The antenna primary part is designed to operate at the desired frequency of 3.6 GHz. To switch to 2.4 GHz, a supplementary patch has been added. When two patches are connected, the antenna will radiate at 2.4 GHz. This additional patch is placed far enough away to not have much effect on the primary patch radiation when two patches are not connected.

To electrically control the connection of these two patches, P-I-N diode SMPA1345-040LF presented in Chapter 3 is used. Since the diode is rather small compared to the gap between the two patches, strip conductors are used to connect the diode with both patches. A DC voltage is applied to two pins of the diode through two thin conductors attached directly to the two patches. When the diode is OFF, the second patch is not connected to the primary patch. The antenna resonance frequency is 3.6 GHz. When the diode is turned ON, both patches are connected. As a result, the antenna resonance frequency is changed to 2.4 GHz. To compare and evaluate the diode effect on the frequency reconfiguration ability of the antenna, two test antennas, which are called Test 1 and Test 2, are built as shown in Figure 4-6. These two antennas are designed based on our proposed paper antenna, with the feeding part and the two patches unchanged. Test 1 antenna has no connection between the two patches. It is considered equivalent to the antenna when the diode is OFF, ideally. Test 2 antenna contains a strip conductor to connect the two patches. It is considered as the ideal antenna when the diode is turned ON. Figure 4-7 depicts the simulated resonant frequencies of Test 1 and Test 2 antenna. The simulated radiation patterns of Test 1 and Test 2 antenna are presented in Figure 4-8.

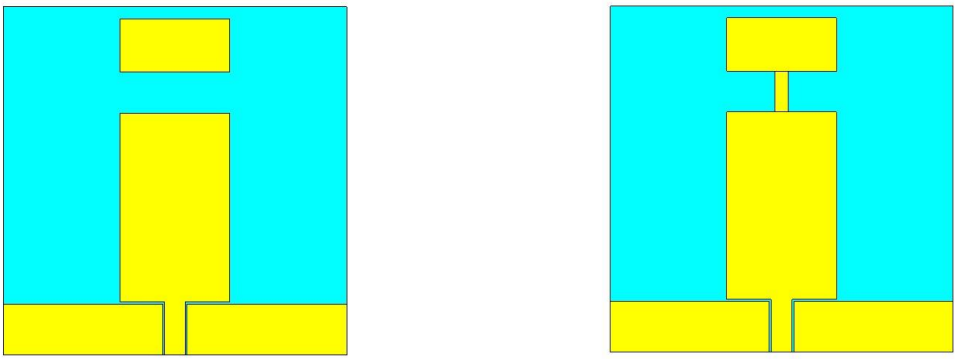

(a) (b)

Figure 4-6. Geometry of (a) Test 1 antenna (b) Test 2 antenna

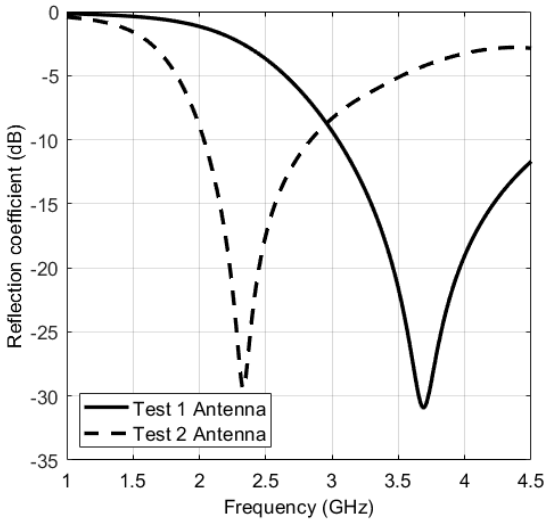

Figure 4-7. Reflection coefficient of Test 1 and Test 2 antenna in simulation

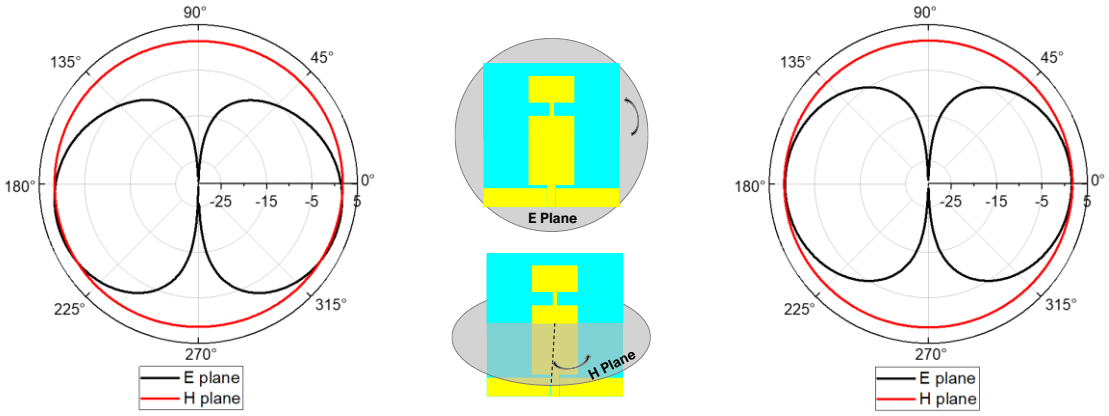

(a) (b)

Figure 4-8. Simulated radiation pattern of (a) Test 1 antenna at 3.6 GHz (b) Test 2 antenna at 2.4 GHz

4.3.2. Antenna Fabrication and Result

Figure 4-9 presents the three fabricated antennas. A DC power supply with a voltage of 0.9 V is applied to turn the diode ON. The (+) of this source is connected to the diode through the conductor wire attached to the secondary patch as shown in Figure 4-9(b). The (-) of the source is connected to the ground of the VNA, so that connected to the diode via the connector. A resistor is connected to the (+) conductor wire to protect the diode.

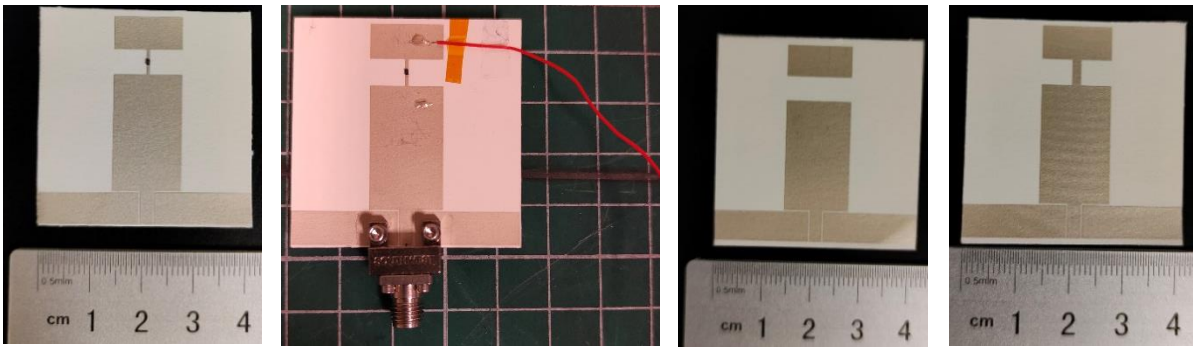

(a) (b) (c) (d)

Figure 4-9. (a) Fabricated proposed patch antenna (b) Configuration of proposed antenna for measurement (c) Fabricated Test 1 antenna (c) Fabricated Test 2 antenna

Measured reflection coefficients of three antennas are presented in Figure 4-10. When the diode is OFF, the proposed antenna resonant frequency is 3.6 GHz, similar to the resonant frequency of Test 1 antenna. When the diode is ON, the proposed antenna resonant frequency is 2.4 GHz, similar to the resonant frequency of Test 2 antenna.

In the measurement results, there exists noises affecting the antenna. These noises are predicted to come from the conductor wire of diode, the resistor and the connector K. Observations during the measurement show that the change in length and shape of the conductor wire changes the noise on the antenna reflection coefficient. To improve this, filters may be used to connect to the conductor wire. However, this proposal needs to be tested experimentally in the future. There is a difference in noise when using resistors and without resistors, and a slight difference when changing resistor values. The third source of noise can come from connector K. We can see that this connecter is massive and close to the antenna patch. So, it may affect the antenna. We tried another type of connector. Since the paper antenna has a thin structure, we used a combination of a SMA connector and a pressure-hold system to connect to the antenna without damaging the antenna structure. However, this structure is also relatively bulky and affects the antenna. It is possible that smaller connectors, which can connect without soldering to the antenna, can help minimize the connector effect on the antenna.

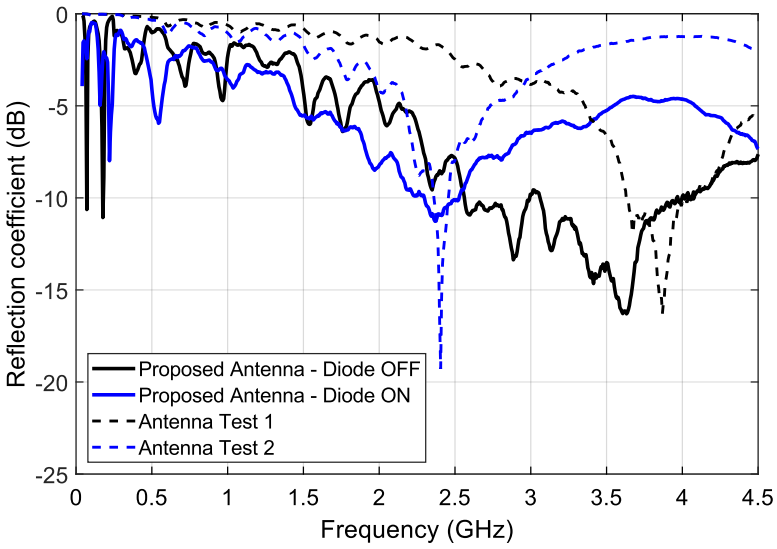

Figure 4-10. Measured reflection coefficient of proposed antenna, Test 1 and Test 2 antenna

The gains of the three antennas are measured and. Test 1 antenna achieves a gain of 4.4 dBi at its 3.6 GHz resonant frequency. The Test 2 antenna reaches a gain of 3.6 dBi at its 2.4 GHz resonant frequency. With the proposed antenna, when the diode is OFF, its gain is 1.1 dBi at 3.6 GHz. When the diode is ON, the gain at 2.4 GHz reaches a value of 3.4 dBi. The measured antenna radiation pattern in H-plane at 3.6 GHz and 2.4 GHz of the proposed antenna is presented in Figure 4-11. Comparison of antenna radiation pattern in H-plane between the proposed antenna in diode OFF state and Test 1 antenna at 3.6 GHz is presented in Figure 4-12(a). There is a general similarity of radiation in two cases, but we can also see that the diode and its power supply system have certain effects on the antenna radiation pattern. This conclusion is also similar when comparing the radiation pattern of proposed antenna when diode is ON and Test 2 antenna at 2.4 GHz as shown in Figure 4-12(b).

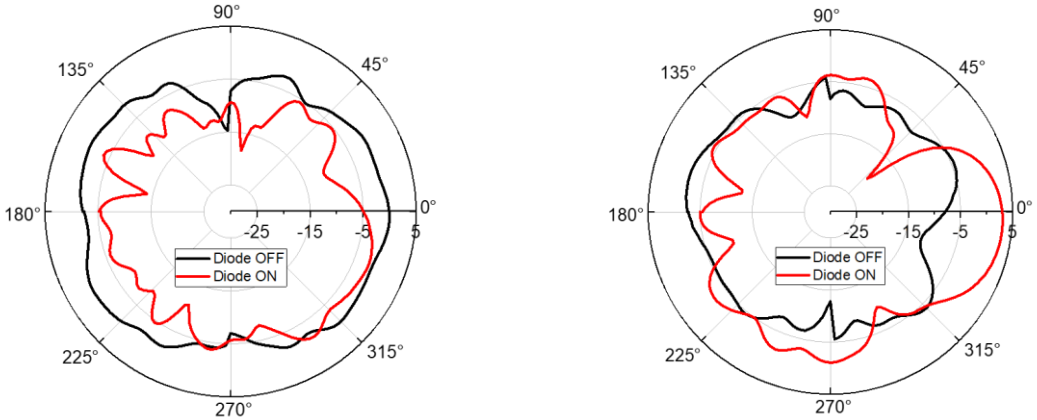

(a) (b)

Figure 4-11. Measured antenna radiation pattern in H-plane at (a) 3.6 GHz (b) 2.4 GHz

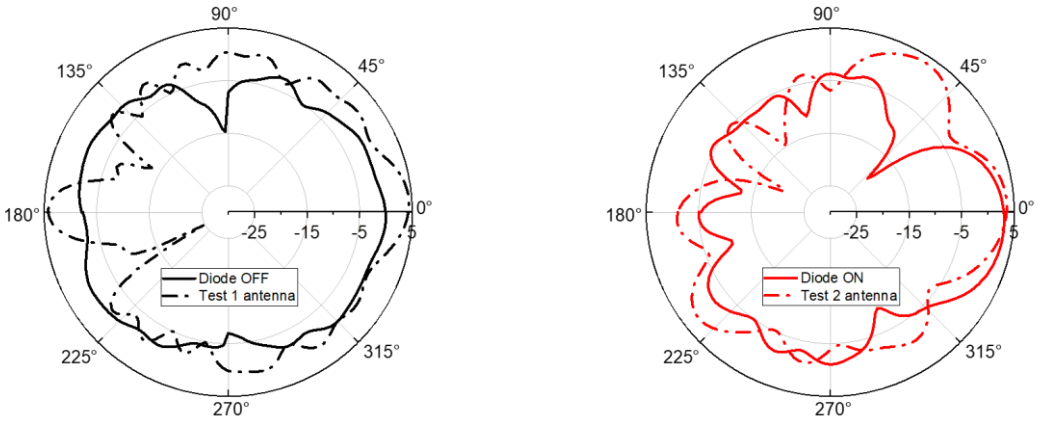

(a) (b)

Figure 4-12. Radiation pattern in H-plane Comparison between (a) Proposed antenna when the diode is off and Test 1 antenna at 3.6 GHz (b) Proposed antenna when diode is on and Test 2 antenna at 2.4 GHz

4.4. Paper Frequency Selective Surface

4.4.1. Frequency Selective Surface (FSS) Unit Cell Design

The FSS unit cell is designed with a central frequency of 3.6 GHz. The substrate used is the same as in section *4.2* - paper PowerCoat XD with a permittivity of 3.3, a loss tangent of 0.11 and a thickness of 0.125 mm. The unit cell structure is based on the resonant band stop structure as presented in Chapter 3. The resonant band stop FSS was chosen instead of the low pass FSS because the low pass FSS has less parameters to control S-parameters than the band stop FSS. In other words, the band stop structure is more flexible than the low pass. The desired features of the unit cell in this section are:

(1) When diodes are present, the FSS must be capable of performing one of the following four states:
   (S1) – Reflect both vertical and horizontal polarized incident waves at 3.6 GHz.
   (S2) – Allow both vertical and horizontal polarized incident waves at 3.6 GHz passing.
   (S3) – Reflect only 3.6 GHz vertical polarized incident waves.
   (S4) – Reflect only 3.6 GHz horizontal polarized incident waves.

(2) When diodes are ON: At 3.6 GHz, the transmission coefficient (S_{21}) must be high (>-3dB) and the reflection coefficient (S_{11}) must be low (<-10dB). This ensures that 3.6 GHz waves are well transmitted and not reflected due to impedance mismatch.

(3) When diodes are OFF: At 3.6 GHz, the transmission coefficient (S_{21}) must be low (<-10dB). This ensures that most 3.6 GHz waves are reflected.

Feature (1) requires the ability to independently control vertical diodes and horizontal diodes. If vertical diodes and horizontal diodes are connected on the same unit cells, it is difficult to monitor them independently. The reason is that, powering the vertical diodes may also unintentionally power the horizontal diodes and vice versa. In Chapter 3, we can print FSS only on the outside surface of the radome. Thus, diodes of the FSS in Chapter 3 are mounted in one direction. To solve the problem, in this chapter, we propose printing FSS unit cells on both sides of the paper. With screen-printing technology, printing on both sides of the paper substrate is possible. Diodes will be mounted in vertical lines (columns) on one paper side and in horizontal lines (rows) on the other side.

Feature (2) and (3) will be satisfied by modifying the unit cell parameters. The general geometry of the FSS unit cell is illustrated in Figure 4-13. The structure of the top and bottom layers is identical, except for the position of the strip conductors used to connect diodes. To construct unit cells, we have to determine values for five parameters: W, W_{in}, d, p, t.

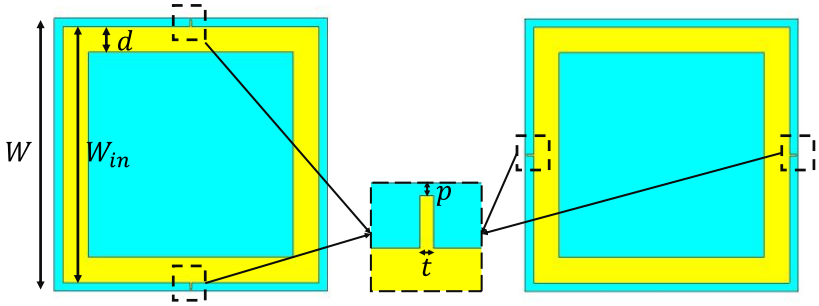

Figure 4-13. Geometry of FSS unit cell on paper, top layer (left) and bottom layer (right)

Figure 4-14 describes the ideal S-parameters of the desired FSS unit cell to satisfy the feature (2) and (3). It is possible to use the studies obtained in Chapter 3 during the design process. The summary of some studies about resonant FSS unit cell in Chapter 3 is presented in Figure 4-15.

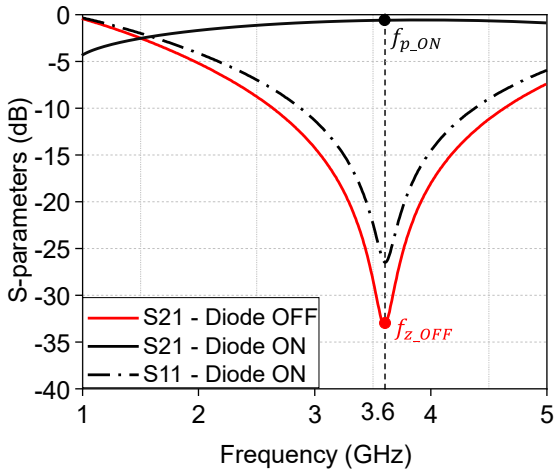

Figure 4-14. Ideal S-parameters of desired FSS unit cell

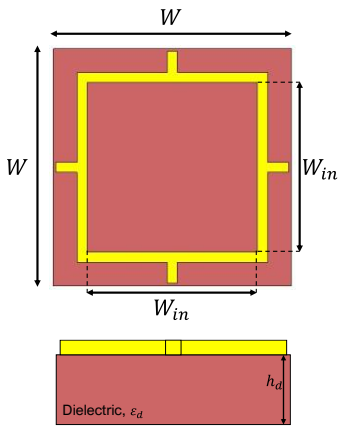

(a)

Parameters	Trend	f_z
W	↑	↓
W_{in}	↑	↓
ε_d	↑	↓
h_d	↑	↓

$$f_{z\_OFF} = \frac{1}{2\pi\sqrt{L(C+C_1)}};\ f_{p\_ON} = \frac{1}{2\pi\sqrt{LC}}$$

(b)

Figure 4-15. Summary of some studies about resonant FSS unit cell in Chapter 3
(a) Resonant FSS unit cell in Chapter 3 (b) Several factors affect unit cell properties

❖ *Determine p and t*

To satisfy feature (2) and (3), unit cell needs to have a zero-transmission frequency, in diode OFF state (f_{z_OFF}), close to a passband frequency, in diode ON state (f_{p_ON}), and close to 3.6 GHz ($f_{z\_OFF} \approx f_{p\_ON} \approx 3.6$ GHz). From Figure 4-15(b), we can see that, reducing C_1 can reduce the difference between f_{z_OFF} and f_{p_ON}. C_1 can be adjusted through p and t (Figure 4-13). Increasing p and reducing t can reduce C_1. To ensure a suitable distance to mount diodes to the circuit, p is fixed at 0.2 mm. The minimum value of t is set to the diode pin width, which is 0.5 mm. After this first step, two values are fixed: p = 0.2 mm and t = 0.5 mm. In the next steps, we need to determine W, W_{in} and d.

❖ *Determine W, W_{in}*

In the second step, the feature (2) is selected for analysis. This feature requires that, the transmission coefficient (S_{21}) must be high (> -3dB) and the reflection coefficient (S_{11}) must be low (< -10dB) at 3.6 GHz, when diodes are ON. When diodes are ON, assume that the passband frequency of S_{21}, which is also the resonant frequency of S_{11}, is f_{res_ON}. The second feature is chosen to analysis because d has almost no effect on the value of f_{res_ON}. Therefore, to satisfy feature (2), it is sufficient to control two parameters W and W_{in} instead of all three parameters (W, W_{in}, d). It is easier for the design process.

To determine W and W_{in}, we can start from parameter values of 1D FSS on RO4003C in Chapter 3. The difference between FSS in Chapter 3 and Chapter 4 is the substrate (the permittivity (ε) and the thickness). If all the dimensions of unit cell in the two chapters are the same, we have:

$$\left.\begin{array}{c}\left\langle\begin{array}{l}Chapter\ 3: \varepsilon_{|Ch3} = 3.55; h_{|Ch3} = 1.524\ mm \\ Chapter\ 4: \varepsilon_{|Ch4} = 3.3; h_{|Ch4} = 0.125\ mm\end{array}\right. \\ From\ Chapter\ 3: \begin{cases}\varepsilon \downarrow \rightarrow f \uparrow \\ h \downarrow \rightarrow f \uparrow\end{cases}\end{array}\right\} \rightarrow f_{p\_ON|ch3} < f_{p\_ON|ch4}$$

In other words, if we used W and W_{in} as in Chapter 3, the passband frequency, when diodes are ON, is greater than 3.6 GHz. To decrease and bring the frequency to 3.6 GHz, W and W_{in} have to be changed. From Chapter 3, we also know that:

- If W increases, f_{p_ON} is decreased.
- If W_{in} decreases (while keeping W unchanged), f_{p_ON} is increased.

Therefore, to ensure that the f_{p_ON} frequency decreases, W and W_{in} in this chapter must increase compared to Chapter 3.

To save space for a unit cell, W_{in} should be close to the value of W. It is because the smaller W_{in}, the more W has to increase the value to decrease f_{p_ON}, so the unit cell becomes bulkier. To ensure that strip conductors to mount diodes are not too short, the value ($W - W_{in}$) is fixed at 3 mm. Therefore, f_{res_ON} is controlled by W.

In this step, to run the simulations, d is temporarily fixed at 0.8 mm as in Chapter 3. Through simulation, we found that at W = 33 mm, the unit cell can satisfy the feature (2) by providing a low S_{11} and a high S_{21} when diodes are ON as shown in Figure 4-16. In conclusion, after the second analysis step, two new values are determined: W = 33 mm, W_{in} = 30 mm.

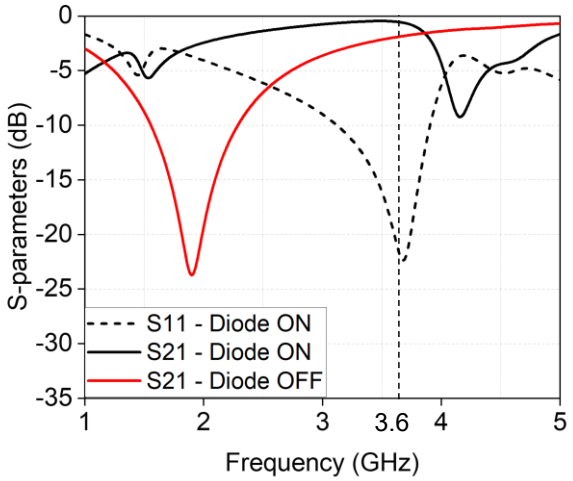

Figure 4-16. S-parameters of FSS unit cell with W = 33 mm, W_{in} = 30 mm, d = 0.8 mm

❖ *Determine d*

From Figure 4-16, we can see that the zero-transmission frequency when diodes are OFF (f_{z_OFF}) is approximately 1.9 GHz. This value is far from 3.6 GHz. Transmission coefficient S_{21} at 3.6 GHz is high. It means that the feature (3), which requires a low S_{21} (S_{21}<-10) at 3.6 GHz when diodes are OFF, is not satisfied if d = 0.8 mm. Although changing d does not change f_{res_ON}, it can change f_{z_OFF}. Therefore, to satisfy condition (3), we simply need to change the value of d, so that f_{z_OFF} approaches 3.6 GHz. Figure 4-17 illustrates that increasing d increases the value of f_{z_OFF}. At d = 6 mm, $f_{z\_OFF} \approx 3.6\ GHz$.

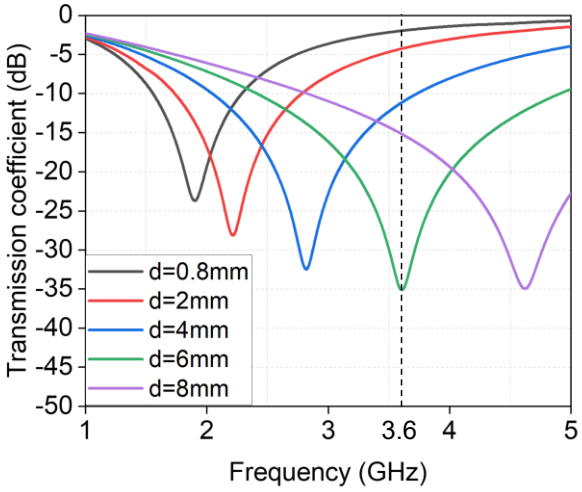

Figure 4-17. Unit cell transmission coefficient with difference values of d, diodes are OFF

In conclusion, the dimensions of FSS unit cell are presented in Table 14. Figure 4-18(a) shows the simulated S-parameters of FSS unit cell when all diodes are ON and when all diodes are OFF. Figure 4-18(b) presents simulated S-parameters of unit cell when the diodes are only ON

in one direction, in this case – vertical direction. In other words, only the diodes on one side of paper substrate are ON while the diodes in the other side are OFF. We can see that, when only vertical diodes are ON, FSS unit cells allow vertical electric field component to pass through while blocking horizontal electric field component. The opposite functioning is observed when only horizontal diodes are activated: FSS unit cells allow horizontal electric field component to pass through while blocking vertical electric field component. We can say that all 3 requirements for FSS unit cell have been met.

Table 14. Dimension of FSS unit cell

Parameters	W	W_{in}	d	t	p
Value (mm)	33	30	6	0.4	0.2

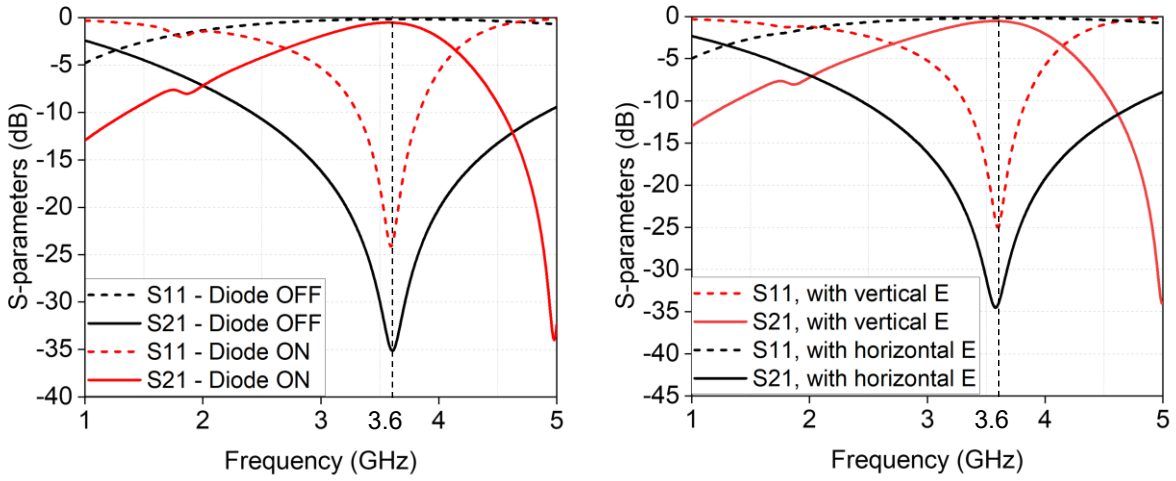

(a) (b)

Figure 4-18. Simulated S-parameter of FSS unit cell final design(a) When all diodes have the same state (on or off) (b) When all vertical diodes are on while all horizontal diodes are off, the incident waves have vertical polarization

4.4.2. FSS Fabrication and Experiment

Figure 4-19 presents the FSS printed using the screen-printing method. The FSS transmission coefficient will be verified with measurements. For technical reasons, diode installation in the FSS is still in progress. Therefore, experiments are first performed on the FSS paper without diodes.

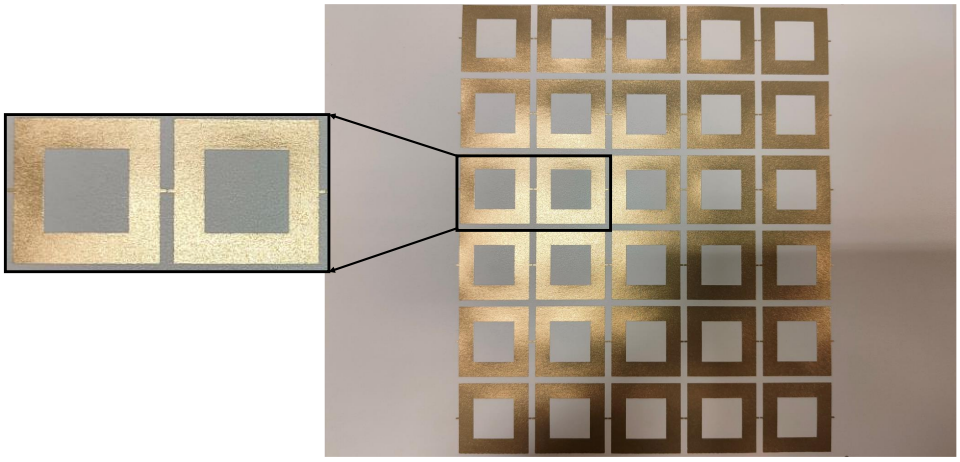

(a)

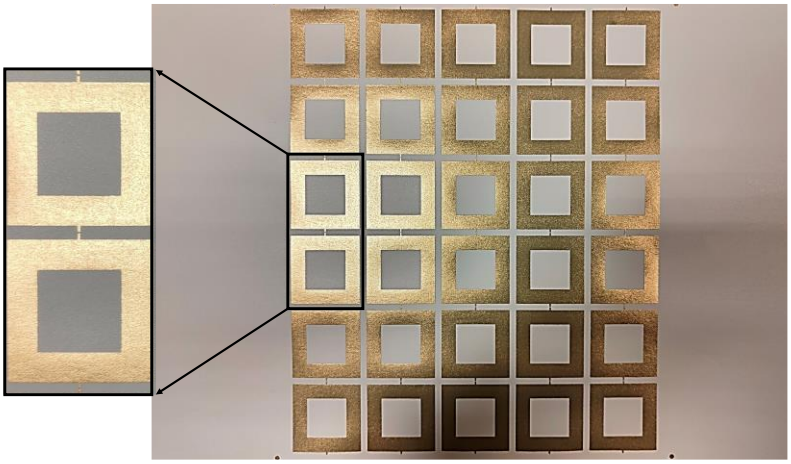

(b)

Figure 4-19. Fabricated paper FSS (a) Top (b) Bottom

The FSS transmission coefficient is measured using the configuration as in Chapter 3, which is used to measure the 1D planar FSS on RO4003C. This configuration consists of two antennas facing each other: a transmit antenna (Tx) and a receive antenna (Rx). First, the transmission coefficient of the Tx-Rx system in air is measured ($S_{21|Ref}$). The FSS is then attached to the window on the communication line between Tx and Rx. The transmission coefficient of the Tx-Rx system with the FSS is measured ($S_{21|Sys}$). Finally, the FSS transmission coefficient is calculated as ($S_{21|Sys}$- $S_{21|Ref}$). This measurement system was developed by A. Niembro-Martin et al. as presented in [108].

To become equivalent to the diode ON state, two strip conductors located between two adjacent unit cells are connected using conductive glue. While with the diode OFF state, the structure of unit cells is kept unchanged (strip conductors disconnected). Although considered equivalent, not using diodes will lose the contribution of capacitance, inductance, and resistance of diodes

to the FSS. Thus, zero-transmission frequencies will increase compared to when using diodes. In other words, the transmission coefficient value curve will be shifted to the right, similar to the analysis of 1D FSS in Chapter 3.

To simulate diode state control, four paper FSS sheets with the following configurations are used, as illustrated in Figure 4-20:

- FSS n°1: Equivalent to “All diodes are ON”, all strip conductors are connected.
- FSS n°2: Equivalent to “Only horizontal diodes are ON”, only horizontal strip conductors, which are in the FSS top face, are connected.
- FSS n°3: Equivalent to “Only vertical diodes are ON”, only vertical strip conductors, which are in the FSS bottom face, are connected.
- FSS n°4: Equivalent to “All diodes are OFF”, all strip conductors are disconnected.

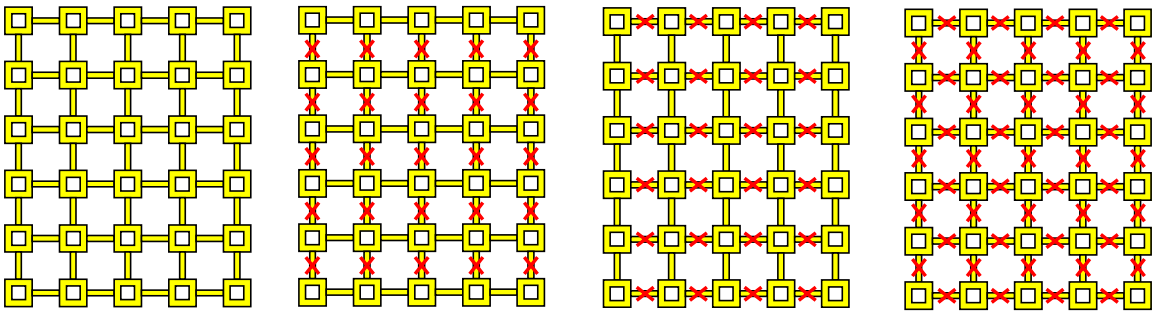

(a) (b) (c) (d)

Figure 4-20. Four FSS versions (a) FSS n°1: All strip conductors are connected
(b) FSS n°2: Only horizontal strip conductors are connected
(c) FSS n°3: Only vertical strip conductors are connected
(d) FSS n°4: All strip conductors are disconnected

To verify the response of FSSs to different incident waves, four scenarios with different incident waves polarizations, as shown in Figure 4-21, will be measured:

- Scenario 1 (S1): Rx and Tx have vertical polarizations.
- Scenario 2 (S2): Rx and Tx have horizontal polarizations.
- Scenario 3 (S3): Rx has vertical polarization; Tx has 45° diagonal polarization.
- Scenario 4 (S4): Rx and Tx have 45° diagonal polarizations.

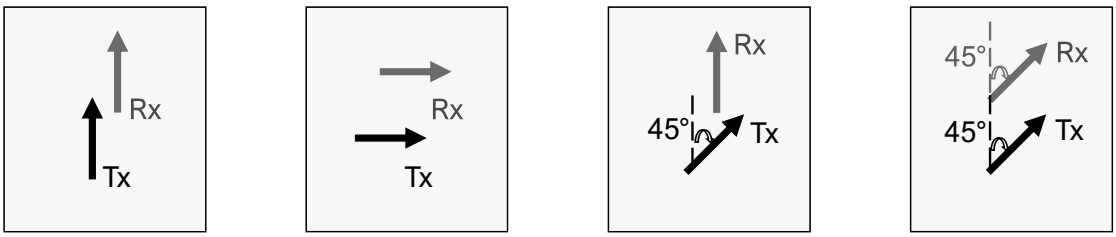

(a) (b) (c) (d)

Figure 4-21. (a) Scenario 1 (S1): Rx and Tx have vertical polarizations
(b) Scenario 2 (S2): Rx and Tx have horizontal polarizations
(c) Scenario 3 (S3): Rx has vertical polarization; Tx has 45° diagonal polarization
(d) Scenario 4 (S4): Rx and Tx have 45° diagonal polarization

Measured results of the four FSSs in the four scenarios are shown in Figure 4-22.

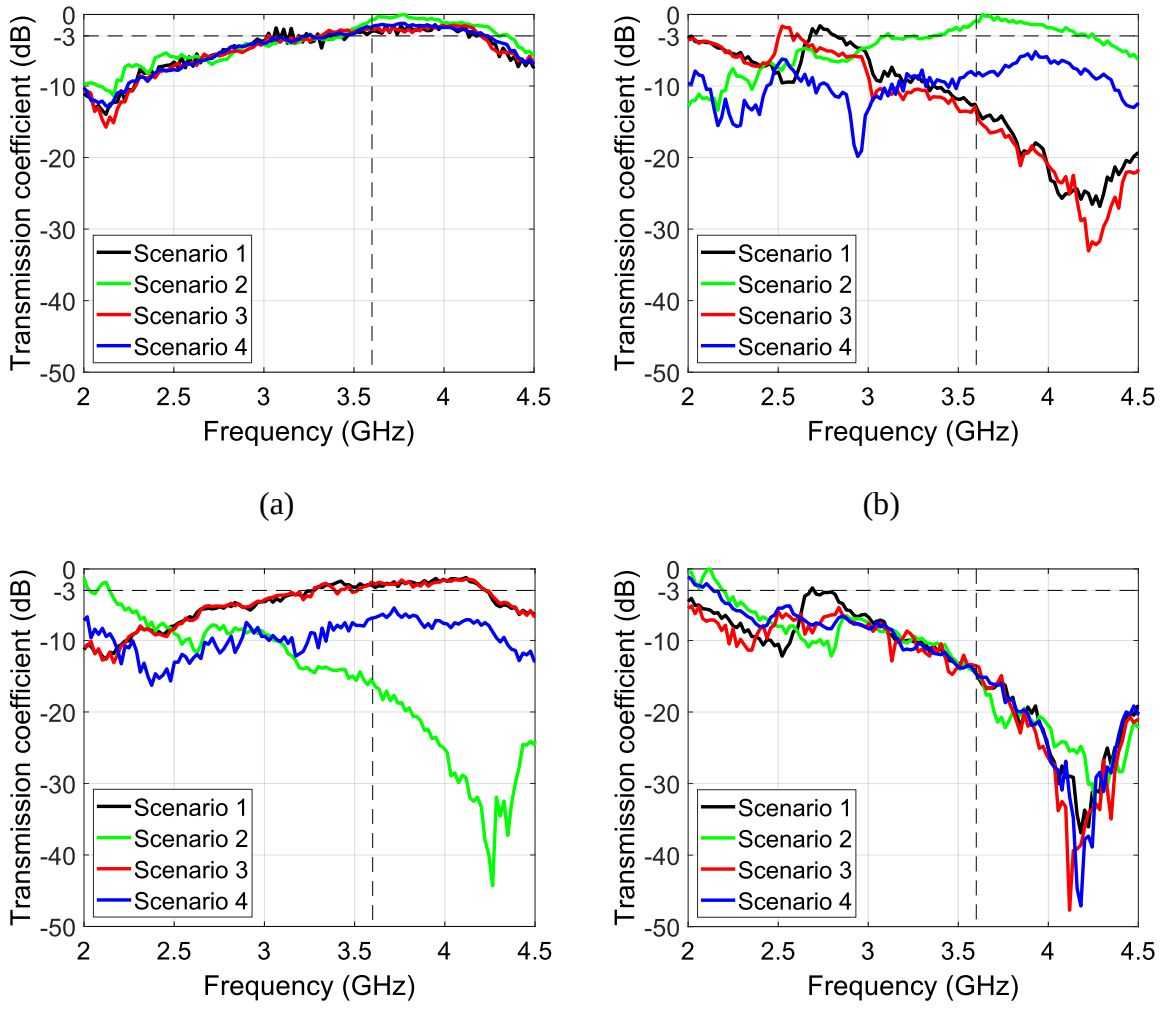

(a) (b)

(c) (d)

Figure 4-22. Measured transmission coefficient in four planned scenarios of (a) FSS n°1
(b) FSS n°2 (c) FSS n°3 (d) FSS n°4

From the measurement results, we have some discussions for each scenario.

With the scenario 1 (black lines), where Tx and Rx have the vertical polarizations. It means that the transmission coefficient is high only if we use FSSs which have vertically connected unit cells to allows vertical polarization incident waves to pass through. At 3.6 GHz:

- S_{21} of FSS n°1 and FSS n°3 are high because they have vertically connected unit cells.
- S_{21} of FSS n°2 and FSS n°4 are low because they have no vertically connected unit cells.

With the scenario 2 (green lines), where Tx and Rx have the horizontal polarizations. It means that the transmission coefficient is high only if we use FSSs which have horizontally connected unit cells to allows horizontal polarization incident waves to pass through. At 3.6 GHz:

- S_{21} of FSS n°1 and FSS n°2 are high because they have horizontally connected unit cells.
- S_{21} of FSS n°3 and FSS n°4 are low because they have no horizontally connected unit cells.

With the scenario 3 (red lines), where Tx has 45° diagonal polarization while Rx has vertical polarization. A diagonal polarization can be decomposed into the sum of vertical and horizontal polarization. At 3.6 GHz, we see that:

- S_{21} of FSS n°1 is high because FSS n°1 allows both elements (vertical and horizontal) of polarization to pass through. Then Rx receives the vertical element as it did with Tx when there is no FSS.
- S_{21} of FSS n°2 is low because FSS n°2 allows only horizontal element to pass through. It means that diagonal polarization waves become horizontal polarized waves after passing though FSS n°2. However, Rx receives only vertical polarization. Thus, S_{21} of FSS n°2 is low.
- S_{21} of FSS n°3 is high because FSS 3 allows vertical element to pass through. And this vertical element is received by Rx which has a vertical polarization. Thus, S_{21} of FSS n°3 is high.
- S_{21} of FSS n°4 is low because FSS n°4 does not allow any polarization to pass through.

With the scenario 4 (blue lines), where Tx and Rx both have 45° diagonal polarization. The diagonal polarization can be decomposed into the sum of vertical and horizontal polarization. At 3.6 GHz, we see that:

- S_{21} of FSS n°1 is high because FSS n°1 allows both elements (vertical and horizontal) of polarization to pass through. Then Rx receives both elements as it did with Tx when there is no FSS.
- S_{21} of FSS n°4 is low because FSS n°4 does not allow any polarization to pass through.
- S_{21} of FSS n°2 and FSS n°3 is lower than S_{21} of FSS n°1 but higher than FSS n°4 because they allow either horizontal or vertical polarization to pass through. And because Rx has a 45° diagonal polarization, it can receive a portion, but not the whole wave after passing through the FSS. Thus, the S_{21} in these two cases is a bit low.

4.5. Chapter Conclusion

In this chapter, we present the application of bio-source paper substrate in 5G applications. Two applications are performed: frequency reconfigurable paper antenna and paper Frequency Selective Surface (FSS). The frequency reconfigurable paper antenna works at 2.4 GHz and 3.6 GHz. By controlling a P-I-N in the structure, the antenna can switch between these two frequencies. The second application presents a FSS structure which is printed on both sides of paper substrate. By connecting unit cells on both paper sides in different directions, the FSS can act as a polarization filter. Initial measurement results show that this idea is quite promising. In the next step, FSS properties can be controlled electrically by using diodes in the structure.

When working with paper substrates, we found some weak points of this paper substrate. The dielectric loss of paper is relatively high compared to traditional dielectric substrate. Processing at very high temperatures, such as soldering tin, on a paper substrate can destroy the paper structure. In addition, the flexible property sometimes causes some difficulties such as distortion of the antenna radiation properties. However, paper is still a promising substrate to replace traditional substrates to reduce environmental impacts. This substrate offers numerous advantages, such as environment friendly, good recyclability, energy saving for the production process, and flexibility. In addition, the small thickness of the used paper can help to minimize wave deflection of passing waves in structures like FSS. Research to overcome the weaknesses of paper substrates is also being widely developed. Widespread adoption of paper substrates to replace traditional substrates is a possible scenario in the future.

General Conclusion and Future Work

This thesis contributes to the development of methods to improve the loss problem in 5G by developing methods to increase the antenna gain and printed radomes to construct steerable antenna-radome systems. The thesis also contributes to the development of sustainable microwave electronics by developing RF components using paper substrate.

Chapter 1 presents an overview of 5G FWA development, advantages and remaining issues in the development of this technology. 5G FWA is predicted to reach approximately 110 million connections by 2027 according to Ericsson study. The frequency bands used for 5G in France include the 3.4-3.8 GHz band, the frequencies of previous generations (2G, 3G, 4G) and the 26 GHz band. It is expected to provide high speed transmissions, low latency, high capacity and flexible network. Despite its great potential, to make the most out of it, 5G FWA still needs to solve one of its biggest challenges, high losses. These losses can come from different sources, such as path loss, non-ideal FWA Line of Sight (LoS), penetration loss through buildings and by plants. To clarify and find solutions to improve this challenge, numerous studies on 5G have been done. The research focuses on a number of key issues such as loss measurement and prediction model, factors affecting losses and solutions to improve the loss problem. In general, solutions can be divided into three main groups: using high gain antennas, using steerable antennas, and improving building material. In this thesis, we focus on studying about using high gain antennas, through the development of high gain Vivaldi antenna, and beamforming techniques, through the design of printed radomes.

Chapter 2 presents in detail two methods to increase the gain of a Vivaldi antenna while keeping its planar and compact structure. Vivaldi antennas in this chapter work in the K_a-band (26-40 GHz). The first method is based on the substrate lens and flared quasi-SIW (Substrate Integrated Waveguide) structure. The flared quasi-SIW is inspired by the E-plane rectangular horn antenna structure. The flared horn acts as transitions from waveguide mode to free-space mode to reduce the reflected waves and emphasize the transmitted waves. The use of quasi-SIW structure helps to integrate the flare structure into the antenna to retain the antenna planar property. In quasi-SIW, two metallic rows are not connected by the metallic layers on the top and bottom of the substrate as in a normal SIW. This allows reducing reflections of antenna radiation waves. The substrate lens is used to focus and orient wave, thus increasing the antenna gain. The second method presented in this chapter is based on PCL (Phase Compensation Lens). This approach has been used in several studies. However, according to our observations, the

PCL design process and its disadvantages are generally not clearly presented. Therefore, we propose a four-step design process leveraging popular software such as CST Studio and MATLAB to design the PCL. The aim of PCL is to convert the cylindrical phase of incoming wavefront to quasi-in-phase for outgoing wavefront. By doing this way, we can achieve a higher gain. Most of these lenses are based on generating different phase velocities (in average) at different locations to correct the phase of the wave as it passes through. To maintain the antenna planar property, planar PCL structure, constructed by using microstrip unit cells to correct phase error, is used in the works reported in this manuscript. Our PCL lens is constructed by following four design steps. Antennas of the two methods are fabricated and measured. In the first method, the antenna volume is increased by 42 % compared to the original antenna, and the gain is improved up to 7.5 dBi. While, in the second method, with an increase of about 6 % in volume, the antenna gain increases by about 1.5 dB. We can see that each method has strong and weak points. The first method brings a good gain improvement, but it increases the antenna size and may increase the fabrication complexity due to the use of quasi-SIW. The second method provides a gain improvement of only 1.5 dB but it does not make the antenna bulkier or more complex.

Chapter 3 presents radome designs to improve antenna functionality by using 3D printing technology to print different metallic and conductive structures on existing dome surfaces. By doing this way, the radome will help protect and improve the functions of the antenna at the 3.6 GHz center frequency. Usually, the main function of a radome is to protect the antenna. This is relatively wasteful because radomes occupy a large area while providing only one effect. The ideas for making printed radomes to improve antenna functionality were developed, to enhance the usefulness of this protection. Currently, the 3D functionalized radomes are usually realized by three different techniques including origami, printed mask and engraving. However, these methods have certain disadvantages and limitations. In this thesis, 3D jetting piezoelectric technology, which is currently developed in the MINT project under the cooperation of Schneider Electric, LGP2 - Grenoble INP Pagora and IMEP-LaHC - Grenoble INP Phelma. By using a printhead mounted on a 6-axes robot, the system allows printing at any point in space. This method allows direct printing without contact on the radome surface. Three patterns were printed on the acrylic dome surface. The first pattern is a simple conductive ring. It acts as a reflector which redirects the secondary beam towards the main beam, thus improving the antenna main beam. A 3.6 GHz ring patch antenna was also fabricated to verify the capabilities of the printed radome. The measurement shows that the printed radome helps to conform the

antenna radiation and improve the gain in a specific direction by 2 dB. The second printed pattern is a FSS low pass-based model. The pattern divides the radome into two halves: half (I), consisting of transmission unit cells (UC1) and half (II) consisting of reflection unit cells (UC2). In other words, the radome has one half which is transparent to radiated waves at 3.6 GHz and the other half prevents 3.6 GHz radiated waves from passing through. Consequently, the antenna radiation waves are deflected to the first radome half after passing through printed radome. A 3.6 GHz rectangular patch was fabricated to verify the printed radome properties. The measurement shows that the antenna main radiation direction has been adjusted to approximately 30 degrees towards the transmission half as expected. However, unit cells used in this low pass are full rectangles, which may cause some difficulties and undesirable phenomena (ink flow) in manufacturing. Therefore, the third pattern, which is based on FSS resonant band stop with rectangular ring unit cells, is developed. This pattern helps to reduce the ink flow in manufacturing. In addition, the use of diodes to control electrically the properties of FSS is also studied. Resonant band stop FSS with diode on planar RO4003C substrate was fabricated and measured. There is a coherence between the measurement and simulation results. When diodes are OFF, the planar FSS reflects the radiated wave at 3.6 GHz. When diodes are ON, the planar FSS allows the wave at 3.6GHz to pass through. With the hemispherical radome, the FSS printing process to the radome surface was done. However, due to some technical reasons, the process of mounting the diode on the radome and the measurement process have not been completed yet.

The final chapter, Chapter 4, presents an approach to sustainable microwave electronics by developing RF components using paper substrate. According to some studies, the use of paper substrates will help reduce the impact on the environment compared to common substrates such as FR-4, Rogers substrates. Therefore, the development of applications based on paper substrates should be considered. In this chapter, we present the application of paper substrate (PowerCoat XD) to fabricate frequency reconfigurable antenna and FSS at 3.6 GHz. In the first application, the antenna can change the operating frequency between 2.4 GHz and 3.6 GHz by controlling a P-I-N diode in the design. However, the measurement also shows that the paper antenna is also affected easily by many environmental influences. In general, paper substrates are commonly used in antenna applications. To study the applicability of paper substrates for other RF components, we fabricated paper FSS. Diodes are also combined in this design. By controlling diodes, the FSS properties are controlled. By printing the FSS and controlling the diode differently on two paper sides, the FSS can act as a polarization filter. Initial

measurements of printed FSSs, without diode, with four different configurations were done. The different responses of the FSSs to different polarizations of the incident wave were as expected. Mounting the diodes on the FSS paper is in progress.

In the limited duration of the thesis, some ideas have not yet been implemented or completed. Follows are some plans to continue to complete and develop some ideas in the future.

1. *FSS printed radome*

In this thesis, the fabrication of printed radome based on resonant band-stop FSS combined with diodes has not finished yet. Fabrication and measurement will be completed in the future.

In addition, the study on the effects of the curved FSS surface on different incident waves also needs to be investigated.

2. *Printed diode on paper*

With the aim of constructing sustainable and ecological components, we tried to optimize and manufacture RF components on paper. However, to reconfigure antennas or FSS, we still need prefabricated diodes, which is not very environmentally sustainable. We therefore want to find an alternative diode to replace this packaged diode. The alternative diode will be produced by printing it directly onto the paper using screen-printing technique. This not only makes the antenna eco-friendly, but also makes the antenna structure simple and compact. A proposed structure of the reconfigurable antenna using a printed diode is shown in Figure 1. This printed diode will be based on the structure of an electrochromic (EC) material. This structure is still being developed.

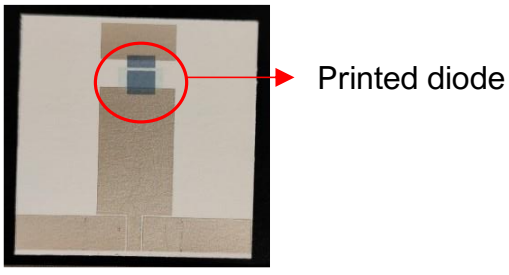

Figure 1. Example of antenna with printed diode test

3. *Printed FSS on paper*

With the paper FSS in Chapter 4, the process of mounting diodes on the circuit is still in progress. The measurement after the fabrication will be carried out in the future. With the measurement process, transmission coefficient of FSSs is measured. In addition, we plan to verify the FSS characteristics through the radiation pattern measurement, by using a circular

polarization antenna. The geometry and simulated cross-polarization, co-polarization of the antenna is presented in Figure 2.

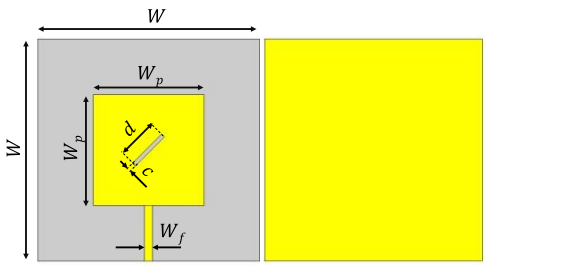

Parameters	W	W_p	W_f	d	c
Value (mm)	41.2	20.6	1.5	7.57	0.76

(a)

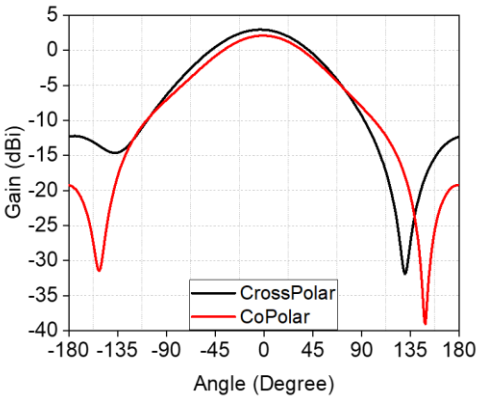

(b)

Figure 2. (a) Greometry of the nearly circular polarization antenna (b) Simulated cross-polarization and co-polarization of the antenna, in Ludwig-3 coordinate system

The test plan will include 4 scenarios: (S1) All diodes are OFF, (S2) All diodes are ON, (S3) Only vertical diodes are ON, (S4) Only horizontal diodes are ON. Two configurations as shown in Figure 3 are planned to use to verify and study the effects of FSS.

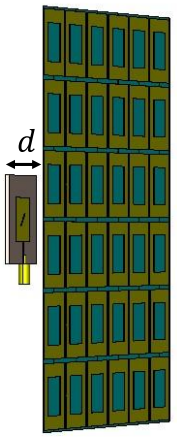

(a)

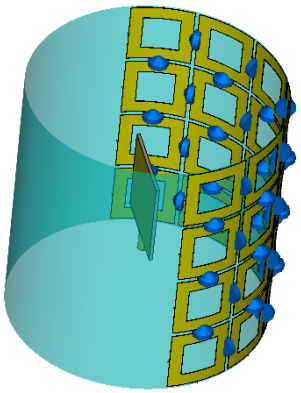

(b)

Figure 3. Antenna - FSS system configuration in simulation

Résumé en français

La 5G FWA (Fixed Wireless Access) est en cours de développement pour proposer des connexions large bande et haut débit. Selon une étude (rapport d'Ericsson de juin 2022 [1]) des forfaits de vente au détail proposés par les fournisseurs de services dans le monde entier, au premier semestre 2022, le nombre de fournisseurs de services 5G FWA dans le monde a augmenté d'environ 30 %, passant de 57 à 75 fournisseurs de services. L'estimation du développement de la 5G FWA, basée sur l'étude d'Ericsson, montre également que la 5G FWA continuera son essor fulgurant. Elle devrait atteindre environ 110 millions de connexions d'ici 2027, soit près de la moitié du nombre total de connexions FWA. La 5G FWA apporte de nombreux avantages tels que le haut débit, la faible latence et la flexibilité. En France, les principales bandes utilisées pour la recherche ou le déploiement de la 5G sont les fréquences déjà précédemment utilisées pour la 2G, 3G, 4G, ainsi que la bande 3.4 - 3.8 GHz et la bande autour de 26 GHz. Les quatre grands opérateurs en France (Bouygues Telecom, Free Mobile, Orange et SFR) se sont inscrits pour utiliser les bandes de fréquences dans la bande 3.4 – 3.8 GHz en 2020 et les déployer civilement. La bande 26 GHz, bien qu'inexplorée dans les télécommunications civiles, est une bande très prometteuse pour résoudre le problème de l'explosion de la consommation de données.

Bien qu'il existe de nombreux avantages, la 5G FWA est confrontée au défi principal des pertes rencontrées à ce type de fréquences élevées. Celles-ci proviennent de diverses sources telles que les pertes durant le trajet de l'onde, la ligne de mire FWA non idéale, les pertes par pénétration de l'onde à travers les bâtiments et les pertes par interaction avec la végétation. De nombreuses études ont été menées pour mesurer et construire des modèles pour pouvoir estimer les pertes. Ces travaux sont importants car la prédiction des pertes affecte grandement la décision, la planification et le déploiement du système 5G FWA. Certains modèles célèbres peuvent être mentionnés comme Okumura, Hata, Alpha-Beta-Gamma (AGB), Close-In (CI), Floating Intercept (FI), 2-ray, Winner II, Log Distance (LD). Outre cela, les études liées à la mesure et à l'analyse des facteurs contribuant aux pertes présentent également un grand intérêt. Des mesures pour comprendre l'influence de la structure du bâtiment ainsi que les matériaux des bâtiments sont présentées dans [9], [25]. Pour la propagation des ondes de la FWA à l'extérieure, la végétation et les conditions météorologiques sont également deux des facteurs importants contribuant aux pertes [26]–[29]. De ces études, on peut voir que les végétaux (les feuilles, les branches, les tiges…) qui sont répartis de manière aléatoire dans le milieu de

propagation peuvent provoquer de la diffusion, de l'atténuation, de l'absorption et de la diffraction des ondes rayonnées. Après avoir mesuré, testé, calculé les facteurs de pertes, des méthodes pour les minimiser sont étudiées et proposées au travers de nombreuses études. En général, ces solutions d'amélioration peuvent être divisées en 3 catégories : l'utilisation d'antennes à gain élevé, l'utilisation d'antennes orientables et l'amélioration des matériaux de construction.

La formule de Friis en décibels peut s'écrire (1.1):

$$P_r = P_t + G_t + G_r - PL \tag{1.1}$$

Où : P_r est la puissance des ondes reçues, P_t est la puissance des ondes transmises, G_t est le gain de l'antenne d'émission, G_r est le gain de l'antenne de réception et PL (path loss) les pertes dues à l'atténuation des ondes électromagnétiques sur le trajet parcouru.

D'après la formule, on peut voir que, si les pertes liées au trajet augmentent, pour s'assurer que la puissance reçue n'est pas réduite, on peut augmenter le gain des antennes, ou en d'autres termes, on peut utiliser des antennes à gain élevé pour améliorer le problème de pertes lié à des trajets conséquents. Afin d'avoir une antenne à gain élevé, en plus d'utiliser des antennes traditionnelles à gain élevé (telles que l'antenne cornet, l'antenne Vivaldi), des méthodes pour améliorer le gain des antennes de base sont également développées. L'utilisation d'une lentille est une méthode efficace pour améliorer le gain d'antenne, qui est normalement basée sur le principe d'une lentille optique : les ondes ont une vitesse de phase différente de celle qu'elles auraient normalement dans l'air, de sorte que la lentille, ayant une épaisseur variable par endroits, retarde les faisceaux de l'onde qui passent à travers en introduisant des temps de propagation différents, modifiant ainsi la forme du front d'onde et la direction de propagation des ondes. Par conséquent, en construisant des lentilles avec des formes spécifiques, il est possible d'augmenter le gain de l'antenne [29], [33]–[35]. Par ailleurs, l'utilisation de FSS (Frequency Selective Surface) ou de métamatériaux pour créer des réflecteurs ou des plans de réseau avec des propriétés spéciales contribue à augmenter le gain d'une antenne [36], [37], [37], [39], comme le montrent les deux exemples de la Figure 1.

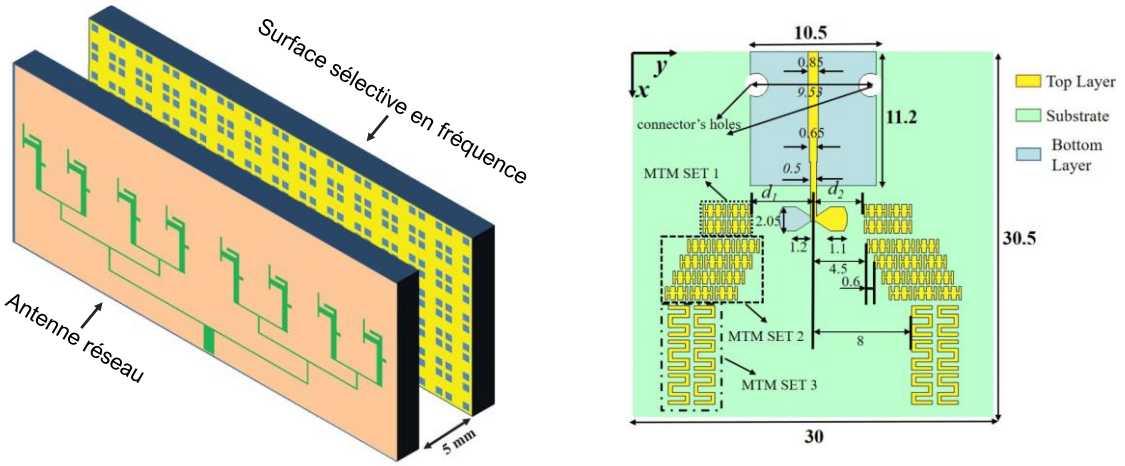

(a) (b)

Figure 1. (a) Antenne réseau avec surface sélective en fréquence [36] (b) Antenne nœud papillon avec métamatériau [39]

Dans la technologie 5G FWA, les deux grandes familles de périphériques rencontrés sont : l'unité d'accès (Access Unit - AU) et l'équipement dans les locaux du client (Customer Premise Equipment - CPE). Habituellement, un AU se connecte à plusieurs CPE. Cela peut entraîner une dissipation d'énergie et également une transmission de signal inefficace. Pour résoudre ce problème, une solution largement utilisée aujourd'hui consiste à utiliser une technique modelage de la forme des faisceaux (beamforming) émis par l'antenne. La mise en forme des faisceaux est une procédure qui oriente la majorité des signaux générés à partir d'un réseau d'antennes d'émission vers une direction angulaire prévue [50]. La formation de faisceaux est généralement utilisée avec les systèmes de réseau d'antennes pour focaliser le signal sans fil dans une direction spécifique, comme illustré sur la Figure 2. Le BF a évolué d'une formation de faisceau unidimensionnelle (1D) à tridimensionnelle (3D). La mise en forme du faisceau peut se faire via 3 solutions technologiques : le BF analogique, le BF numérique et le BF hybride. Dans les applications simples, comme dans les CPE, l'utilisation de structures de formation de faisceaux simples est préférée. L'un des systèmes de formation de faisceaux les plus simples et les plus compacts est le système de formation de faisceaux à base de lentille de Rotman [54]. Un autre système compact de formation de faisceaux qui a été développé est le système d'antenne à cavité résonnante (RCA) [56], [57]. En outre, le contrôle mécanique peut également être utilisé pour effectuer la fonction de formation de faisceaux.

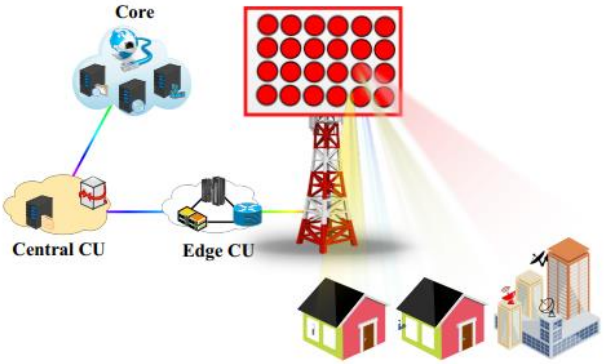

Figure 2. Réseau FWA utilisant un multiplexage MIMO (Multiple Input Multiple Output) et BF (beamforming) [3]

Comme mentionné, le signal sans fil est rapidement atténué lorsqu'il traverse des bâtiments. Les longueurs d'onde à des fréquences aussi élevées comme celles de la 5G sont très facilement bloquées ou à réfléchies par des matériaux de construction standard, ce qui rend difficile l'établissement et le maintien d'un lien entre une tour 5G FWA à proximité et un CPE dans les bâtiments. Un matériau en particulier a la propriété de bloquer les ondes : il s'agit du verre à faible émissivité (low-e). Un verre à faible émissivité de base se compose d'un panneau ou d'un diélectrique et d'un ou deux revêtements métalliques minces (d'épaisseur ayant pour ordre de grandeur la centaine de nanomètres), optiquement transparents et réfléchissant la chaleur mais également les ondes radio. Pour résoudre ce problème, de nombreuses méthodes sont proposées et la plupart d'entre elles suggèrent d'utiliser une métasurface. L'utilisation d'une métasurface peut se faire en remplaçant la couche métallique interne du verre par celle-ci. Il peut aussi être envisagé de fabriquer des couches de film à base de ces métasurfaces, que l'on vient coller directement sur le verre pour éviter d'avoir à refaire la porte en verre.

Dans cette thèse, nous travaillerons sur les deux premières solutions : l'utilisation d'antennes à haut gain et les techniques de formation de faisceaux. Ces méthodes sont étudiées en se basant sur des applications pour des dispositifs compacts, tels que des terminaux mobiles ou des CPE, plutôt que des applications à grande portée telles que des antennes de station.

Du fait de l'utilisation d'une antenne à gain élevé, nous explorons et proposons des méthodes pour augmenter son gain tout en gardant sa structure plate et compacte. Deux approches sont proposées et implémentées dans le chapitre 2. Ces antennes sont construites pour fonctionner dans la bande Ka (26 - 40 GHz). La largeur de cette bande Ka est capable de couvrir de plusieurs applications, notamment les télécommunications spatiales ou dans le cas nous intéressant, les fréquences les plus hautes de la 5G. Pour améliorer le gain de l'antenne tout en préservant sa

structure planaire, nous nous sommes attelés au développement de constructions à lentilles plates. La première structure est basée sur une lentille planaire dont les métallisations sont gravées à même le substrat, intégrant à son bout une structure quasi-SIW. Habituellement, l'architecture SIW est utilisée comme une ligne de transmission sans perte. Celle-ci est considérée comme un guide d'onde intégré dans le substrat, ou en d'autres termes, cette technique aide la structure à conserver ses propriétés planaires. Nous voulions donc tirer parti d'une architecture basée sur du SIW en bout de lentille pour augmenter le gain de l'antenne, et pouvoir potentiellement en tirer profit pour d'autres applications ou la technologie SIW pourrait être impliquée. La deuxième méthode est basée sur une approche de type PCL (Phase Compensation Lens). Cette architecture de lentille a déjà été utilisée dans plusieurs études. Cependant, à la connaissance de l'auteur, le processus de conception d'une lentille de type PCL ainsi que les inconvénients de cette approche ne sont généralement pas clairement présentés. Par conséquent, dans la dernière partie du second chapitre, nous proposons un processus de conception de cette lentille à l'aide de logiciels utilisés classiquement tels que CST Studio Suite ou MATLAB.

Ensuite, dans le chapitre 3, nous nous concentrons sur la mise en forme de faisceaux, basée sur les FSS imprimées sur une structure 3D. Pour contextualiser cette étude, nous rappelons que des pertes très conséquentes sont causées par l'influence des matériaux de construction. Si une piste peut consister à améliorer ces matériaux sur leur « transparence » aux ondes, l'utilisation de CPE placés à l'extérieur est également une bonne solution. En effet, les CPE placés à l'extérieur peuvent être utilisés pour relayer la communication entre l'intérieur et l'extérieur du bâtiment, en particulier dans les cas où du verre à faible émissivité ou une mauvaise fenêtre est présent. Cependant, cela signifie également que les CPE extérieurs sont affectés par des facteurs environnementaux tels que la pluie et le vent. Pour protéger les circuits électroniques à l'intérieur, les CPE sont équipés d'une coque normalement étanche appelée radôme. Il s'agit d'une enceinte structurelle résistante aux intempéries utilisées pour protéger les systèmes de communication sans fil et est presque transparente aux ondes électromagnétiques. La seule fonction du radôme est de protéger le système interne. Ceci est relativement peu coûteux car dans de nombreux cas, le radôme occupera souvent un certain espace tout en n'ayant que cette seule fonction. Ainsi, dans notre étude, nous proposons d'imprimer nos structures FSS sur la surface du radôme et de les combiner à l'aide de composants actifs. En conséquence de quoi, le radôme peut à la fois protéger le système interne et contrôler son rayonnement. Certaines études similaires ont été menées, mais sont généralement effectuées sur des surfaces 1D. Le faire sur

une structure 3D nous paraît plus pertinent car la forme des radômes est généralement hémisphérique. Pour réaliser l'impression des motifs sur la surface du radôme, on utilise une technique d'impression par jet direct, et ce même sur une structure 3D. Cette technique, nouvellement développée, présente de nombreux atouts par rapport aux techniques d'impression équivalentes. La seule limitation technique actuelle réside dans le fait que la tête d'impression à encre est encore trop grande. Afin de pouvoir réaliser ce qui était prévu à l'origine pour fonctionnaliser le radôme tout en protégeant l'ensemble du système, nous avons dû faire le choix d'imprimer les motifs sur la face extérieure du radôme. En effet, pour les imprimer à l'intérieur avec la tête actuelle, un radôme avec un rayon d'au moins 1 à 2 m serait nécessaire. A titre d'information, le radôme sur lequel le démonstrateur est imprimé présente un rayon de 10 cm. La fréquence d'émission de l'antenne placée à l'intérieur du radôme est de 3,6 GHz - l'une des fréquences 5G FWA déployées civilement et présentant donc à ce jour un réel intérêt applicatif.

Enfin, dans le chapitre 4, nous présentons des résultats de recherches sur l'utilisation de substrats biosourcés. De nos jours, la plupart des systèmes électroniques utilisent couramment des substrats tels que le FR4 ou ceux de la gamme Rogers. Ce sont des substrats possédant de bonnes propriétés, mais ils sont produits à partir de ressources fossiles, qui ne sont pas respectueuses de l'environnement en raison de leur faible recyclabilité, et leur processus de production est énergivore. Dans un contexte où la pollution de l'environnement et ses conséquences deviennent de plus en plus graves, les actions de protection de l'environnement doivent être renforcées. Par conséquent, l'application de substrats biosourcés pour envisager la possibilité de remplacer les substrats traditionnels nous paraît être très intéressante. Dans ce chapitre, nous utiliserons des substrats en papier pour la conception et la fabrication de nos antennes ou de nos lentilles pour des applications en 5G FWA.

References

[1] Ericsson, “Ericsson Mobility Report.” Jun. 2022.

[2] Samsung Electronics Co., Ltd, “5G for Fixed Wireless Access.” 2019.

[3] I. A. Alimi, R. K. Patel, N. J. Muga, A. N. Pinto, A. L. Teixeira, and P. P. Monteiro, “Towards Enhanced Mobile Broadband Communications: A Tutorial on Enabling Technologies, Design Considerations, and Prospects of 5G and beyond Fixed Wireless Access Networks,” *Applied Sciences*, vol. 11, no. 21, p. 10427, Nov. 2021, doi: 10.3390/app112110427.

[4] M. Cheffena and M. Mohamed, “Empirical Path Loss Models for Wireless Sensor Network Deployment in Snowy Environments,” *Antennas Wirel. Propag. Lett.*, pp. 1–1, 2017, doi: 10.1109/LAWP.2017.2751079.

[5] M. K. Samimi, T. S. Rappaport, and G. R. MacCartney, “Probabilistic Omnidirectional Path Loss Models for Millimeter-Wave Outdoor Communications,” *IEEE Wireless Commun. Lett.*, vol. 4, no. 4, pp. 357–360, Aug. 2015, doi: 10.1109/LWC.2015.2417559.

[6] A. I. Sulyman, A. Alwarafy, G. R. MacCartney, T. S. Rappaport, and A. Alsanie, “Directional Radio Propagation Path Loss Models for Millimeter-Wave Wireless Networks in the 28-, 60-, and 73-GHz Bands,” *IEEE Trans. Wireless Commun.*, vol. 15, no. 10, pp. 6939–6947, Oct. 2016, doi: 10.1109/TWC.2016.2594067.

[7] I. A. Alimi, R. K. Patel, N. J. Muga, and P. P. Monteiro, “Performance Analysis of 5G Fixed Wireless Access Networks with Antenna Diversity Techniques,” *Wireless Pers Commun*, vol. 113, no. 3, pp. 1541–1565, Aug. 2020, doi: 10.1007/s11277-020-07399-8.

[8] S. Dominic *et al.*, “All-Indoor Optical Customer Premises Equipment for Fixed Wireless Access,” presented at the 2021 Optical Fiber Communications Conference and Exhibition (OFC), 2021.

[9] J. Du, D. Chizhik, R. Feick, G. Castro, M. Rodriguez, and R. A. Valenzuela, “Suburban Residential Building Penetration Loss at 28 GHz for Fixed Wireless Access,” *IEEE Wireless Commun. Lett.*, vol. 7, no. 6, pp. 890–893, Dec. 2018, doi: 10.1109/LWC.2018.2835473.

[10] G. Bolun *et al.*, “Building entry loss model for 24 to 31GHz band,” presented at the 2016 International Symposium on Antennas and Propagation (ISAP), Oct. 2016.

[11] J. Lehtomaki, R. Vuohtoniemi, M. Matinmikko-Blue, and K. Hiltunen, “Building-to-building propagation loss measurements at 3.5 GHz with application to micro operators,” in *2018 IEEE Wireless Communications and Networking Conference (WCNC)*, Barcelona, Apr. 2018, pp. 1–6. doi: 10.1109/WCNC.2018.8377102.

[12] M. U. Sheikh, L. Mela, N. Saba, K. Ruttik, and R. Jantti, “Outdoor to Indoor Path Loss Measurement at 1.8GHz, 3.5GHz, 6.5GHz, and 26GHz Commercial Frequency Bands,” in *2021 24th International Symposium on Wireless Personal Multimedia Communications (WPMC)*, Okayama, Japan, Dec. 2021, pp. 1–5. doi: 10.1109/WPMC52694.2021.9700427.

[13] S. Y. Jun *et al.*, “Penetration Loss at 60 GHz for Indoor-to-Indoor and Outdoor-to-Indoor Mobile Scenarios,” in *2020 14th European Conference on Antennas and Propagation (EuCAP)*, Copenhagen, Denmark, Mar. 2020, pp. 1–5. doi: 10.23919/EuCAP48036.2020.9135581.

[14] S. Sun, G. R. MacCartney, and T. S. Rappaport, “Millimeter-wave distance-dependent large-scale propagation measurements and path loss models for outdoor and indoor 5G systems,” in *2016 10th European Conference on Antennas and Propagation (EuCAP)*, Davos, Switzerland, Apr. 2016, pp. 1–5. doi: 10.1109/EuCAP.2016.7481506.

[15] H. Zhang *et al.*, “mmWave Indoor Channel Measurement Campaign for 5G New Radio Indoor Broadcasting,” *IEEE Trans. on Broadcast.*, vol. 68, no. 2, pp. 331–344, Jun. 2022, doi: 10.1109/TBC.2021.3131864.

[16] M. K. Elmezughi and T. J. Afullo, “An Efficient Approach of Improving Path Loss Models for Future Mobile Networks in Enclosed Indoor Environments,” *IEEE Access*, vol. 9, pp. 110332–110345, 2021, doi: 10.1109/ACCESS.2021.3102991.

[17] N. O. Oyie and T. J. O. Afullo, “Measurements and Analysis of Large-Scale Path Loss Model at 14 and 22 GHz in Indoor Corridor,” *IEEE Access*, vol. 6, pp. 17205–17214, 2018, doi: 10.1109/ACCESS.2018.2802038.

[18] S. Dahal, S. Ahmed, H. King, G. Bharatula, J. Campbell, and M. Faulkner, “Urban Microcell 39 GHz Measurements,” *Antennas Wirel. Propag. Lett.*, vol. 18, no. 10, pp. 2071–2075, Oct. 2019, doi: 10.1109/LAWP.2019.2937539.

[19] N. Moraitis, D. Vouyioukas, A. Gkioni, and S. Louvros, “Rural Path Loss Measurements and Models for a Fixed Wireless Access TD-LTE Network at 3.7 GHz,” *2019 13th European Conference on Antennas and Propagation (EuCAP)*, pp. 1–5, 2019.

[20] G. R. MacCartney and T. S. Rappaport, “Rural Macrocell Path Loss Models for Millimeter Wave Wireless Communications,” *IEEE J. Select. Areas Commun.*, vol. 35, no. 7, pp. 1663–1677, Jul. 2017, doi: 10.1109/JSAC.2017.2699359.

[21] S. Sun *et al.*, “Investigation of Prediction Accuracy, Sensitivity, and Parameter Stability of Large-Scale Propagation Path Loss Models for 5G Wireless Communications,” *IEEE Trans. Veh. Technol.*, vol. 65, no. 5, pp. 2843–2860, May 2016, doi: 10.1109/TVT.2016.2543139.

[22] J. Thrane, D. Zibar, and H. L. Christiansen, “Model-Aided Deep Learning Method for Path Loss Prediction in Mobile Communication Systems at 2.6 GHz,” *IEEE Access*, vol. 8, pp. 7925–7936, 2020, doi: 10.1109/ACCESS.2020.2964103.

[23] H. Cheng, S. Ma, H. Lee, and M. Cho, “Millimeter Wave Path Loss Modeling for 5G Communications Using Deep Learning With Dilated Convolution and Attention,” *IEEE Access*, vol. 9, pp. 62867–62879, 2021, doi: 10.1109/ACCESS.2021.3070711.

[24] A. Gupta, J. Du, D. Chizhik, R. A. Valenzuela, and M. Sellathurai, “Machine Learning-Based Urban Canyon Path Loss Prediction Using 28 GHz Manhattan Measurements,” *IEEE Trans. Antennas Propagat.*, vol. 70, no. 6, pp. 4096–4111, Jun. 2022, doi: 10.1109/TAP.2022.3152776.

[25] M. H. Tariq, I. Chondroulis, P. Skartsilas, N. Babu, and C. B. Papadias, “mmWave Massive MIMO Channel Measurements for Fixed Wireless and Smart City Applications,” in *2020 IEEE 31st Annual International Symposium on Personal, Indoor and Mobile Radio Communications*, London, United Kingdom, Aug. 2020, pp. 1–6. doi: 10.1109/PIMRC48278.2020.9217375.

[26] Z. El Khaled, W. Ajib, and H. Mcheick, “Log Distance Path Loss Model: Application and Improvement for Sub 5 GHz Rural Fixed Wireless Networks,” *IEEE Access*, vol. 10, pp. 52020–52029, 2022, doi: 10.1109/ACCESS.2022.3166895.

[27] Z. A. Shamsan, “Rainfall and Diffraction Modeling for Millimeter-Wave Wireless Fixed Systems,” *IEEE Access*, vol. 8, pp. 212961–212978, 2020, doi: 10.1109/ACCESS.2020.3040624.

[28] S. Greg, “Using Modeling and Simulation to Assess Challenges and Solutions for 5G Fixed Wireless Access.” 2018.

[29] Y. S. Meng and Y. H. Lee, “Investigations of foliage effect on modern wireless communication systems: A review,” *PIER*, vol. 105, pp. 313–332, 2010, doi: 10.2528/PIER10042605.

[30] G. Julius and J. V. Wolfhard, *Handbook of Propagation Effects for Vehicular and Personal Mobile Satellite Systems*. 1998.

[31] N. Saba, L. Mela, M. U. Sheikh, J. Salo, K. Ruttik, and R. Jantti, “Rural Macrocell Path Loss Measurements for 5G Fixed Wireless Access at 26 GHz,” in *2021 IEEE 4th 5G World Forum (5GWF)*, Montreal, QC, Canada, Oct. 2021, pp. 328–333. doi: 10.1109/5GWF52925.2021.00064.

[32] R. Garg, R. K. Jaiswal, and N. P. Pathak, “Design and Development of High Gain and Narrow Beam Width Antenna For 5G Application,” in *2018 IEEE Indian Conference on Antennas and Propogation (InCAP)*, Hyderabad, India, Dec. 2018, pp. 1–5. doi: 10.1109/INCAP.2018.8770956.

[33] G. R. Shalini, D. R. Krishna, G. Karthikeya, and S. K. Koul, “Design of 3D printed lens antenna for 5G applications,” in *2021 IEEE MTT-S International Microwave and RF Conference (IMARC)*, KANPUR, India, Dec. 2021, pp. 1–4. doi: 10.1109/IMaRC49196.2021.9714615.

[34] E. H. Mujammami and A. Sebak, “A High Gain Broadband Quasi-Yagi Dielectric Lens Antenna for 5G and Millimeter Wave Applications,” in *2019 IEEE International Symposium on Antennas and Propagation and USNC-URSI Radio Science Meeting*, Atlanta, GA, USA, Jul. 2019, pp. 1911–1912. doi: 10.1109/APUSNCURSINRSM.2019.8888866.

[35] T. A. H. Bressner, M. N. Johansson, A. B. Smolders, and U. Johannsen, “High-Gain Lens-Horn Antennas for Energy-Efficient 5G Millimeter-Wave Communication Infrastructure,” *IEEE Trans. Antennas Propagat.*, vol. 70, no. 5, pp. 3183–3194, May 2022, doi: 10.1109/TAP.2021.3137252.

[36] R. Ullah *et al.*, “Wideband and High Gain Array Antenna for 5G Smart Phone Applications Using Frequency Selective Surface,” *IEEE Access*, vol. 10, pp. 86117–86126, 2022, doi: 10.1109/ACCESS.2022.3196687.

[37] H. A. Mohamed, M. Edries, M. A. Abdelghany, and A. A. Ibrahim, “Millimeter-Wave Antenna With Gain Improvement Utilizing Reflection FSS for 5G Networks,” *IEEE Access*, vol. 10, pp. 73601–73609, 2022, doi: 10.1109/ACCESS.2022.3189651.

[38] Y. Chen *et al.*, “Landstorfer Printed Log-Periodic Dipole Array Antenna With Enhanced Stable High Gain for 5G Communication,” *IEEE Trans. Antennas Propagat.*, vol. 69, no. 12, pp. 8407–8414, Dec. 2021, doi: 10.1109/TAP.2021.3090079.

[39] H. Jiang, L.-M. Si, W. Hu, and X. Lv, “A Symmetrical Dual-Beam Bowtie Antenna With Gain Enhancement Using Metamaterial for 5G MIMO Applications,” *IEEE Photonics J.*, vol. 11, no. 1, pp. 1–9, Feb. 2019, doi: 10.1109/JPHOT.2019.2891003.

[40] J. Puskely, J. Lacik, Z. Raida, and H. Arthaber, “High-Gain Dielectric-Loaded Vivaldi Antenna for Ka Band Applications,” *Antennas Wirel. Propag. Lett.*, vol. 15, pp. 2004–2007, 2016, doi: 10.1109/LAWP.2016.2550658.

[41] Ying Song Zhang and Wei Hong, “A Millimeter-Wave Gain Enhanced Multi-Beam Antenna Based on a Coplanar Cylindrical Dielectric Lens,” *IEEE Trans. Antennas Propagat.*, vol. 60, no. 7, pp. 3485–3488, Jul. 2012, doi: 10.1109/TAP.2012.2194646.

[42] M. Moosazadeh and S. Kharkovsky, “A Compact High-Gain and Front-to-Back Ratio Elliptically Tapered Antipodal Vivaldi Antenna With Trapezoid-Shaped Dielectric Lens,” *Antennas Wirel. Propag. Lett.*, vol. 15, pp. 552–555, 2016, doi: 10.1109/LAWP.2015.2457919.

[43] B. Feng, Y. Tu, J. Chen, S. Yin, and K. L. Chung, “Dual Linearly-Polarized Antenna Array With High Gain and High Isolation for 5G Millimeter-Wave Applications,” *IEEE Access*, vol. 8, pp. 82471–82480, 2020, doi: 10.1109/ACCESS.2020.2990494.

[44] S. F. Jilani and A. Alomainy, “A Multiband Millimeter-Wave 2-D Array Based on Enhanced Franklin Antenna for 5G Wireless Systems,” *Antennas Wirel. Propag. Lett.*, vol. 16, pp. 2983–2986, 2017, doi: 10.1109/LAWP.2017.2756560.

[45] H. Ullah and F. A. Tahir, “A High Gain and Wideband Narrow-Beam Antenna for 5G Millimeter-Wave Applications,” *IEEE Access*, vol. 8, pp. 29430–29434, 2020, doi: 10.1109/ACCESS.2020.2970753.

[46] C.-X. Mao, M. Khalily, P. Xiao, T. W. C. Brown, and S. Gao, “Planar Sub-Millimeter-Wave Array Antenna With Enhanced Gain and Reduced Sidelobes for 5G Broadcast Applications,” *IEEE Trans. Antennas Propagat.*, vol. 67, no. 1, pp. 160–168, Jan. 2019, doi: 10.1109/TAP.2018.2874796.

[47] B. Feng, X. He, J.-C. Cheng, Q. Zeng, and C.-Y.-D. Sim, “A Low-Profile Differentially Fed Dual-Polarized Antenna With High Gain and Isolation for 5G Microcell Communications,” *IEEE Trans. Antennas Propagat.*, vol. 68, no. 1, pp. 90–99, Jan. 2020, doi: 10.1109/TAP.2019.2935091.

[48] W. Zhao, X. Li, Z. Qi, and H. Zhu, “Broadband and High-Gain Dual-Polarized Antenna Array With Shared Vias Feeding Network for 5G Applications,” *Antennas Wirel. Propag. Lett.*, vol. 20, no. 12, pp. 2377–2381, Dec. 2021, doi: 10.1109/LAWP.2021.3112565.

[49] N. O. Parchin, J. Zhang, R. A. Abd-Alhameed, G. F. Pedersen, and S. Zhang, “A Planar Dual-Polarized Phased Array With Broad Bandwidth and Quasi-Endfire Radiation for 5G Mobile Handsets,” *IEEE Trans. Antennas Propagat.*, vol. 69, no. 10, pp. 6410–6419, Oct. 2021, doi: 10.1109/TAP.2021.3069501.

[50] M. Faizi Khajeim, G. Moradi, R. Sarraf Shirazi, and S. Zhang, “Broadband Dual-Polarized Antenna Array With Endfire Radiation for 5G Mobile Phone Applications,” *Antennas Wirel. Propag. Lett.*, vol. 20, no. 12, pp. 2427–2431, Dec. 2021, doi: 10.1109/LAWP.2021.3113993.

[51] L. Wen, Y. Zhiqiang, L. Zhu, and J. Zhou, “High-Gain Dual-Band Resonant Cavity Antenna for 5G Millimeter-Wave Communications,” *Antennas Wirel. Propag. Lett.*, vol. 20, no. 10, pp. 1878–1882, Oct. 2021, doi: 10.1109/LAWP.2021.3098390.

[52] Y. Al-Alem and A. A. Kishk, “Low-Cost High-Gain Superstrate Antenna Array for 5G Applications,” *Antennas Wirel. Propag. Lett.*, vol. 19, no. 11, pp. 1920–1923, Nov. 2020, doi: 10.1109/LAWP.2020.2974455.

[53] I. Ahmed *et al.*, “A Survey on Hybrid Beamforming Techniques in 5G: Architecture and System Model Perspectives,” *IEEE Commun. Surv. Tutorials*, vol. 20, no. 4, pp. 3060–3097, 2018, doi: 10.1109/COMST.2018.2843719.

[54] J. Wang *et al.*, “3D Beamforming Technologies and Field Trials in 5G Massive MIMO Systems,” *IEEE Open J. Veh. Technol.*, vol. 1, pp. 362–371, 2020, doi: 10.1109/OJVT.2020.3030774.

[55] N. H. Mohamed, “Beamformers Explained.” CommScope, 2020.

[56] R. Chataut and R. Akl, “Massive MIMO Systems for 5G and beyond Networks—Overview, Recent Trends, Challenges, and Future Research Direction,” *Sensors*, vol. 20, no. 10, p. 2753, May 2020, doi: 10.3390/s20102753.

[57] E. H. Mujammami, I. Afifi, and A. B. Sebak, “Optimum Wideband High Gain Analog Beamforming Network for 5G Applications,” *IEEE Access*, vol. 7, pp. 52226–52237, 2019, doi: 10.1109/ACCESS.2019.2912119.

[58] S. Vashist, M. K. Soni, and P. K. Singhal, “A Review on the Development of Rotman Lens Antenna,” *Chinese Journal of Engineering*, vol. 2014, pp. 1–9, Jul. 2014, doi: 10.1155/2014/385385.

[59] A. Goudarzi, M. M. Honari, and R. Mirzavand, “A High-Gain Leaky-Wave Antenna Using Resonant Cavity Structure With Unidirectional Frequency Scanning Capability for 5G Applications,” *IEEE Access*, vol. 9, pp. 138858–138865, 2021, doi: 10.1109/ACCESS.2021.3118286.

[60] A. Goudarzi, M. M. Honari, and R. Mirzavand, “A Millimeter-Wave Fabry–Perot Cavity Antenna With Unidirectional Beam Scanning Capability for 5G Applications,” *IEEE Trans. Antennas Propagat.*, vol. 70, no. 3, pp. 1787–1796, Mar. 2022, doi: 10.1109/TAP.2021.3118796.

[61] Y.-F. Lin, W.-C. Chen, C.-H. Chen, C.-T. Liao, N.-C. Chuang, and H.-M. Chen, “High-Gain MIMO Dipole Antennas With Mechanical Steerable Main Beam for 5G Small Cell,” *Antennas Wirel. Propag. Lett.*, vol. 18, no. 7, pp. 1317–1321, Jul. 2019, doi: 10.1109/LAWP.2019.2914673.

[62] L. Liu *et al.*, “Achieving low-emissivity materials with high transmission for broadband radio-frequency signals,” *Sci Rep*, vol. 7, no. 1, p. 4840, Dec. 2017, doi: 10.1038/s41598-017-04988-9.

[63] O. Bouvard *et al.*, “Structured transparent low emissivity coatings with high microwave transmission,” *Appl. Phys. A*, vol. 123, no. 1, p. 66, Jan. 2017, doi: 10.1007/s00339-016-0701-8.

[64] P. J. Gibson, “The Vivaldi Aerial,” in *1979 9th European Microwave Conference*, Brighton, UK, Sep. 1979, pp. 101–105. doi: 10.1109/EUMA.1979.332681.

[65] A. Elsherbini *et al.*, “UWB antipodal vivaldi antennas with protruded dielectric rods for higher gain, symmetric patterns and minimal phase center variations,” in *2007 IEEE Antennas and Propagation Society International Symposium*, Honolulu, HI, Jun. 2007, pp. 1973–1976. doi: 10.1109/APS.2007.4395909.

[66] R. Kazemi, A. E. Fathy, and R. A. Sadeghzadeh, “Dielectric Rod Antenna Array With Substrate Integrated Waveguide Planar Feed Network for Wideband Applications,” *IEEE Trans. Antennas Propagat.*, vol. 60, no. 3, pp. 1312–1319, Mar. 2012, doi: 10.1109/TAP.2011.2182489.

[67] M. Amiri, F. Tofigh, A. Ghafoorzadeh Yazdi, and M. Abolhasan, “Exponential Antipodal Vivaldi Antenna With Exponential Dielectric Lens,” *Antennas Wirel. Propag. Lett.*, pp. 1–1, 2017, doi: 10.1109/LAWP.2017.2679125.

[68] M. Moosazadeh, S. Kharkovsky, J. T. Case, and B. Samali, “Improved Radiation Characteristics of Small Antipodal Vivaldi Antenna for Microwave and Millimeter-Wave Imaging Applications,” *Antennas Wirel. Propag. Lett.*, vol. 16, pp. 1961–1964, 2017, doi: 10.1109/LAWP.2017.2690441.

[69] O. Yesilyurt and G. Turhan-Sayan, “Metasurface Lens for Ultra-Wideband Planar Antenna,” *IEEE Trans. Antennas Propagat.*, vol. 68, no. 2, pp. 719–726, Feb. 2020, doi: 10.1109/TAP.2019.2940462.

[70] H. Cheng, H. Yang, Y. Li, and Y. Chen, “A Compact Vivaldi Antenna With Artificial Material Lens and Sidelobe Suppressor for GPR Applications,” *IEEE Access*, vol. 8, pp. 64056–64063, 2020, doi: 10.1109/ACCESS.2020.2984010.

[71] L. Sang, S. Wu, G. Liu, J. Wang, and W. Huang, “High-Gain UWB Vivaldi Antenna Loaded With Reconfigurable 3-D Phase Adjusting Unit Lens,” *Antennas Wirel. Propag. Lett.*, vol. 19, no. 2, pp. 322–326, Feb. 2020, doi: 10.1109/LAWP.2019.2961393.

[72] O. Turkmen-Kucuksari, A. Kocakaya, S. Çimen, and G. Çakır, “High constant gain modified antipodal Vivaldi antenna incorporated with a phase compensation lens and a frequency selective surface,” *AEU - International Journal of Electronics and Communications*, vol. 113, p. 152975, Jan. 2020, doi: 10.1016/j.aeue.2019.152975.

[73] K. Wu, D. Deslandes, and Y. Cassivi, “The substrate integrated circuits - a new concept for high-frequency electronics and optoelectronics,” in *6th International Conference on Telecommunications in Modern Satellite, Cable and Broadcasting Service, 2003. TELSIKS 2003.*, Nis, Yugoslavia, 2003, p. P-III. doi: 10.1109/TELSKS.2003.1246173.

[74] X.-P. Chen and K. Wu, “Substrate Integrated Waveguide Filter: Basic Design Rules and Fundamental Structure Features,” *IEEE Microwave*, vol. 15, no. 5, pp. 108–116, Jul. 2014, doi: 10.1109/MMM.2014.2321263.

[75] A. Patrovsky, M. Daigle, and K. Wu, “Millimeter-wave wideband transition from CPW to substrate integrated waveguide on electrically thick high-permittivity substrates,” in *2007 European Microwave Conference*, Munich, Germany, Oct. 2007, pp. 138–141. doi: 10.1109/EUMC.2007.4405145.

[76] D. M. Pozar, *Microwave engineering*, Fourth Edition. Hoboken, NJ: John Wiley & Sons, Inc, 2012.

[77] D. Deslandes, “Design equations for tapered microstrip-to-Substrate Integrated Waveguide transitions,” in *2010 IEEE MTT-S International Microwave Symposium*, Anaheim, CA, USA, May 2010, pp. 704–707. doi: 10.1109/MWSYM.2010.5517884.

[78] D. Deslandes and Ke Wu, “Accurate modeling, wave mechanisms, and design considerations of a substrate integrated waveguide,” *IEEE Trans. Microwave Theory Techn.*, vol. 54, no. 6, pp. 2516–2526, Jun. 2006, doi: 10.1109/TMTT.2006.875807.

[79] J. Zhang, X. Zhang, and S. Xiao, “Antipodal Vivaldi Antenna to Detect UHF Signals That Leaked Out of the Joint of a Transformer,” *International Journal of Antennas and Propagation*, vol. 2017, pp. 1–13, 2017, doi: 10.1155/2017/9627649.

[80] W. L. Stutzman and G. A. Thiele, *Antenna theory and design*, 3rd ed. Hoboken, NJ: Wiley, 2013.

[81] C. A. Balanis, *Antenna theory: analysis and design*, 3rd ed. Hoboken, NJ: John Wiley, 2005.

[82] X. Li, L. Sang, Y. Shi, G. Lv, and R. Cao, "Gain improvement of planar-printed broadband end-fire antenna," *International Journal of Electronics*, vol. 104, no. 11, pp. 1906–1919, Nov. 2017, doi: 10.1080/00207217.2017.1329949.

[83] H. Cheng, L. Hua, Y. Wang, H. Yang, and T. Lu, "Design of high gain Vivaldi antenna with a compound optical lens inspired by metamaterials," *Int J RF Microw Comput Aided Eng*, vol. 31, no. 4, Apr. 2021, doi: 10.1002/mmce.22570.

[84] R. Shavit, *Radome electromagnetic theory and design*. 2018. Accessed: Mar. 13, 2022. [Online]. Available: https://onlinelibrary.wiley.com/doi/book/10.1002/9781119410850

[85] P. Mei, X. Q. Lin, J. W. Yu, P. C. Zhang, and A. Boukarkar, "A Low Radar Cross Section and Low Profile Antenna Co-Designed With Absorbent Frequency Selective Radome," *IEEE Trans. Antennas Propagat.*, vol. 66, no. 1, pp. 409–413, Jan. 2018, doi: 10.1109/TAP.2017.2767645.

[86] W.-J. Liao, W.-Y. Zhang, Y.-C. Hou, S.-T. Chen, C. Y. Kuo, and M. Chou, "An FSS-Integrated Low-RCS Radome Design," *Antennas Wirel. Propag. Lett.*, vol. 18, no. 10, pp. 2076–2080, Oct. 2019, doi: 10.1109/LAWP.2019.2937556.

[87] H. Zhou *et al.*, "Filter-Antenna Consisting of Conical FSS Radome and Monopole Antenna," *IEEE Trans. Antennas Propagat.*, vol. 60, no. 6, pp. 3040–3045, Jun. 2012, doi: 10.1109/TAP.2012.2194648.

[88] I. M. Ehrenberg, S. E. Sarma, and B.-I. Wu, "Fully conformal FSS via rapid 3D prototyping," in *Proceedings of the 2012 IEEE International Symposium on Antennas and Propagation*, Chicago, IL, USA, Jul. 2012, pp. 1–2. doi: 10.1109/APS.2012.6348601.

[89] B. Gao, S. Huang, Z. Ren, Y. Chen, and X. Wang, "Design and Verification of an Integrated Free-Standing Thick-Screen FSS Radome," *Antennas Wirel. Propag. Lett.*, vol. 17, no. 9, pp. 1630–1634, Sep. 2018, doi: 10.1109/LAWP.2018.2859232.

[90] C. Delfaut, "Intégration de fonctions électroniques imprimées sur des thermoplastiques 2D et 3D pour des applications radiofréquences," 2022.

[91] G. Houzet *et al.*, "In-situ characterization up to 100 GHz of insulators used in new 3D 'System in Package on board' (SiPoB) technologies," *Microelectronics Journal*, vol. 108, p. 104990, Feb. 2021, doi: 10.1016/j.mejo.2021.104990.

[92] T.-K. Wu, "Frequency Selective Surfaces," in *Encyclopedia of RF and Microwave Engineering*, K. Chang, Ed. Hoboken, NJ, USA: John Wiley & Sons, Inc., 2005, p. eme133. doi: 10.1002/0471654507.eme133.

[93] Suhair Mansoor Mahmood, "Antennes Reconfigurables en Diagramme de Rayonnement à base de Surfaces Sélectives de Fréquence," 2016.

[94] M. Al-Joumayly and N. Behdad, "A New Technique for Design of Low-Profile, Second-Order, Bandpass Frequency Selective Surfaces," *IEEE Trans. Antennas Propagat.*, vol. 57, no. 2, pp. 452–459, Feb. 2009, doi: 10.1109/TAP.2008.2011382.

[95] A. Kraszewski, "Prediction of the Dielectric Properties of Two-Phase Mixtures," *Journal of Microwave Power*, vol. 12, no. 3, pp. 216–222, Jan. 1977, doi: 10.1080/16070658.1977.11689049.

[96] M. N. Nassajfar, I. Deviatkin, V. Leminen, and M. Horttanainen, “Alternative Materials for Printed Circuit Board Production: An Environmental Perspective,” *Sustainability*, vol. 13, no. 21, p. 12126, Nov. 2021, doi: 10.3390/su132112126.

[97] B. S. Cook and A. Shamim, “Inkjet Printing of Novel Wideband and High Gain Antennas on Low-Cost Paper Substrate,” *IEEE Trans. Antennas Propagat.*, vol. 60, no. 9, pp. 4148–4156, Sep. 2012, doi: 10.1109/TAP.2012.2207079.

[98] M. F. Farooqui, C. Claudel, and A. Shamim, “An Inkjet-Printed Buoyant 3-D Lagrangian Sensor for Real-Time Flood Monitoring,” *IEEE Trans. Antennas Propagat.*, vol. 62, no. 6, pp. 3354–3359, Jun. 2014, doi: 10.1109/TAP.2014.2309957.

[99] H. AbuTarboush, M. Farooqui, and A. Shamim, “Inkjet-Printed Wideband Antenna on Resin-Coated Paper Substrate for Curved Wireless Devices,” *Antennas Wirel. Propag. Lett.*, pp. 1–1, 2015, doi: 10.1109/LAWP.2015.2425797.

[100] R. Sivasamy, L. Murugasamy, M. Kanagasabai, E. F. Sundarsingh, and M. Gulam Nabi Alsath, “A Low-Profile Paper Substrate-Based Dual-Band FSS for GSM Shielding,” *IEEE Trans. Electromagn. Compat.*, vol. 58, no. 2, pp. 611–614, Apr. 2016, doi: 10.1109/TEMC.2015.2498398.

[101] H. F. Abutarboush and A. Shamim, “A Reconfigurable Inkjet-Printed Antenna on Paper Substrate for Wireless Applications,” *Antennas Wirel. Propag. Lett.*, vol. 17, no. 9, pp. 1648–1651, Sep. 2018, doi: 10.1109/LAWP.2018.2861386.

[102] R. Hussain, M. U. Khan, and M. S. Sharawi, “Frequency Reconfigurable MIMO Antenna using SRR for Multi-Band Operation,” *2019 13th European Conference on Antennas and Propagation (EuCAP)*, pp. 1–3, 2019.

[103] A. Shastri, P. Njogu, B. Sanz-Izquierdo, S. Gao, and Z. Chen, “Low-cost Inkjet Printed Paper Poster FSS for 5G Applications,” in *2021 15th European Conference on Antennas and Propagation (EuCAP)*, Dusseldorf, Germany, Mar. 2021, pp. 1–4. doi: 10.23919/EuCAP51087.2021.9411448.

[104] T. Li, H. Zhai, X. Wang, L. Li, and C. Liang, “Frequency-Reconfigurable Bow-Tie Antenna for Bluetooth, WiMAX, and WLAN Applications,” *Antennas Wirel. Propag. Lett.*, vol. 14, pp. 171–174, 2015, doi: 10.1109/LAWP.2014.2359199.

[105] M. Sun, Z. Zhang, F. Zhang, and A. Chen, “L/S Multiband Frequency-Reconfigurable Antenna for Satellite Applications,” *Antennas Wirel. Propag. Lett.*, vol. 18, no. 12, pp. 2617–2621, Dec. 2019, doi: 10.1109/LAWP.2019.2945624.

[106] C. GUERS, “Optimisation des matériaux cellulosiques pour des applications en radiofréquences et térahertz,” 2016.

[107] R. Parashkov, E. Becker, T. Riedl, H.-H. Johannes, and W. Kowalsky, “Large Area Electronics Using Printing Methods,” *Proc. IEEE*, vol. 93, no. 7, pp. 1321–1329, Jul. 2005, doi: 10.1109/JPROC.2005.850304.

[108] A. Niembro-Martin, E. Pistono, P. Lemaitre-Auger, T.-P. Vuong, and G. E. P. Tourtollet, “Efficient setup for the measurement of transmission-coefficients with a single-room anechoic chamber,” in *2014 IEEE Conference on Antenna Measurements & Applications (CAMA)*, Antibes Juan-les-Pins, France, Nov. 2014, pp. 1–3. doi: 10.1109/CAMA.2014.7003432.

LIST OF PUBLICATIONS

International journal

1. T. Dam, G. Houzet, T. Lacrevaz, and T. Vuong, "High gain Vivaldi antenna from 26 up to 40 GHz for 5G applications," *Micro & Optical Tech Letters*, vol. 64, no. 7, pp. 1267–1271, Jul. 2022, doi: 10.1002/mop.33271.

International conference

1. D. T. Hong Le, M. T. Le, B. Cabon, and T. P. Vuong, "A Broadband High Gain SIW Dielectric Rod Antenna," in *2019 International Conference on Advanced Technologies for Communications (ATC)*, Hanoi, Vietnam, Oct. 2019, pp. 7–9. doi: 10.1109/ATC.2019.8924545.
2. T.-H.-L. Dam *et al.*, "Printed radome for reconfigurable antenna radiation pattern in 5G applications," in *2021 IEEE International Symposium on Antennas and Propagation and USNC-URSI Radio Science Meeting (APS/URSI)*, Singapore, Singapore, Dec. 2021, pp. 309–310. doi: 10.1109/APS/URSI47566.2021.9704084.
3. T. H. Le Dam, T. T. Truong, M. T. Le, A. Niembro-Martin, E. Dreina, and T. P. Vuong, "Vertical and Horizontal SIW Horn Antennas at 60 GHz," in *2021 51st European Microwave Conference (EuMC)*, London, United Kingdom, Apr. 2022, pp. 749–752. doi: 10.23919/EuMC50147.2022.9784343.
4. T.-H.-L. Dam, G. Houzet, T. Lacrevaz, G. Gaborit, and T.-P. Vuong, "Investigation of phase compensation lens to improve the gain of Vivaldi antenna in Ka-band," in *2022 IEEE Ninth International Conference on Communications and Electronics (ICCE)*, Nha Trang, Vietnam, Jul. 2022, pp. 265–268. doi: 10.1109/ICCE55644.2022.9852039.
5. T. H. le Dam *et al.*, "Study of a 3D FSS-Based Printed Radome Demonstrator for a Patch Antenna at 3.6 GHz," in *2022 52nd European Microwave Conference (EuMC)*, Milan, Italy, Sep. 2022, pp. 664–667. doi: 10.23919/EuMC54642.2022.9924470.
6. T. H. le Dam *et al.*, "Reconfigurable Screen-Printed Patch Antenna on Paper for 4G and 5G Applications," in *2022 52nd European Microwave Conference (EuMC)*, Milan, Italy, Sep. 2022, pp. 64–67. doi: 10.23919/EuMC54642.2022.9924459.

National conference

1. Thi-Hong-Le Dam, Thi-Them Truong, Minh-Thuy Le, Alejandro Niembro-Martin, Emmanuel Dreina, Tan-Phu Vuong « Conception des antennes millimétriques en technologie SIW », Neuvième Conférence Plénière du GDR ONDES, 2021, Lille, France.

2. Thi-Hong-Le Dam, Camille Delfaut, Gregory Houzet, Thierry Lacrevaz, B. Fléchet, et al.. « Reconfiguration du diagramme de rayonnement d'une antenne dédiée à la 5G à l'aide d'un radôme imprimé en 3D », 22ème Journées Nationales Microondes (JNM 2022), Jun 2022, Limoges, France.